UC Berkeley
UC Berkeley Electronic Theses and Dissertations

Title
Design of Three-Dimensional Nanostructured Catalysts for the Oxygen Reduction Reaction

Permalink
https://escholarship.org/uc/item/342073s4

Author
Becknell, Nigel

Publication Date
2017

Peer reviewed|Thesis/dissertation

eScholarship.org Powered by the California Digital Library
University of California

Design of Three-Dimensional Nanostructured Catalysts for the Oxygen Reduction Reaction

By

Nigel Becknell

A dissertation submitted in partial satisfaction of the

requirements for the degree of

Doctor of Philosophy

in

Chemistry

in the

Graduate Division

of the

University of California, Berkeley

Committee in charge:

Professor Peidong Yang, Chair
Professor Gabor Somorjai
Professor Alexander Katz

Spring 2017

Design of Three-Dimensional Nanostructured Catalysts for the Oxygen Reduction Reaction

© 2017

By

Nigel Becknell

Abstract

Design of Three-Dimensional Nanostructured Catalysts for the Oxygen Reduction Reaction

by

Nigel Becknell

Doctor of Philosophy in Chemistry

University of California, Berkeley

Professor Peidong Yang, Chair

Anthropogenic CO_2 emissions from human dependence on fossil fuel are causing rising concentrations of CO_2 in the atmosphere and oceans, increasing the average temperature of the planet and acidifying the oceans, among other negative effects. Reliance on carbon-based fuels is not sustainable and must be replaced by alternative, renewable energy sources, including solar, wind, hydroelectric, and geothermal. The water cycle, splitting water into hydrogen and oxygen and electrochemically oxidizing the hydrogen to regenerate water, can be an efficient and sustainable energy storage cycle. An electrolyser powered by renewable electricity splits water, and a proton exchange membrane fuel cell uses hydrogen fuel to produce electricity on demand. The performance of proton exchange membrane fuel cells is significantly limited by the platinum-based oxygen reduction catalyst, which must be improved in activity and durability in order to commercialize applications such as fuel cell vehicles.

Bimetallic nanoframes have great potential for achieving new levels of catalytic activity in various heterogeneous reactions due to their high surface area dispersion of expensive noble metals on the exterior and interior surfaces of the structure. Pt-based nanoframes such as Pt-Ni and Pt-Co can be specifically tuned for excellent oxygen reduction activity and application in the cathode of proton exchange membrane fuel cells. Nanoframes were made by first synthesizing polyhedral nanoparticles with composition such as $PtCo_3$ or $PtNi_3$ by a hot-injection method. Scanning transmission electron microscopy combined with energy dispersive x-ray spectroscopy showed that these nanoparticles demonstrate elemental segregation of platinum to the edges of the polyhedron, forming the basis for a framework nanostructure. The process of preferential oxidative leaching was used to remove the non-noble metal from the interior of the framework, leaving the platinum-rich edges intact to form Pt_3Co or Pt_3Ni nanoframes.

Understanding the atomic structure of the nanoframe is crucial to exposing the source of its performance characteristics. It is highly unlikely that a catalyst remains the same under reaction conditions when compared to as-synthesized. Hence, the ideal experiment to study the catalyst structure should be performed *in situ*. X-ray absorption spectroscopy is an ideal *in situ* technique to study Pt_3Ni nanoframes, which are an excellent electrocatalyst for the oxygen reduction reaction. First, the surface characteristics of the nanoframes were probed through electrochemical hydrogen underpotential deposition and carbon monoxide electrooxidation, which proved that nanoframe surfaces with different structure exhibit varying levels of binding strength to adsorbate molecules. It is well-known that Pt-skin formation on Pt–Ni catalysts will enhance oxygen reduction activity by

weakening the binding energy between the surface and adsorbates. *Ex situ* and *in situ* X-ray absorption spectroscopy revealed that nanoframes which bind adsorbates more strongly have a rougher Pt surface caused by insufficient segregation of Pt to the surface and consequent Ni dissolution. In contrast, nanoframes which exhibit extremely high oxygen reduction activity demonstrated more significant segregation of Pt over Ni-rich subsurface layers, allowing better formation of the critical Pt-skin.

The nanoframe structure is made possible by the compositional heterogeneity in polyhedral Pt-Ni or Pt-Co nanocrystals, which offers additional variables to maneuver the functionality of the nanocrystal. However, understanding how to manipulate anisotropic elemental distributions in a nanocrystal is a great challenge in reaching higher tiers of nanocatalyst design. The evolutionary trajectory of phase segregation in Pt–Ni rhombic dodecahedra was studied in order to elucidate the mechanisms that enable synthesis of the Pt_3Ni nanoframe. The anisotropic growth of a Pt-rich phase along the <111> and <200> directions at the initial growth stage resulted in Pt segregation to the 14 axes of a rhombic dodecahedron, forming a highly branched, Pt-rich tetradecapod structure embedded in a Ni-rich shell. With longer growth time, the Pt-rich phase selectively migrated outwards through the 14 axes to the 24 edges such that the rhombic dodecahedron became a Pt-rich frame enclosing a Ni-rich interior phase. The Ni-rich interior was then selectively oxidized and corroded to form the hollow Pt_3Ni nanoframe that demonstrated exceptional catalytic activity for the oxygen reduction reaction.

The anisotropic phase segregation and migration mechanism offers a radically different approach to synthesis of nanocatalysts with desired compositional distributions and performance. The newly acquired understanding of these mechanisms was applied to manipulate the morphology of Pt-Ni rhombic dodecahedral nanoframes into excavated nanoframes that also exhibit high catalytic activity for the oxygen reduction reaction without need for Pt-skin formation. Controlling the ratio of platinum and nickel precursors within the nanoframe synthetic system adjusted the three-dimensional platinum anisotropy in the rhombic dodecahedron, resulting in a transition from the previous hollow nanoframe to a unique excavated structure. Excavated nanoframes showed ~10 times higher specific and ~6 times higher mass activity than commercial Pt/C, and twice the mass activity of the hollow nanoframe. The high specific activity of the excavated nanoframe is attributed to enhanced Ni content in the near-surface region and the extended two-dimensional sheet structure within the nanoframe that minimizes the number of low-coordinated Pt sites.

I dedicate this dissertation to my wife, Stef, my parents, Karen and Alan, and my brother, Francis, for their love and support throughout this entire process.

Table of Contents

List of Figures and Tables..... **iv**

List of Abbreviations..... **vi**

Acknowledgements..... **vii**

1. Introduction..... **1**

1.1 Brief Introduction to PEMFCs and ORR Challenges.....1
1.2 Rotating Disk Electrode Studies of Model Systems.....3
1.3 Bimetallic Alloys for ORR Catalysis.....4
1.4 Design of Nanostructured Catalysts for ORR.....9

2. Pt_3Co Nanoframes..... **15**

2.1 Preface.....15
2.2 Introduction.....15
2.3 $PtCo_3$ Nanoparticle Synthesis.....16
2.4 Evolution from $PtCo_3$ Nanoparticle to Pt_3Co Nanoframe.....17
2.5 Structure of $PtCo_3$ Nanoparticle and Pt_3Co Nanoframe.....18
2.6 Composition of $PtCo_3$ Nanoparticle and Pt_3Co Nanoframe.....19
2.7 Surface Characterization of $PtCo_3$ Nanoparticle.....20
2.8 Conclusions.....20

3. Atomic Structure of Nanoframes..... **21**

3.1 Preface.....21
3.2 Introduction.....21
3.3 Pt-Skin Formation on Pt_3Ni/C Catalyst.....22
3.4 *Ex Situ* XANES and EXAFS Analysis of As-Prepared Pt_3Ni/C.....24
3.5 *In Situ* XANES and EXAFS Analysis of Pt_3Ni/C.....27
3.6 Model of *Ex Situ* and *In Situ* Pt_3Ni/C Surfaces.....32
3.7 Conclusions.....33

4. Mechanism of Pt-Ni Rhombic Dodecahedron Growth..... **34**

4.1 Preface.....34
4.2 Introduction.....34
4.3 Pre-Rhombic Dodecahedron Observations.....35
4.4 Rhombic Dodecahedron Progression and Corrosion to 3-D Nanostructures.....36
4.5 Phase Segregation in Rhombic Dodecahedra.....41
4.6 Mechanism of Pt Segregation in Rhombic Dodecahedra.....43
4.7 Conclusions.....47

5. Excavated Nanoframes.....**49**

5.1 Preface.....49
5.2 Introduction.....49
5.3 Control of Pt Anisotropy in Rhombic Dodecahedra.....50
5.4 Phase Segregation in Rhombic Dodecahedra.....53
5.5 Morphology of Excavated Nanoframe.....57
5.6 Oxygen Reduction Activity of Excavated Nanoframes.....59
5.7 Conclusions.....61

6. Concluding Remarks.....**62**

References.....**64**

A1. Methods of Chapter 2.....**82**

A1.1 $PtCo_3$ Nanoparticle Synthesis.....82
A1.2 Evolution to Pt_3Co Nanoframes.....82
A1.3 Characterization of Pt-Co Nanoparticles and Nanoframes.....82

A2. Methods of Chapter 3.....**84**

A2.1 Synthesis of $PtNi_3$ Nanopolyhedra.....84
A2.2 Evolution from $PtNi_3$ Nanopolyhedra to Pt_3Ni Nanoframes.....84
A2.3 Preparation of Pt_3Ni/C Nanocatalyst and Testing.....84
A2.4 X-ray Diffraction.....85
A2.5 X-ray Absorption Measurements and Data Analysis.....85

A3. Methods of Chapter 4.....**87**

A3.1 Chemicals.....87
A3.2 Synthesis of Pt–Ni Rhombic Dodecahedra.....87
A3.3 Chemical Corrosion of Pt–Ni Rhombic Dodecahedra to $Pt_{75}Ni_{25}$ 3-D Structures.....87
A3.4 Characterization.....88
A3.5 Electrochemical Characterization.....88
A3.6 EXAFS Data Collection and Analysis.....88

A4. Methods of Chapter 5.....**90**

A4.1 Chemicals.....90
A4.2 Synthesis of Pt-Ni Rhombic Dodecahedra.....90
A4.3 Chemical corrosion to Nanoframes.....90
A4.4 Characterization.....90
A4.5 EXAFS Data Collection and Analysis.....91
A4.6 Electrochemical Characterization.....91

A5. Full Publication List.....**92**

List of Figures and Tables

Figure 1.1. Standard assembly of a PEMFC..... 2
Figure 1.2. Strategies for ORR catalyst design..... 3
Figure 1.3. Structure sensitivity of the ORR..... 4
Figure 1.4. Metal-adsorbate interaction..... 5
Figure 1.5. ORR Volcano plot..... 7
Figure 1.6. Pt-skin effect..... 8
Figure 1.7. Basic types of metal surface sites..... 9
Figure 1.8. Atomic layer deposition of Pt on Pd..... 10
Figure 1.9. Au enhancement of ORR stability..... 11
Figure 1.10. Dealloying trends in Pt-Ni octahedra..... 12
Figure 1.11. Nanoparticle Pt-skin formation..... 13
Figure 1.12. Pt_3Ni nanoframe discovery..... 14

Figure 2.1. TEM of Pt-Co NP and NF..... 16
Figure 2.2. Pt-Co NPs without oleic acid..... 17
Figure 2.3. XRD patterns of $PtCo_3$ NP and Pt_3Co NF..... 18
Figure 2.4. Elemental distribution of Pt-Co NP and NF..... 19
Figure 2.5. Evolution to Pt_3Co NF..... 19
Figure 2.6. Surface segregation in $PtCo_3$ NP..... 20

Figure 3.1. TEM images of as-prepared catalyst..... 23
Figure 3.2. Electrochemical characterization of NFs..... 23
Figure 3.3. X-ray absorption spectroscopy of Pt_3Ni/C catalysts before electrochemistry..... 24
Figure 3.4. XRD of NFs..... 25
Figure 3.5. EXAFS of as-prepared catalysts..... 26
Table 3.1. EXAFS fitting parameters of as-prepared nanoframe catalysts..... 27
Figure 3.6. XANES of Pt_3Ni/C catalysts *in situ* and after electrochemistry..... 28
Figure 3.7. EXAFS of catalysts *in situ*..... 29
Table 3.2. EXAFS fitting parameters of nanoframe catalysts during *in situ* ORR..... 30
Figure 3.8. EXAFS of catalysts after electrochemistry..... 31
Table 3.3. EXAFS fitting parameters of catalysts after electrochemistry..... 31
Figure 3.9. Nanoframe atomic structure models..... 32

Figure 4.1. Formation process of the rhombic dodecahedra..... 35
Figure 4.2. HRTEM images of interim ill-defined branches..... 36
Figure 4.3. Development of RD and corrosion to three-dimensional nanostructures..... 37
Figure 4.4. Size distributions of solid Pt-Ni RD and corroded products..... 37
Figure 4.5. TEM of RD-3-cor with different magnifications..... 38
Figure 4.6. Geometric model of rhombic dodecahedron..... 38
Figure 4.7. In-depth examination of tetradecapod geometry..... 39

Figure 4.8. STEM–EDS analysis of segregation and migration of Pt in Pt–Ni RD……...40
Table 4.1. Compositions of RD-3, RD-10 and RD-30 determined by EDS, ICP and XPS……...40
Figure 4.9. Structural evolution over time in Pt–Ni RD……... 41
Figure 4.10. EXAFS results for Pt-Ni rhombic dodecahedra……... 42
Table 4.2. EXAFS fitting parameters for RD-3, RD-10, and RD-30…… 43
Figure 4.11. Intermediate three-dimensional structures between tetradecapod and nanoframe…….44
Figure 4.12. *Ex situ* annealing converts RD-3 into "RD-10-like" dodecahedron……...45
Figure 4.13. Summary of the complete growth process of a Pt–Ni rhombic dodecahedron……. 46
Figure 4.14. Oxygen reduction activity of tetradecapods and nanoframes…… 47

Figure 5.1. Scheme of Pt anisotropy control strategy……....50
Figure 5.2. Rhombic dodecahedron growth schemes……... 51
Figure 5.3. Comparison of hollow and excavated nanoframes……..52
Figure 5.4. Morphology of solid dodecahedral nanoparticles……....52
Figure 5.5. Elemental mapping of hollow and excavated anisotropies……..53
Figure 5.6. X-ray diffraction of solid nanoparticles and nanoframes…… 54
Table 5.1. Compositions of hollow and excavated solid nanoparticles and nanoframes……....54
Figure 5.7. Elemental segregation in hollow and excavated solid nanoparticles…… 55
Figure 5.8. EXAFS of hollow and solid nanoframes…… 56
Table 5.2. EXAFS fitting results for hollow and excavated nanoframes……... 57
Figure 5.9. Three-dimensional morphology of the excavated nanoframe…… 58
Figure 5.10. TEM of as-loaded nanoframes on carbon support……... 59
Figure 5.11. Pt-skeleton formation on excavated and hollow nanoframes…… 60
Figure 5.12. Oxygen reduction activity of excavated nanoframes…… 60

Figure A2.1. *In situ* electrochemical XAS cell……....85

List of Abbreviations

ADT	Accelerated durability test
ALS	Advanced Light Source
APXPS	Ambient pressure X-ray photoelectron spectroscopy
CCD	Charge-coupled device
CO_{ad}	Adsorbed CO
Cu_{upd}	Copper underpotential deposition
CV	Cyclic voltammogram
DFT	Density functional theory
ECSA	Electrochemical surface area
EDS	Energy dispersive X-ray spectroscopy
ET	Electron tomography
EXAFS	Extended X-ray absorption fine structure
fcc	Face-centered cubic
FFT	Fast Fourier transform
FWHM	Full width at half maximum
GADDS	General area detector diffraction system
GDL	Gas diffusion layer
HAADF	High-angle annular dark-field
HOR	Hydrogen oxidation reaction
HRTEM	High-resolution transmission electron microscopy
H_{upd}	Hydrogen underpotential deposition
ICP-MS	Inductively coupled plasma mass spectrometry
ICP-OES	Inductively coupled plasma optical emission spectroscopy
MEA	Membrane electrode assembly
NF	Nanoframe
NP	Nanoparticle
ORR	Oxygen reduction reaction
PEMFC	Proton exchange membrane fuel cell
PGM	Platinum-group metal
RD	Rhombic dodecahedron(a)
RDE	Rotating disk electrode
RHE	Reversible hydrogen electrode
rpm	Revolutions per minute
SD	Solid dodecahedron
SEM	Scanning electron microscopy
SSA	Specific surface area
STEM	Scanning transmission electron microscopy
TEM	Transmission electron microscopy
UHV	Ultra-high vacuum
XANES	X-ray absorption near edge structure
XAS	X-ray absorption spectroscopy
XPS	X-ray photoelectron spectroscopy
XRD	X-ray diffraction
1, 2, or 3-D	One, two, or three-dimensional

Acknowledgements

First, I would like to thank Professor Peidong Yang, my advisor of the past five years. I knew when I accepted admittance to the UC Berkeley Chemistry Ph.D. program that I only wanted to work for Professor Yang, due to his research interests in nanomaterials applications to renewable energy technology and his drive to make a major impact in these fields. I feel extremely lucky to have been admitted to his group and am forever grateful for his scientific guidance that has built me into the scientist I am. I must also specifically thank him for a few advising decisions he made for me: (1) allowing me to switch my research into our group's nanoframe project after my first year; (2) suggesting that I attend the SUNCAT Catalysis Summer School at the beginning of my second year; (3) sliding the resume of my exceptional undergraduate mentee over to me at the beginning of my third year; and (4) recommending that I attend the Fuel Cells Gordon Conference at the beginning of my fifth year. I view these events as especially pivotal in my career as a UC Berkeley graduate student.

Next, I must thank all of the students and postdoctoral scholars that I have had the pleasure to work with over the years. I really appreciate the alternate perspectives and inspiration provided by new Yang group members including Mike Ross, Sheena Louisia, Stefano Cestellos-Blanco, Shouping Chen, and Zhenni Lin, and wish I could have overlapped in the group with them longer. It has also been a real pleasure working with Chris Kley for his sunny attitude every morning and German perspective. I am grateful to Jinghua Guo, Matthew Marcus, Sirine Fakra, Yifan Ye, Yi-Sheng Liu, Kaiqi Nie, and Ethan Crumlin for all the help with training and experiments at the Advanced Light Source, a critical resource to my Ph.D. career. The ALS was the location for long nights and fascinating experiments with the original Team X-rayted, Anthony Fu, Nick Kornienko, and Joaquin Resasco, and the new X-ray team Chenlu Xie, Qiao Kong, and Hao Zhang, all of whom made those long experiments enjoyable.

Older students that I am grateful to have overlapped with include Sean Andrews, who developed my passion for Your Mom (the chemistry softball team), Chong Liu, who taught me so much about experimental design, and Michael Moore, who I believe originally suggested to Peidong that I should join Andrew Wong as a lab safety officer. Andrew was awesome to work with because he cared so much about safety and could be relied on not to overlook something. I am now very appreciative to be working with Yifan Li and Teng Lei on continuing the Yang Group's excellent safety tradition, and am confident they will carry the torch. In addition to safety, teaching was a large and unexpectedly bright portion of my graduate career, and I am extremely thankful to Dr. Michelle Douskey for instilling in me a passion for chemistry education.

Of course, I must acknowledge the six other students, Fan Cui, Dandan Zhang, Yude Su, Kelsey Sakimoto, Joaquin Resasco, and Dohyung Kim who joined the Yang Group with me in 2012. I think we collectively brought a strong workforce to the Yang Group at a time when it needed youth. I especially must thank Dohyung for the collaboration and conversation as we kicked off the Yang Group's major efforts in catalysis, which grew to become one of the largest subgroups in the group. Finally, I must thank the ORR Team I worked with: Yoonkook Son, Zhiqiang Niu, and Cindy Zheng. Yoonkook brought a lot of hard work and new perspectives to nanoframe research. Zhiqiang taught me so much about the research process and I am extremely grateful to have worked so closely with him. Cindy was my undergraduate mentee for three years and I could not have asked for anyone better. Her exuberant personality and at times goofy discussions brought happiness to my days even when things were not going so well. She worked so hard on our projects that I sometimes had to force her

to take a break or ration the number of experiments she did, because I knew she would be willing to do them all. Mentoring Cindy was undoubtedly the best decision I made in my graduate career, and I wish her all the best in her own graduate career and hope she always remembers her original motivations for wanting to do chemistry research.

Outside of the lab, my friends and family have been my foundation allowing me to keep my perspective throughout the hardest task I have ever undertaken. My friends Ryan Solomon, Mahesh Shirole, and Megan Cleveland from back home have rigorously stayed in touch even though I have not been back as often as I would have liked. They are my constant reminder of where I came from, how I grew up, and who I am. Neelay Phadke braved the transition from UW-Madison to UC Berkeley with me and has been my best beer-brewing, food-tasting, politics-discussing friend, and I am confident that will continue in the future, even as we are not living in the same city for the first time in nine years. UW-Madison was the location of my independent formative years, and they would not have been the same without my grandmother, Memop, who I got to see quite often in Madison. She was always interested in my classes, research, and sports, and was dedicated to keeping in touch just as often when I moved to Berkeley. My parents and my brother are a constant, unchanging force in my life. I know that no matter what is going on in my life or theirs, I can call them and rely on their values and perspective for advice, though I also know I could and should have called more, for my own sanity.

Based on the past five years, I truly believe that when you are married, the couple earns the Ph.D. together. My Ph.D. experience would have been infinitely more stressful and altogether less enjoyable if my girlfriend (at the time), Stef, had not chosen to move to Berkeley and forge her own career path while we worked toward marriage. She received my venting frustrations with open ears and relieved my stress with excursions to Bay Area activities, home-cooked meals, and general silliness. She has always been there to support me even though she faces her own day-to-day challenges at work that seem infinitely more difficult than my own. I also never imagined the amount of comfort I would feel from marrying into a second family, the Dulaks, who have welcomed me and treated me as their fourth child.

I hope this Ph.D. experience proves to be worth it to my entire family, and I look forward to the future that will most definitely include more time spent with them all.

1. Introduction

Arguably the most significant challenge facing materials chemists in the 21st Century is the development of technology that enables harvesting of renewable energy sources and efficient storage until the energy is needed.[1,2] As of 2013, approximately 80% of the average global energy consumption rate of 18 TW was still provided by coal, oil, or gas.[3] These fossil resources generate harmful greenhouse gas emissions that are apparent through the steady rise of atmospheric CO_2 concentration.[4-6] Anthropogenic CO_2 emissions[7] are the leading cause of observed and predicted rapid climate change through their effects on rising global temperatures,[8] ocean acidification,[9,10] biological trends,[11] and evolutionary adaptation.[12,13] In order to restrict any further damage by rising levels of greenhouse gases in the Earth's atmosphere, new carbon-free energy storage media must be developed. Molecular hydrogen (H_2) is the most prominent example of carbon-free chemical energy storage in a molecule's bonds.[14] In a larger context, use of H_2 as a fuel is one segment of the water cycle, a potentially sustainable succession of splitting water to form hydrogen and oxygen (O_2) and then oxidizing H_2 to regenerate water. The water cycle is highly favored as a sustainable energy foundation for society compared to the carbon cycle. The long-term carbon cycle is the process in which biomass is converted to fossil fuels over millions of years, while the combustion of those fuels to CO_2 is comparatively instantaneous, occurring during the past ~250 years of industrialization.[15-19] Therefore, though attempts to intervene are being made, such as electrochemical CO_2 reduction or carbon sequestration, the combustion of fossil fuels as the primary source of energy for society is an unsustainable process currently having grave impacts on the Earth's biosphere.

In order to enable a sustainable water cycle, two major pieces of electrochemical technology are required: an electrolyser to split water and a proton exchange membrane fuel cell (PEMFC) to recombine H_2 and O_2, forming clean water while extracting electricity. This dissertation will focus on catalysts for the oxygen reduction reaction (ORR) in a fuel cell, though the electrolyser is equally important to the overall sustainability of the process and many similar electrochemical and design concepts apply to both technologies. If the electrolyser is powered by a renewable source of electricity such as solar or wind, then the use of hydrogen in a fuel cell can be completely carbon- and pollutant-free and sustainable.[20] The first large-scale application of PEMFCs is targeted at the transportation sector. By developing electrolyser and PEMFC technologies, cars, buses, trains, and even planes could be powered by a cleaner energy source than current gasoline and diesel fuels. From the PEMFC point of view, the major challenges to commercialization are the cost and lifetime of state-of-the-art fuel cells.[21]

1.1 Brief Introduction to PEMFCs and ORR Challenges

PEMFCs are typically constructed of five layers, though other variations on the design exist (Fig. 1.1). The central layer is the proton exchange membrane (also known as the polymer electrolyte membrane) that is responsible for conducting protons from the anode to the cathode. On either side of the membrane there is a catalyst layer to perform either the anodic hydrogen oxidation reaction (HOR) or the cathodic ORR. The HOR forms two protons and two electrons from one molecule of hydrogen (Eq. 1.1), while the ORR uses four electrons and four protons to form two molecules of water from one molecule of oxygen (Eq. 1.2).

HOR: $H_2 \rightarrow 2H^+ + 2e^-$ (1.1)

ORR: $O_2 + 4H^+ + 4e^- \rightarrow 2H_2O$ (1.2)

Taken together, the membrane and catalyst layers are typically called a membrane electrode assembly (MEA). Finally, the outer two layers are gas diffusion layers (GDL) responsible for dispersing H_2 to the anode catalyst and O_2 to the cathode catalyst. It is the cathode catalyst, typically platinum-based, that can be identified as the bottleneck for PEMFC performance due to the slower kinetics of the ORR compared to the HOR.[22,23] Higher activity is required in order to lower the cost of the catalyst, and therefore the fuel cell. Higher durability of the catalyst in the oxidizing potential region of the ORR is required to improve the lifetime of the PEMFC.

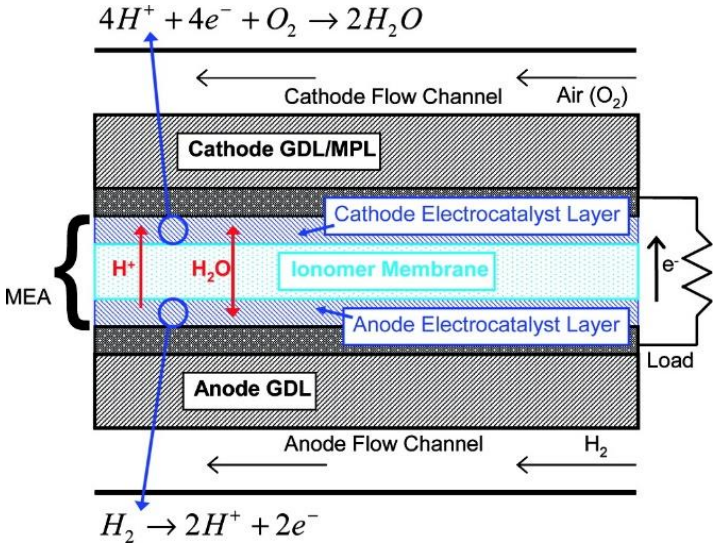


Figure 1.1. Standard assembly of a PEMFC. A PEMFC has a membrane with catalysts and gas diffusion layers. Reprinted with permission from Ref. 21. Copyright 2007 American Chemical Society.

Due to the fact that a model PEMFC or even an MEA is difficult and time-consuming to fabricate, protocols for testing oxygen reduction catalysts have been established using the rotating disk electrode (RDE) technique that allows for higher throughput and kinetic studies. PEMFCs operate in acidic environments in order to achieve optimal kinetics for the ORR and fast proton diffusion across the proton exchange membrane, so acidic electrolyte is used for model RDE tests. The acidic environment greatly reduces the choice of catalysts that can be used for ORR due to many materials' poor chemical stability at low pH (Fig. 1.2). It is well known that Pt is the best single-metal catalyst for the ORR.[24] Among other active monometallic catalysts that are chemically stable in the acidic environment, palladium (Pd) is slightly cheaper than platinum (Pt), though its activity is significantly lower.[25-27] Non-Pt-group metal (PGM) or metal-free catalysts are also an intense area of study, with major focuses on M-polymer composites (M = Mn, Fe, Co, Ni; polymer = polypyrrole, polyaniline),[28,29] M-N_x (x = 2 or 4) pyridinic functional complexes embedded in carbon materials,[30,31] N-doped graphene or carbon nanotubes,[32-36] or metal oxides such as Co_3O_4 or Fe_3O_4 in alkaline electrolyte.[37,38] The common theme throughout the class of carbon-based, non-PGM catalysts is the formation of pyridine functional groups that activates the carbon atom adjacent to the pyridinic N, though other active sites may also be present.[39] Despite these efforts to develop cheaper, highly active ORR catalysts, Pt-based catalysts remain the only practical material to obtain the required PEMFC performance for a fuel cell vehicle.

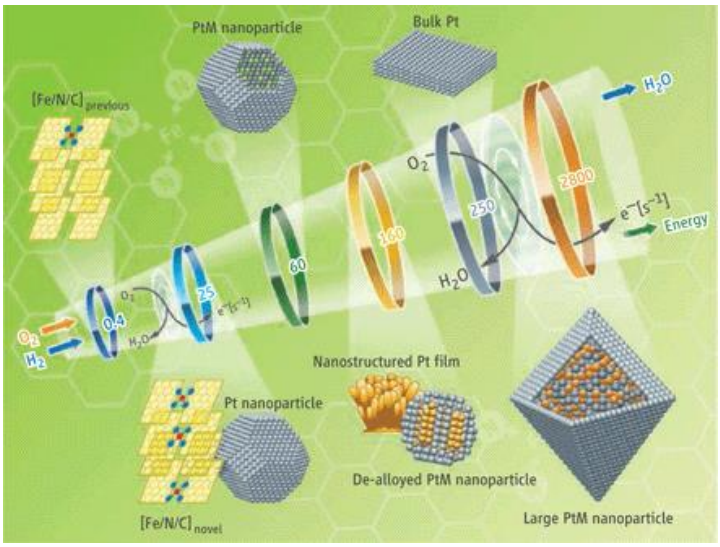


Figure 1.2. Strategies for ORR catalyst design. Pt-based and non-Pt materials, such as Fe-N-C, are intensely studied currently. From Ref. 22. Reprinted with permission from AAAS.

1.2 Rotating Disk Electrode Studies of Model Systems

The RDE method is well-suited for ORR measurements because it is a hydrodynamic technique that accelerates mass transfer of O_2 molecules to the surface of the electrode, minimizing the impact of mass transfer compared to the electron-transfer kinetics that are being studied.[40] Single-crystal studies laid the groundwork for understanding of the electrochemical interface at which the ORR occurs and the structure-sensitivity of the ORR. Studies of (100), (110), and (111) Pt single crystals in potassium hydroxide (KOH), sulfuric acid (H_2SO_4), and perchloric acid ($HClO_4$) revealed the relative structure insensitivity in $HClO_4$ electrolyte compared to KOH and H_2SO_4 (Fig. 1.3).[41-45] Strong adsorption of the bisulfate or sulfate anions in H_2SO_4 on the (111) Pt surface greatly reduces the availability of Pt active sites,[41] while an irreversible oxide forms on the (100) and (110) surfaces in KOH, increasing conversion of O_2 to peroxide instead of water.[42] In order to best model the non-adsorbing nature of the ionomer electrolyte (such as Nafion) used in catalyst layers in MEAs, $HClO_4$ is the best electrolyte for studying the activity of Pt-based catalysts by the RDE method.[43,46,47] The RDE method is used in many laboratories because of its requirements for smaller amounts of catalyst and shorter testing preparation and execution time compared to fabricating MEAs. In order to compare catalyst development across laboratories, certain protocols had to be established for testing nanoparticle (NP) catalysts in the RDE geometry. Pt-based nanoparticle catalysts are typically loaded on a carbon support, which is a prominent area of research in itself that produces many types of support materials.[48,49] One of the most popular carbon supports for ORR catalyst testing is Vulcan XC-72 from Cabot Corporation. Once the metal nanoparticle is loaded onto a conductive carbon support, the thin film must be prepared on the rotating disk electrode, which is made of glassy carbon. In some cases, Nafion is used to adhere the catalyst to the electrode, and the properties of these composite thin films have been studied in detail in order to understand the effect that the preparation protocols can have on the final catalyst evaluation.[50-54] Additional practical procedures for the RDE measurement have been thoroughly explored and documented, such as correcting for uncompensated

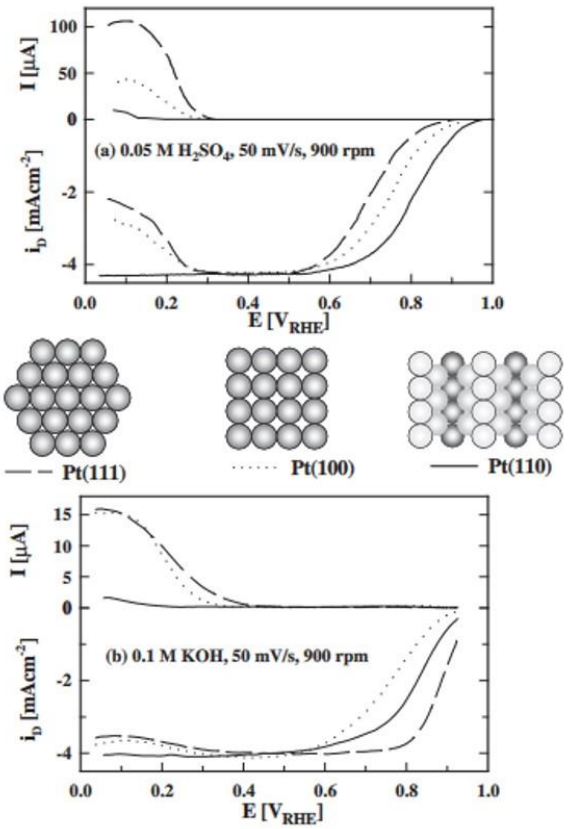


Figure 1.3. Structure sensitivity of the ORR. (a) H_2SO_4 and (b) KOH affect the activity trend on low-index Pt surfaces. Reprinted with permission from Ref. 44. Copyright 2001 John Wiley and Sons.

resistance,[55] eliminating the effects of impurities,[56,57] and the proper, accurate normalization of activity values.[58,59] Surface area normalized activity, a measure of the intrinsic activity of the surface, is typically reported in units of mA/cm^2, where the electrochemical surface area (ECSA) is determined by a Pt-specific technique such as hydrogen underpotential deposition (H_{upd}) or oxidative stripping of CO (CO_{ad}). The efficiency of the Pt utilization in nanoparticle catalysts is described by the specific surface area (SSA) in units of m^2/g_{Pt}. Finally, the mass normalized activity is the product of the SSA and the specific activity and is reported in units of A/mg_{Pt} to convey the quantity of Pt required for a certain PEMFC performance level. The stability of ORR catalysts is measured by performing accelerated durability tests (ADT). New electrochemical techniques such as *in situ* inductively coupled plasma mass spectrometry (ICP-MS) are now being developed for in depth electrochemical characterization of catalyst stability, where the focus again returns to single crystals in order understand nanoparticle catalysts.[60]

1.3 Bimetallic Alloys for ORR Catalysis

One thoroughly investigated strategy for reducing the amount of Pt required in a PEMFC is to alloy it with a less expensive, more Earth-abundant metal, M. In addition to decreasing the Pt mass by replacing some atoms with M, it has been demonstrated in multiple systems that control over composition and surface structure of Pt-M alloys consistently achieves higher specific activity than

pure Pt systems. Initial hypotheses were posited to explain the activity improvement of systems where M is a 3*d* transition metal such as Ti, V, Cr, Mn, Fe, Co, Ni, or Cu. It was observed by X-ray diffraction (XRD) that alloying of the solute M into the face-centered cubic (fcc) lattice of Pt induced contraction of the lattice. This led to the thought that the smaller Pt-Pt bond distance, also observed by extended X-ray absorption fine structure (EXAFS), enhanced the activity, possibly by optimization of the distance required to break an O-O bond.[61-63] X-ray absorption near edge structure (XANES) demonstrated that Pt-M alloys had a larger fraction of *d*-electron vacancies compared to pure Pt, possibly leading to the improved activity.[62-65] Other suggestions were that M was either leached out of the catalyst surface in the acidic electrolyte, creating a rougher surface with more active sites, or that it participated in surface redox processes that enhanced the activity for ORR.[66] Depending on the structure of the catalyst surface, any of these mechanisms could contribute in some manner; however, the most widely agreed upon understanding of the effect of alloying on the activity of Pt-M surfaces relies on the electronic and geometric effects.[67,68] The electronic effect, also known as the ligand effect, refers to the modification of the electronic structure of the surface by M and is typically only believed to be impactful over the first two to three surface layers.[67] The geometric effect, also known as the strain effect, generally refers to the alteration of the surface Pt-Pt distance by inducing compressive or tensile strain in the surface, which has been shown to also alter the surface electronic structure. It is common for both effects to be present in one catalyst system and therefore difficult to distinguish.[69]

In order to understand the mechanism behind ORR activity improvement in Pt-M alloys, one must first understand why pure Pt is not precisely optimized for the ORR. In catalysis, the theoretical understanding of the interaction of a metal surface with an adsorbate molecule/atom is best characterized by *d*-band theory.[70] Fig. 1.4 demonstrates the simplified situation of an adsorbate's interaction with a metal surface.[71] The adsorbate (in a vacuum) has a very sharp density of states that

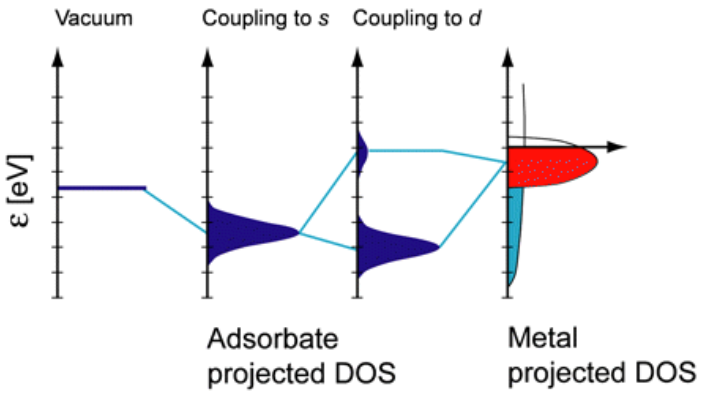


Figure 1.4. Metal-adsorbate interaction. Illustration of the electronic interaction between an adsorbate and a transition metal surface. Reprinted with permission from Ref. 71.

is broadened when it interacts with the metal *s*-band, which is broad compared to the *d*-band. The broadened adsorbate states then interact with the sharp *d*-band, forming bonding and antibonding energetic states between the metal surface and the adsorbate. The main principle of *d*-band theory is that the coupling between the *s*-band and the adsorbate state is similar across a row of transition metals, while the coupling of the adsorbate with the *d*-band is the critical factor determining the strength of the interaction with a given transition metal. The shape and distribution of the density of

states in the *d*-band determine the energy level of the bonding and antibonding states. The energy of the antibonding states relative to the metal's Fermi level determines the filling of the antibonding states, and therefore the strength of the adsorption of the molecule onto the metal surface.[72] For example, if the antibonding states are lower in energy than the Fermi level and are therefore filled, the adsorption interaction will be weak. These bonding and antibonding states can be visualized by performing X-ray emission spectroscopy and X-ray absorption spectroscopy (XAS) on an adsorbate, for the filled and empty states, respectively.[73] Finally, it has been demonstrated that the *d*-band center is a good descriptor of the entire *d*-band density of states.[74] The *d*-band center is a major determinant for the energy of the adsorption interaction, in addition to the filling fraction of the *d*-band and the coupling matrix between the adsorbate and the *d*-band.

There are two major mechanisms suggested for the ORR forming water, where "*" represents an arbitrary adsorption site on the catalyst surface:

Dissociative Mechanism

$$\tfrac{1}{2}O_2 + * \rightarrow O^*$$
$$O^* + H^+ + e^- \rightarrow HO^*$$
$$HO^* + H^+ + e^- \rightarrow H_2O + *$$

Associative Mechanism

$$O_2 + * \rightarrow O_2^*$$
$$O_2^* + H^+ + e^- \rightarrow HOO^*$$
$$HOO^* + H^+ + e^- \rightarrow H_2O + O^*$$
$$O^* + H^+ + e^- \rightarrow HO^*$$
$$HO^* + H^+ + e^- \rightarrow H_2O + *$$

In either mechanism, the catalyst must bind intermediates through the oxygen atom. The adsorption energies of oxygenated intermediates (O*, HO*, HOO*) scale linearly due to the common binding motif between the metal atom and an oxygen atom, thereby creating a volcano relationship between activity and binding strength of oxygen.[75-77] This is otherwise known as the Sabatier principle of catalysis, which states that the ideal catalyst cannot bind the reaction intermediates too strongly nor too weakly, forming the volcano that has peak activity at an optimized binding strength. It is generally accepted that Pt binds oxygenated species too strongly compared to what would allow for maximum ORR turnover rate (Fig. 1.5).[24,76] Nørskov et al. demonstrated via density functional theory (DFT) calculations on a Pt(111) surface that without sufficient overpotential, O* adsorbed on Pt is too stable and cannot be protonated to form water.[24] Therefore, in the case of the ORR, O* is too strongly bound to Pt, allowing oxygenated species to poison the surface, while a catalyst that binds too weakly is not capable of adsorbing and/or dissociating the O_2 molecule. The adsorption energies of initial and final intermediates dictate the reaction energy for a given step in the reaction mechanism. The Bronsted-Evans-Polanyi relationship illustrates that the activation energy of a given reaction is linearly correlated to the reaction energy such that the reaction kinetics can be directly related to the adsorption strength of a given intermediate.[75,78] Consequently, the reaction kinetics of the ORR can be compared on various transition metal surfaces and directly attributed to their binding strength to oxygenated intermediates, which is directly related to their surface electronic structure, including their *d*-band center.[79]

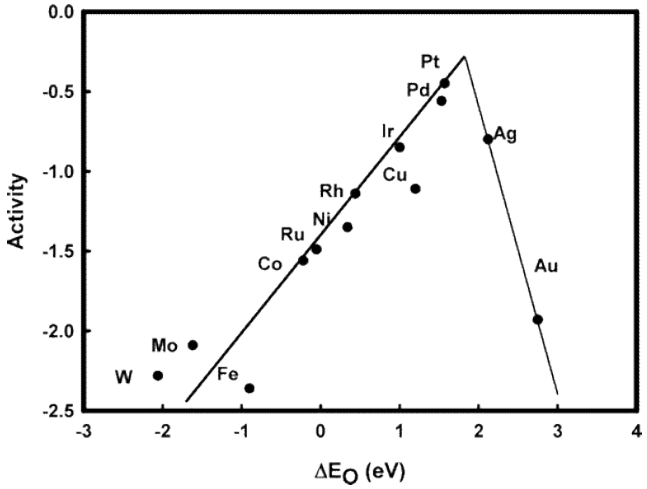


Figure 1.5. ORR Volcano plot. The plot is constructed from DFT calculations of the oxygen binding energy to a metal surface. Reprinted with permission from Ref. 24. Copyright 2004 American Chemical Society.

While pure Pt binds oxygenated adsorbates too strongly, many Pt-M alloys are able to reduce the binding strength of the oxygenated adsorbates in order to increase the rate of the ORR. In most cases, a combination of the electronic and geometric effects has tuned the position of the *d*-band center of the catalyst surface to a lower energy compared to that of Pt. This causes greater filling of metal-adsorbate antibonding states, weakening the adsorption interaction. For Pt-M alloys, the lowering of the *d*-band center with respect to the Fermi level has been shown by DFT[67,80] and valence band measurements by ultraviolet photoelectron spectroscopy[81-83], with combination of the two methods demonstrating the correlation between *d*-band center position, oxygen binding strength, and ORR activity.[84,85] The precise surface atomic structure of the alloy plays a pivotal role in the activity enhancement that can be achieved.

Initially, simple surface alloys with randomly distributed Pt and M on the surface were synthesized, and some instability was observed due to leaching of non-noble M atoms.[61-63,69,86] A significant improvement in surface structure was later discovered, termed "Pt-skin," to describe a smooth, pure Pt surface atomic layer over an M-rich subsurface layer.[87,88] The formation of Pt-skin takes advantage of the tendency for Pt to surface segregate when given the required thermal energy for diffusion because of its lower surface energy compared to 3*d* transition metals.[89-93] The Pt-skin discovery culminated in the seminal report by Stamenkovic et al. that showed an order of magnitude improvement in the specific activity of a $Pt_3Ni(111)$ single-crystalline surface with Pt-skin formation over that of a Pt(111) surface (Fig. 1.6).[82] Though attempts have been made through DFT calculations to decouple one portion of activity enhancement, due to the compressive strain of Pt-skin, from a second portion, due to the ligand effect of the M-rich second atomic layer,[94] it remains difficult to experimentally separate the geometric and electronic effects. A DFT survey of many alloys revealed theoretical compositions that could have the proper binding characteristics for high ORR activity; however, very few of these compositions are thermodynamically stable in the oxidizing potential region and acidic conditions of the ORR.[95] Therefore, research has been mainly limited to Pt and Pd-based alloys with Pt or Pd enriched on the surface.[96] In addition to the aforementioned Pt-M alloys where M = Ti, V, Cr, Mn, Fe, Co, Ni, or Cu, there is another class of alloys in which M = Sc, Y, or a

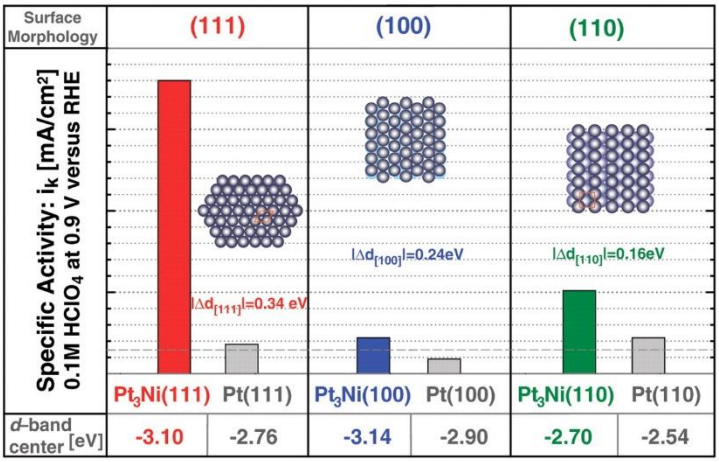


Figure 1.6. Pt-skin effect. Activity enhancement for three low-index surfaces of Pt_3Ni with Pt-skin formation compared to pure Pt single crystals. A comparison of the experimentally measured *d*-band centers is also shown. From Ref. 82. Reprinted with permission from AAAS.

lanthanide metal.[76,97-99] In this series, the size of M tunes the compressive strain of a Pt overlayer, which forms after dissolution of M from the alloy surface. The Pt overlayer is a few atomic layers thick, definitively thicker than the overlayer defined as Pt-skin by Stamenkovic et al. By varying the identity of M, the amount of compressive strain in the Pt overlayer was optimized in Pt_5Tb and Pt_5Gd.[99] DFT studies have demonstrated that compressive strain causes increased overlap of metal *d* orbitals, resulting in a broadening of the *d*-band, lowering of its center, and weakening of the surface binding strength.[74,100]

While mechanistic studies of catalytic enhancement are generally difficult, model systems such as single-crystalline $Pt_3Ni(111)$ with Pt-skin provide the best opportunity to understand how the surface increases the turnover rate of the ORR. To this point, the effect of lowering the *d*-band center further below the Fermi level on the binding strength of oxygenated adsorbates to Pt surfaces has been discussed. It was suggested that lowering this binding strength, which scales linearly for adsorbates such as O*, HO*, and HOO*, can lower the activation energy of the reaction, thereby improving the kinetics.[24] While this effect should certainly be considered, a related mechanism has also been proposed and supported by experiment. The concept is that the $Pt_3Ni(111)$ surface demonstrates reduced coverage of oxygenated adsorbates compared to a pure Pt(111) surface, allowing more open Pt sites to perform ORR.[82] A general rate expression (Eq. 1.3) has been proposed for the ORR on Pt surfaces:

$$i = nFKC_{O_2}(1 - m\Theta_{ad})^x \, e^{\frac{-\beta FE}{RT}} \, e^{\frac{-\gamma r\Theta_{ad}}{RT}} \qquad (1.3)$$

In this expression, i is the current measured at a certain potential E, n is the number of electrons per reaction, F is the Faraday constant, K is the rate constant, C_{O_2} is the concentration of dissolved oxygen in the electrolyte, Θ_{ad} is the surface coverage by adsorbed species, m is the fraction of adsorbed species that are HO*, x is the order of the reaction with respect to the number of active Pt sites, β and γ are symmetry factors assumed to be 0.5, $r\Theta_{ad}$ characterizes the rate of change of the free energy of

adsorption with the surface coverage of adsorbed species, R is the universal gas constant, and T is the temperature. Detailed kinetic studies demonstrated that the Tafel slope and activation energy of the ORR were similar on Pt, Pt_3Ni, and Pt_3Co, leading to the conclusion that K and the two exponential terms in the rate expression are very similar for these surfaces.[87,88] Therefore, the activity enhancement on Pt-skin surfaces must be explained by the pre-exponential term that describes the coverage of adsorbed oxygenated species on the surface. By reducing the number of adsorbed HO* and O* poisoning the surface, more Pt sites are available to perform ORR. This is consistent with the lower *d*-band center of Pt-skin surfaces that induces weaker binding of adsorbates to Pt-skin.[82,101] After this new perspective on the mechanistic differences between Pt-M and Pt surfaces, oxygenated species were observed on Pt surfaces by ambient pressure X-ray photoelectron spectroscopy (APXPS) in a model fuel cell compatible with the spectroscopic technique. The complexity of the electrochemical interface was described by supporting DFT simulations of various hydration environments of the adsorbed oxygenated species.[102]

1.4 Design of Nanostructured Catalysts for ORR

The excellent electrochemical, structural, and surface characterization performed on model systems such as single crystals has guided the design of practical nanostructured catalysts for the ORR. When applying bulk design principles to the nanoscale, the first consideration must be the effect of the particle size on the activity and durability of the catalyst. A single crystal has a quasi-infinite terrace surface with only limited defect step or kink sites (Fig. 1.7), while a nanoscale surface will inherently be terminated by edges and corners where step and kink sites are prevalent. As the nanoscale features become smaller, the density of these lower-coordinated sites will increase.[103] Mayrhofer et al. demonstrated that the potential of zero charge shifts more negative as Pt particle size decreases, meaning the smaller nanoparticles have slight positive charge on their surfaces. Therefore, the coverage of oxygenated adsorbates increases on smaller particles. As could be expected based on the previous discussion, the increased coverage of HO* leads to lower ORR specific activity on smaller Pt nanoparticles.[104,105] DFT studies have demonstrated that edge or step sites are the location of stronger binding of oxygenated species.[106] Combined DFT and experimental studies showed that in order to obtain the highest mass activity, there is a compromise between decreasing specific activity and increasing SSA of smaller nanoparticles,[107] though the optimal size is not necessarily agreed upon and may be different for various nanoparticles.[108]

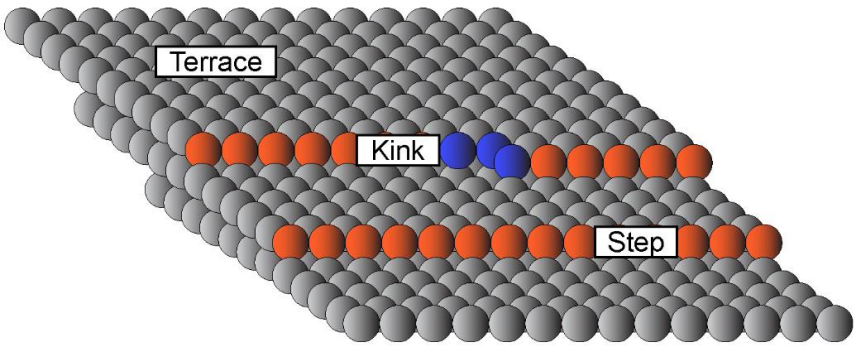


Figure 1.7. Basic types of metal surface sites. Illustration showing terrace (gray), step (orange), and kink (blue) sites on a metal surface.

The goal of nanoparticle design for ORR is to obtain the highest specific activity on a nanostructure with high SSA. If these two conditions are met, then the mass activity will be high with the potential to be used in a PEMFC. The mass normalization is always reported by mass of noble metal used (Pt, Pd, Ir, Rh, Os, Ru, Re, Au, Ag) because only the most expensive, rare elements are of concern to fuel cell commercialization. Therefore, one obvious strategy to reduce the precious metal loading is to use only a single monolayer (ML) of Pt atoms on the surface of another metal. The protocol for making Pt ML catalysts is to perform Cu underpotential deposition (Cu_{upd}) onto a metal surface and subsequent galvanic replacement of the Cu with Pt. Cu_{upd} can only be performed on noble metals, so the concept was initially demonstrated on single crystals of precious metals. The *d*-band center and O* binding strength were calculated by DFT and correlated with the experimental activity, with Pt ML/Pd(111) being the only substrate that outperformed the Pt(111) control.[109] An alternative strategy was developed to reduce the precious metal content by inducing surface segregation of the precious metal in an alloy with a non-precious metal, and then performing Cu_{upd} on the precious metal surface. Nanoparticle substrates such as Au-Ni, Pd-Fe, Pd-Co, and Pd-Au have been used for depositing a Pt ML.[110-112] A solution based reduction of Pt can also be used to deposit multiple Pt monolayers onto a substrate nanoparticle, often Pd.[113] This method has been used by Xia et al. and Li et al. in a number of different geometries including cubes,[114] octahedra,[115] and icosahedra[116], even leading to hollow nanocage geometries by etching of the Pd through pinholes in the Pt shell (Fig. 1.8).[116-118] A different strategy for obtaining high surface area geometry is the growth of dendritic structures, also often carried out in the Pt-Pd system.[119,120] However, in general, the Pt-Pd alloys discussed at length here suffer from low specific activity due to less impactful geometric and ligand effects from Pd, which is more similar in size and electronic structure to Pt compared to 3*d* transition metals.

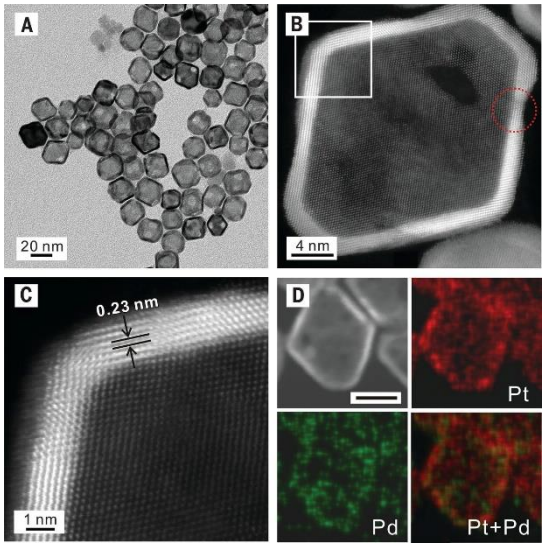


Figure 1.8. Atomic layer deposition of Pt on Pd. Hollow Pt-Pd alloy octahedral nanocage with ultrathin walls after etching of Pd template. From Ref. 117. Reprinted with permission from AAAS.

Pt-Pd nanoparticles have demonstrated enhancement in stability during ADTs due to the sacrificial oxidation of Pd, which preserves the Pt shell.[111] A similar strategy for nanoparticle design is the process of dealloying popularized by Strasser et al. However, dealloying is performed as an activation step before utilization of the catalyst, creating a thick Pt shell on the surface of Pt-Cu, Co, Ni, or ternary

catalysts. The thick Pt shell can protect the 3*d* transition metal in the core of the nanoparticle, preserving its activity. These catalysts are typically synthesized through simple impregnation of a Pt/C catalyst with M precursor, followed by freeze-drying and annealing to alloy Pt and M.[121] Dealloying can be performed electrochemically or by chemical corrosion, and a procedure was developed in order to prepare catalyst for use in an MEA without contaminating the membrane with M cations.[122,123] The strain of the Pt shell could be tuned depending on the initial composition of a Pt-Cu alloy, thereby influencing the oxygen binding strength and the ORR activity.[124] Another approach to improve the stability of the nanoparticle is to induce intermetallic ordering of two metals within the lattice. Intermetallic ordering can only be easily achieved in a few systems such as Pt_3Co and PtFe as it requires rather high temperature. Pt_3Co intermetallic nanoparticles were achieved by annealing at 700 °C and demonstrated enhanced activity and stability over identical nanoparticles that were only annealed at 400 °C. The activity improvement was attributed to the Pt surface segregation that occurred at higher annealing temperature.[125] The durability of intermetallic nanoparticles is generally believed to be due to the more negative enthalpy of formation of the intermetallic lattice as compared to a disordered alloy, reducing oxidation and dissolution of the non-noble M atom.[126] PtFe nanoparticles were also synthesized as a disordered alloy and annealed at 700 °C in order to induce the disorder-to-order transition, which led to enhanced ORR activity and durability.[127] One final strategy for enhancing the durability of nanoparticles is the incorporation of Au, which has been demonstrated beneath ORR-active Pt-Fe and Pt-Ni shells. Using a solid Au core underneath a Pt-Fe shell, stability up to 60,000 cycles was demonstrated (Fig. 1.9).[128] It was later shown that only 5 atomic percent Au was required between a Ni core and PtNi shell to achieve stability over the course of 10,000 cycles.[129] Au beneath

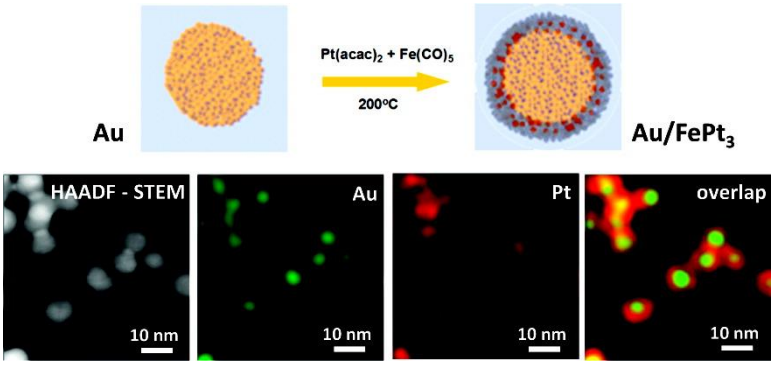


Figure 1.9. Au enhancement of ORR stability. Au nanoparticles coated with a $FePt_3$ shell demonstrate excellent stability after an accelerated durability test for the ORR. Reprinted with permission from Ref. 128. Copyright 2011 American Chemical Society.

a Pt-M surface is believed to inhibit the place-exchange mechanism in which oxygen penetrates the first layer of Pt after continuous cycling, oxidizing the M atom. Au is highly resistant to oxidation, explaining the suppression of the place-exchange mechanism and allowing the Pt-M shell to maintain its high specific activity.

Arguably the most prevalent and elegant strategy for controlling activity of nanoparticle catalysts for the ORR is the design of the shape of bimetallic alloys.[130-133] Nanoparticle shape control has been most thoroughly explored for noble metals such as Pd, Pt, Ag, and Au, but has been gradually extended to other materials to demonstrate catalytic activity dependence based on the shape, typically due to the

facet that was exposed.[134-139] Shape-controlled Pt nanocrystals have been applied to the ORR,[140-142] and while some activity enhancement was demonstrated for octahedra due to their dominant (111) surface faceting, the shapes are generally unstable under durability tests, leading to spherical particles with similar activity regardless of the initial shape.[143] Less well-controlled Pt-based nanostructures such as branches, urchins, flowers, and porous structures have also been studied because of their propensity to provide new types of surfaces not present on well-defined nanoparticles.[144-146] However, their non-uniform nature makes it more difficult to elicit the origin of their catalytic performance. One example that approximated a well-defined system was the evaporation of metal alloys onto molecular solid whiskers, producing nano/mesostructured thin films on which surfaces resembling Pt-skin could be created.[147,148] The emergence of Pt-skin surface features and the discovery of the highly active $Pt_3Ni(111)$ single-crystal surface[82] led to the rapid pursuit of Pt-Ni octahedra with the expectation that they could provide Pt-skin surfaces on their (111) facets. Standard organic surfactants could only produce truncated Pt-Ni octahedra[149] until it was discovered that CO was a critical ligand for synthesizing near-perfect octahedra.[150-152] Strasser et al. studied a separate system of Pt-Ni octahedra synthesized with only dimethylformamide as the surfactant and solvent.[153] However, they found that the (111) facets of Pt-Ni octahedra tend to be enriched in Ni, leading to very poor stability of the shape in the acidic electrolyte (Fig. 1.10).[154] It was discovered that the Ni-enrichment of the (111) facets was likely due to the growth mechanism in which anisotropic Pt hexapod structures first grew that were then filled in by Ni.[155-157] Pt-Ni octahedra have certainly provided large increases in ORR activity;[158] however, they have not lived up to the promise of the original single-crystal studies due to their surface structure that is very different from that of the $Pt_3Ni(111)$ Pt-skin.

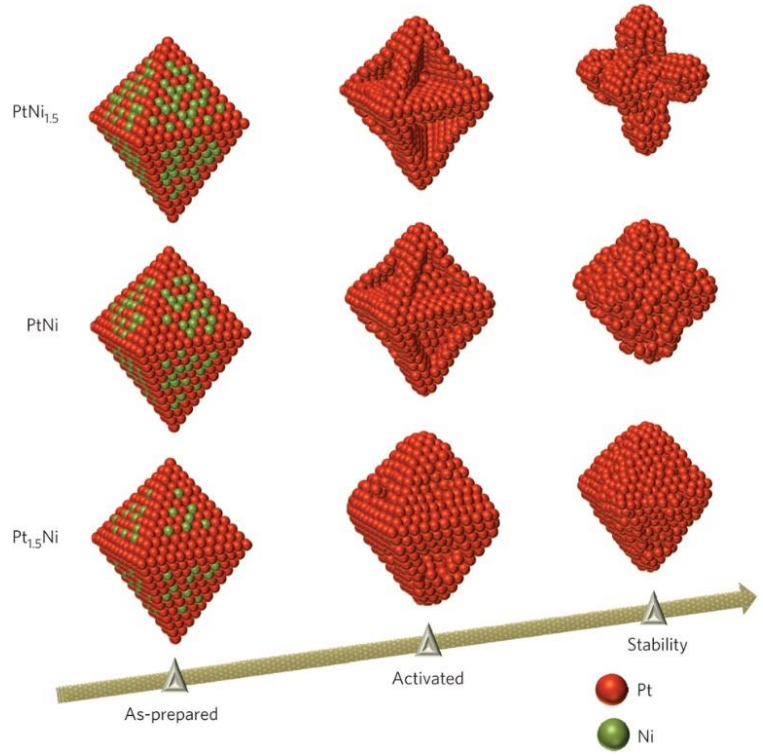


Figure 1.10. Dealloying trends in Pt-Ni octahedra. Activation and degradation characteristics of Pt-Ni octahedra with various initial compositions. From Ref. 154. Reprinted by permission from Macmillan Publishers Ltd: Nature Materials, copyright 2013.

While the advantageous Pt-skin structure has been difficult to form on octahedra, monodisperse spherical nanoparticles have shown some promise.[159] Size-controlled Pt_3Co nanoparticles were synthesized to determine the size with maximum mass activity and the optimal annealing pretreatment protocols.[108,160] Composition and size control was implemented to show that Pt_3Co and Pt_3Ni were essentially equally promising as nanoscale compositions for the ORR.[161] The study of different compositions of Pt-Ni alloy nanoparticles led to the conclusion that PtNi was the optimum composition for obtaining a Pt-rich surface with highest specific activity,[162] and subsequent annealing treatment enabled the formation of the first nanoscale Pt-skin surface (Fig. 1.11).[163,164] Nanoscale Pt-skin surfaces can be identified electrochemically by performing oxidative stripping of H_{upd} and CO_{ad}. Both molecules specifically adsorb onto Pt surfaces with one molecule per Pt atom, though on Pt-skin surfaces, the H_{upd} coverage is reduced due to the lower *d*-band center position. Therefore, the ratio of charge passed during the oxidative stripping of the two adsorbates is 1.0 for a pure Pt surface, while on a Pt-skin surface the ratio increases to 1.5.[165]

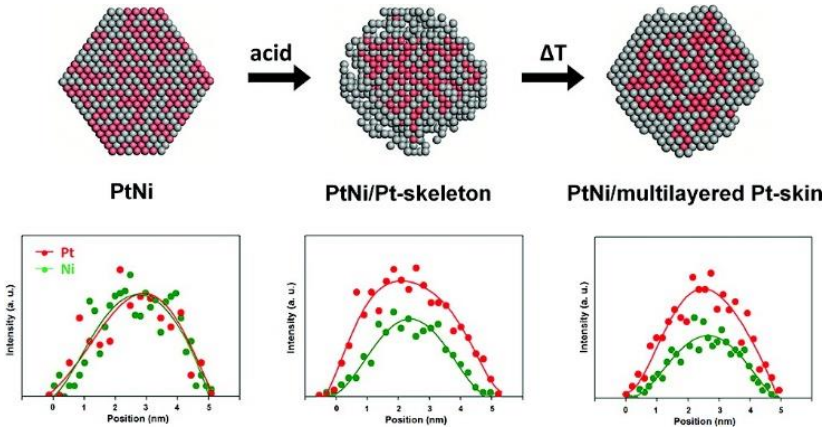


Figure 1.11. Nanoparticle Pt-skin formation. Formation of multilayered Pt-skin surface on PtNi nanoparticles with energy dispersive x-ray spectroscopy line scans demonstrating the surface Pt enrichment. Reprinted with permission from Ref. 163. Copyright 2011 American Chemical Society.

By control over size, shape, and composition, novel and complex nanostructures can be designed with specific catalytic properties. Central to this dissertation is the design of highly open, three-dimensional, multimetallic Pt-based nanoframes (NF) for the ORR. Monometallic frames or cages could be synthesized by preferential etching of a specific facet of a shaped nanoparticle,[166] and selective etching was also used to remove the core from a core-frame bimetallic heterostructure.[167-169] The more common early method to synthesize nanoframes, branching off the rich literature on shape-controlled noble metal nanoparticles, was the galvanic replacement of a template, often Ag, with a more noble metal, often Au.[170-174] However, these methods left room for improvement in the regions of shape, size, and surface uniformity due to the aggressive, poorly controlled galvanic replacement method. One-pot methods increased in popularity because bimetallic nanoparticles could be synthesized with high mono-dispersity and control over the elemental positioning in order to etch the less noble element, producing a nanoframe. Based on the number of reports and shapes of Cu-based nanoframe syntheses, it is apparent that Cu is a beneficial choice to alloy with Pt because of its crystal structure (fcc), reduction potential, and high mobility.[175-185] The Pt-Cu nanoframe system often takes advantage of the Kirkendall effect,[186] which is the faster diffusion outwards of one atom than another, to form

the hollow frame. However, Pt-Cu alloys have not demonstrated nearly as much promise for the ORR as their Ni and Co counterparts. In 2014, Yang et al. reported a one-pot synthetic method for $PtNi_3$ rhombic dodecahedral nanocrystals that had Pt enriched on their edges such that, when the nickel was spontaneously oxidized and corroded, a single-crystalline, three-dimensional, rhombic dodecahedral Pt_3Ni nanoframe remained (Fig. 1.12).[187] The Pt_3Ni nanoframe set a record for nanoscale ORR activity at the time and catalyzed a rapid growth in nanoframe reports including some within the Pt-Ni composition space.[188-191] In this dissertation, the nanoframe system as reported by Yang et al. is further explored for its expansion to other compositions and shapes as well as the underlying synthetic mechanisms that enable the highly open, three-dimensional structure to be designed with high catalytic activity for the ORR.

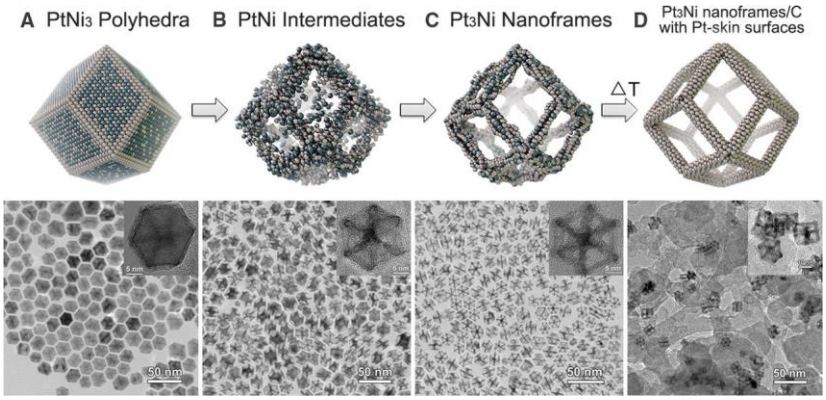


Figure 1.12. Pt_3Ni nanoframe discovery. (a) Rhombic dodecahedral $PtNi_3$ nanoparticles are etched through a (b) intermediate composition into (c) Pt_3Ni nanoframes that can be (d) annealed to form Pt-skin for high ORR activity. From Ref. 187. Reprinted with permission from AAAS.

2. Pt_3Co Nanoframes

Portions of the content and figures of this chapter are reprinted or adapted with permission from N. Becknell, C. Zheng, C. Chen, Y. Yu, P. Yang, "Synthesis of $PtCo_3$ polyhedral nanoparticles and evolution to Pt_3Co nanoframes", Surf. Sci., 2016, 648, 328. DOI: 10.1016/j.susc.2015.09.024. Copyright 2016 Elsevier B.V.

2.1 Preface

Following the discovery of Pt_3Ni nanoframes,[187] there was great intrigue into the variety of compositions that were possible in this synthetic system and could provide new functionality. The nanoframe synthetic mechanism is complex and highly dependent on a number of variables, so the extension to a new Pt-based alloy was not trivial. Cobalt was the first new metal attempted as it is the most similar to nickel among the 3*d* transition metals. In Chapter 2, the Pt-Co nanoframe synthesis is established and the differences and similarities of the Pt-Co system are compared to the Pt-Ni system.

2.2 Introduction

The importance of nanocrystal synthesis has been emphasized by the applications of nanocrystals in a vast array of fields including catalysis,[192,193] semiconductors,[194] electronics,[195] plasmonics,[196] and magnetism.[197,198] The nature of nano-sized metallic or semiconducting materials affords them unique and beneficial properties compared to their bulk counterparts. The ability to control the shape and structure of nanoparticles (NP) can greatly enhance and clarify structure-dependent trends in their properties;[135,199,200] when two or more metals are incorporated into a single particle, the possibilities for structural control of the particle expand significantly. Bimetallic NPs have been synthesized with various geometries including core-shell,[136] random distribution, and heterogeneous distribution.[201] By incorporating two metals into a nanoparticle, the capabilities of the nanoparticle can be diversified due to the synergistic interactions between the two different metals.

Yang et al. have employed both homogeneous and heterogeneous distributions of elements in bimetallic particles to achieve significant enhancements in catalytic activity for electrochemical carbon dioxide reduction[202] and oxygen reduction.[187] In the latter case, a $PtNi_3$ rhombic dodecahedron was synthesized with heterogeneous distribution of platinum to the edges of the three-dimensional shape. Nickel was then preferentially oxidized from the faces and interior of the polyhedron, leaving a hollow nanoframe (NF) with three-dimensional catalytically active surfaces on the interior and exterior of the frame. This work demonstrated a novel method for obtaining a NF by synthesizing a bimetallic NP with heterogeneous distribution of the two elements. This method enables the synthesis of an alloy which can convert from Pt-poor to Pt-rich composition while maintaining the rigid structure of the edges of the shape. Previous work on hollow NF structures involved galvanic replacement of a template nanostructure with a more noble metal,[167,170,172,174] sequential growth of metal on the edges of a template shape,[169] or direct solvothermal synthesis of a hollow NF.[175,177] More recently, additional work has been done on the synthesis of bimetallic NPs with heterogeneous distribution of a noble metal to the edges of the shape.[178,188-190] However, to this point, no work has been reported on the synthesis of platinum-cobalt bimetallic NFs.

Platinum-cobalt bimetallic alloys have been extensively studied for their magnetic properties[203,204] and enhanced catalytic activity for the ORR.[94,108,125,151,159-161,205] The Pt_3Co phase was synthesized with high monodispersity by reduction of platinum acetylacetonate with concomitant decomposition of cobalt carbonyl.[108,203] Ordered PtCo NPs have been synthesized by solution-phase methods, which typically result in a disordered face centered cubic structure, and subsequent high temperature annealing to produce the ordered tetragonal PtCo phase.[206] There are very few reports of solution phase synthesis of $PtCo_3$ NPs.[207] In fact, the platinum-cobalt phase diagram is still in debate, with some suggesting a $PtCo_3$ ordered phase should be possible,[208] similar to $PtNi_3$, and others asserting that it is not a stable phase and that the solid solution composition of 75% cobalt is similarly unfavorable.[209] This is understandable considering that at temperatures below 450°C, cobalt prefers its epsilon hexagonally close-packed phase.[210] It is well known that platinum strongly prefers cubic close-packing structure, so cobalt-rich platinum alloys are naturally difficult to stabilize and the more stable PtCo or Pt_3Co phases are typically preferred. The synthesis of a cobalt-rich Pt-Co polyhedron was developed because the NP must be cobalt-rich in order to make a sufficiently hollow NF by leaching of the Co. Through this synthesis and evolution process, the first synthesis of a Pt-rich, platinum-cobalt alloy nanoframe is reported.

2.3 $PtCo_3$ Nanoparticle Synthesis

$PtCo_3$ NPs were synthesized by hot-injection of Pt and Co precursors into a mixture of oleylamine and oleic acid (see Appendix A1.1). A typical transmission electron microscopy (TEM) image of the as-synthesized $PtCo_3$ polyhedral NP is shown in Fig. 2.1a. The size distribution of the $PtCo_3$ NP was calculated to be 17.1 ± 2.7 nm. The hexagonal projection, characteristic of a rhombic dodecahedron

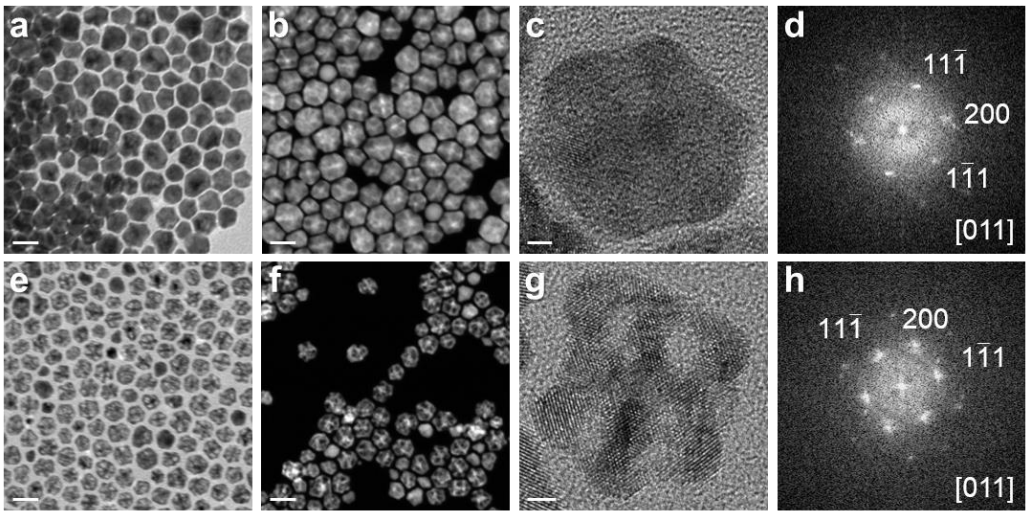


Figure 2.1. TEM of Pt-Co NP and NF. (a) TEM image of $PtCo_3$ NP. (b) STEM image of $PtCo_3$ NP. (c) HRTEM image of a $PtCo_3$ NP and (d) corresponding FFT. (e) TEM image of Pt_3Co NF. (f) STEM image of Pt_3Co NF. (g) HRTEM image of Pt_3Co NF and (h) corresponding FFT. Scale bars in TEM/STEM images are 20 nm. Scale bars in HRTEM images are 2 nm.

in the platinum bimetallic, oleylamine-based system, was primarily observed in TEM though there are other polyhedra which form during the synthesis of the $PtCo_3$ NPs. High-angle annular dark-field (HAADF)-scanning transmission electron microscopy (STEM) imaging was used to screen $PtCo_3$ NPs for the required heterogeneous elemental distribution because it provides significant contrast

difference between atoms of different atomic number.[211] The STEM image of the as-synthesized $PtCo_3$ polyhedra in Fig. 2.1b demonstrates initial proof of segregation of the heavier element, Pt, to the edges of the three-dimensional shape due to the bright contrast which can be seen at the edges.

A few key aspects of the synthesis enabled it to produce these Co-rich polyhedra. A molar ratio of 4.4:1 Co:Pt (in excess of the 3:1 ratio in the product) was required to accelerate reduction of Co^{2+} due to its more negative reduction potential compared to that of Pt^{4+}.[212] In addition, oleylamine acted as a solvent, reducing agent, and surfactant,[213,214] while oleic acid also aided as a surfactant. Oleic acid was introduced into the synthesis to enhance the shape control as it has been shown that oleic acid has a particularly strong affinity for cobalt in many cobalt-based NP syntheses.[198,215-219] Oleic acid has also been found to improve the effectiveness of oleylamine[219] and their synergistic effect was expected based on the slight temperature increase of their solution upon simple mixing of the two surfactants. Without the presence of the oleic acid, the NPs synthesized were significantly more rounded and the size was only 11.9 ± 1.6 nm (Fig. 2.2). This result indicates oleic acid played a key role in stabilizing larger nuclei and sharpening the edges of the polyhedra during the synthesis, a critical point for transformation into the desired hollow NF.

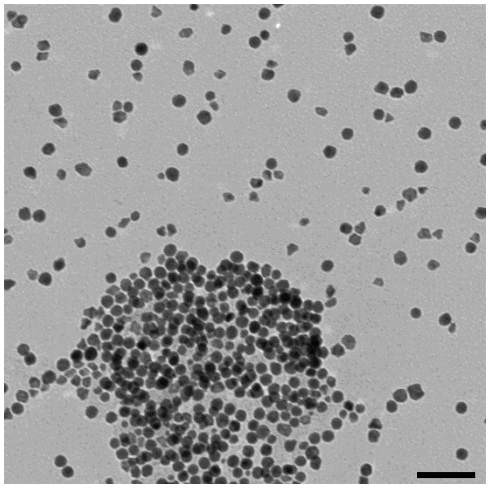


Figure 2.2. Pt-Co NPs without oleic acid. TEM image of NPs synthesized without oleic acid, in the presence of only oleylamine (Scale bar = 50 nm).

2.4 Evolution from $PtCo_3$ Nanoparticle to Pt_3Co Nanoframe

In order to evolve the $PtCo_3$ NP to a Pt_3Co NF, the NPs were dispersed in excess oleylamine and hexadecane and heated at 130°C under air atmosphere (see Appendix A1.2). While sufficiently stabilized by both oleylamine and oleic acid, the NPs are magnetic and do aggregate over a short period of time after washing. During the initial period of heating, the magnetic NPs continued to settle out, requiring intermediate periods of sonication to re-disperse the particles. However, once a sufficient amount of cobalt was removed, the magnetic moment of the particle could no longer be sustained, so aggregation was not severe and sonication was no longer required. TEM and STEM images of the final evolved Pt_3Co NFs are shown in Fig. 2.1e and Fig. 2.1f. The hollow interior of the polyhedral frame can be seen in bright-field and dark-field images. Compared to the NPs, STEM imaging revealed more uniform intensity, or less contrast, over the area of the NFs, indicating more uniform distribution of Pt and Co.

2.5 Structure of $PtCo_3$ Nanoparticle and Pt_3Co Nanoframe

High-resolution transmission electron microscopy (HRTEM) imaging (Fig. 2.1c-d, g-h) and XRD (Fig. 2.3) indicated that the NPs and NFs had the expected fcc structure. In the XRD, the peaks corresponded well with $PtCo_3$ for the NP and Pt_3Co for the NF. These compositions were further supported by energy dispersive X-ray spectroscopy (EDS) and inductively coupled plasma optical emission spectroscopy (ICP-OES) measurements. The NP was determined to be 75% Co and the NF was 25% Co by both ICP-OES and EDS. However, the $PtCo_3$ NP diffraction pattern exhibited asymmetric broadening toward the lower 2Θ side, indicating the possible formation of other Pt-Co alloys. This is expected according to the known phase stability,[209] which favors phase separation to the

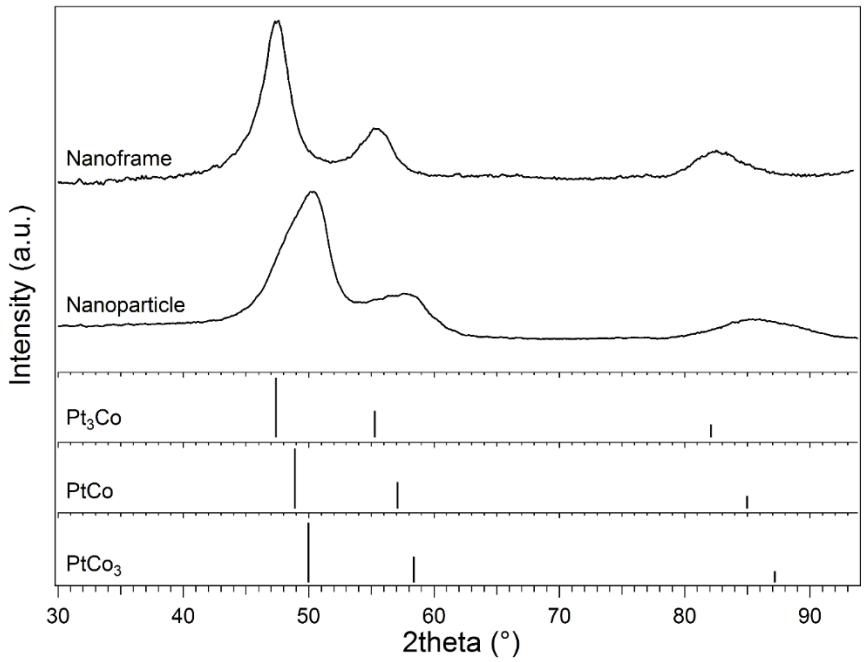


Figure 2.3. XRD patterns of $PtCo_3$ NP and Pt_3Co NF. Diffraction patterns for Pt_3Co (JCPDS 01-072-9178), PtCo (03-065-8970), and $PtCo_3$ (01-071-7411) are shown for comparison.

PtCo composition. Many previous reports illustrate the relatively facile synthesis of Pt_3Co or PtCo phases.[203,206] Additionally, a fcc platinum-cobalt solid solution NP was synthesized with a composition of $Co_{69}Pt_{31}$ and while more Pt-rich compositions were demonstrated, increased cobalt content was not.[214] Even impregnation and high-temperature annealing methods do not produce pure phase $PtCo_3$ NP alloys, but rather a mixture of two or more Pt-Co phases with an average composition of 75% Co and 25% Pt.[205,220-222] For example, Strasser et al. reported via Rietveld analysis that their $PtCo_3$ sample actually consisted of 74.8 ± 2.2 wt% $Pt_{47}Co_{53}$ and 25.2 ± 2.1 wt% Pt_5Co_{95},[220] consistent with the Pt-Co phase diagram reported by Okamoto.[209] Some Pt-rich NP impurities were also observed in Fig. 2.1f. The solid spherical particles remained in the NF sample and these particles exhibit little contrast in the HAADF image, indicating that they were platinum-rich impurity particles in the initial $PtCo_3$ NP synthesis. The diffraction pattern for the NF sample consists of symmetric peaks with significantly less broadening than that observed in the NP XRD pattern. Therefore, after evolution, the sample consists of homogeneous Pt_3Co NFs with some spherical impurities which were likely synthesized as Pt_3Co initially.

2.6 Composition of $PtCo_3$ Nanoparticle and Pt_3Co Nanoframe

HAADF-STEM imaging and corresponding EDS mapping in Fig. 2.4a-d further prove that the $PtCo_3$ polyhedral NPs were synthesized with platinum enrichment on the edges. In the $PtCo_3$ NP, the edges exhibit brighter contrast (Fig. 2.4a) due to the enrichment of the heavier element, platinum. This is corroborated by elemental mapping which shows a cobalt-rich core (Fig. 2.4c) and a platinum framework (Fig. 2.4d) which has formed in the as-synthesized NP. Evolution of this NP yields a NF in which the HAADF imaging contrast is more uniform (Fig. 2.4e) and the elemental mapping demonstrates homogeneous distribution of the elements (Fig. 2.4f-h). The composition of the NPs could also be tracked during the evolution process via quantitative EDS (Fig. 2.5). The measured EDS composition matched well with the XRD and ICP-OES results in that the NP began with a composition of 75% Co, but leaching of the cobalt from the particle during solution-phase oxidation led to a NF with 25% Co composition.

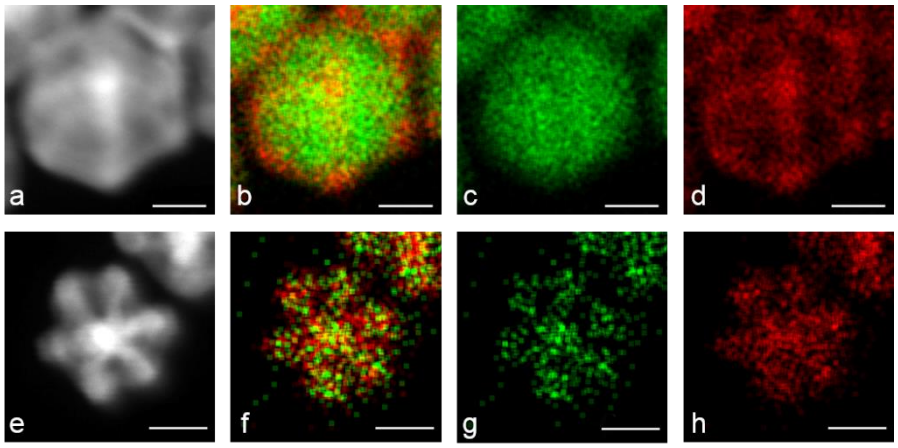


Figure 2.4. Elemental distribution of Pt-Co NP and NF. (a) HAADF-STEM image of $PtCo_3$ NP and (b) corresponding EDS elemental mapping with separate maps shown for (c) Co and (d) Pt. (e) HAADF-STEM image of Pt_3Co NF and (f) corresponding EDS elemental mapping with separate maps shown for (g) Co and (h) Pt. All scale bars are 6 nm.

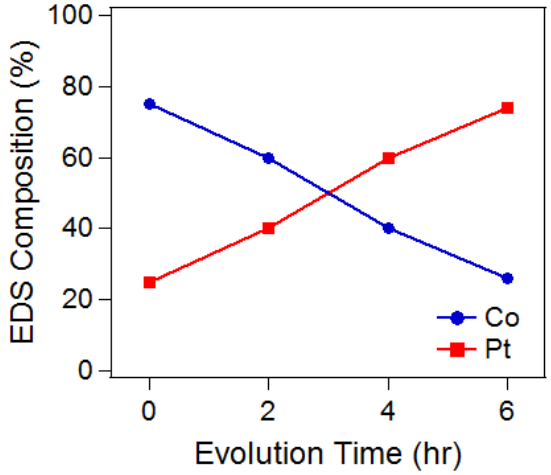


Figure 2.5. Evolution to Pt_3Co NF. Compositional evolution from $PtCo_3$ NP to Pt_3Co NF at 130 °C as tracked by EDS.

2.7 Surface Characterization of $PtCo_3$ Nanoparticle

Further proof of the favorable oxidative leaching process was obtained through APXPS experiments at the Advanced Light Source (ALS) Beamline 9.3.2. Although APXPS is a difficult method for achieving accurate quantification, the general trends of surface composition can be elucidated. The incident photon energy was tuned to 490 eV, corresponding to an inelastic mean free path of approximately 0.9 nm.[223] The changes in surface composition of the $PtCo_3$ NP due to different environments in the APXPS chamber are shown in Fig. 2.6. Initially, it was found that the surface of the $PtCo_3$ NPs may have been slightly enriched in Pt. Annealing of the NP in 100 mTorr H_2 at 120°C only furthered this enrichment of Pt at the surface. Subsequent annealing in 100 mTorr O_2 at 120°C produced a drastic increase in the concentration of Co at the surface of the NP. A similar increase in surface Ni concentration under O_2 was observed in the corresponding $PtNi_3$ nanoparticle.[187] A final annealing step in H_2 served to once again induce surface segregation of Pt in the $PtCo_3$ NP. These results demonstrate the ability of cobalt to surface segregate and be oxidized under an air atmosphere at moderately high temperature in these NPs. Therefore, the removal of cobalt from the $PtCo_3$ NP and evolution to the hollow Pt_3Co NF was able to proceed quite easily and over a short period of time.

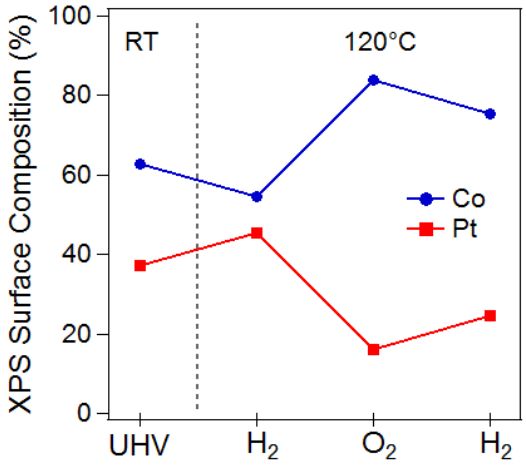


Figure 2.6. Surface segregation in $PtCo_3$ NP. APXPS quantitative analysis of surface composition. Initial spectrum was taken at approximately 10^{-9} Torr (UHV) at room temperature (RT). Subsequent annealing was performed in 100 mTorr of H_2 or O_2 while the sample was heated at 120 °C.

2.8 Conclusions

$PtCo_3$ NPs with segregation of platinum to the edges of their polyhedral shape were synthesized by co-reduction of platinum and cobalt precursor salts. Shape control was achieved by utilizing a dual surfactant system of oleylamine and oleic acid. Due to the heterogeneous distribution of the elements in the polyhedron, cobalt was able to easily oxidize as shown in APXPS experiments. This allowed for leaching of cobalt from the NP and evolution to a hollow NF by solution-phase oxidation. The hollow Pt_3Co NF is the first platinum-cobalt alloy nanoframe and could have important applications in areas such as catalysis. Specifically, the alloy composition and framework structure could potentially provide excellent ORR activity which is currently under investigation.

3. Atomic Structure of Nanoframes

Portions of the content and figures of this chapter are reprinted or adapted with permission from N. Becknell, Y. Kang, C. Chen, J. Resasco, N. Kornienko, J. Guo, N. M. Markovic, G. A. Somorjai, V. R. Stamenkovic, P. Yang, "Atomic Structure of Pt3Ni Nanoframe Electrocatalysts by in situ X-ray Absorption Spectroscopy", J. Am. Chem. Soc., 2015, 137, 15817. DOI: 10.1021/jacs.5b09639. Copyright 2015 American Chemical Society.

3.1 Preface

The Pt_3Ni nanoframe was believed to have extremely high ORR activity due to its high surface area, three-dimensional structure and the formation of Pt-skin on its surface.[187] However, additional evidence of the Pt-skin and general surface characteristics was required in order to understand some variability in activity from batch to batch of Pt_3Ni nanoframes. In Chapter 3, the surface structure of Pt_3Ni nanoframes is explored *in situ* through X-ray absorption spectroscopy.

3.2 Introduction

A major breakthrough in ORR catalyst design was made in the discovery that the formation of Pt-skin—a single atomic layer of platinum—over the surface of a $Pt_3Ni(111)$ single crystal through high-temperature annealing led to an order-of-magnitude increase in specific activity over the Pt(111) single-crystal surface.[82] The significant increase in activity was attributed to the alteration of the surface electronic density of states due to the segregation of platinum to the surface and nickel to the subsurface layer. This results in a lower center of gravity for the surface *d*-band states with respect to the Fermi level, which weakens the binding energy between adsorbates and the Pt-skin surface.[72,83,84] Pt-skin can be identified by ECSA estimation via H_{upd} and carbon monoxide electrooxidation (CO_{ad}).[50,51,165] On a Pt-skin surface, underpotentially deposited hydrogen exhibits lower surface coverage due to weakened binding, which leads to underestimation of the ECSA. However, the ECSA obtained from electrooxidation of CO_{ad} experiments, or CO-stripping, remains unaffected. This phenomenon yields a characteristic value of the ratio between ECSA determined from CO_{ad} and H_{upd} (CO_{ad}:H_{upd}) of approximately 1.5. This has proven to be an easy way to identify formation of the Pt-skin surface structure over Pt_3Ni electrocatalysts.

Many attempts have been made to replicate the surface conditions of the $Pt_3Ni(111)$-skin at the nanoscale in order to utilize the high specific activity of the Pt-skin surface and obtain nanocatalysts with uniquely high mass activity.[148-154,163,224,225] The Pt_3Ni nanoframe reported by Yang et al. is one of few that have successfully obtained Pt-skin segregation at the nanoscale. After annealing of the nanoframe, electrochemical measurements of the CO_{ad}:H_{upd} ratio yielded a value of ~1.5, confirming that heat treatment could induce the formation of the desired Pt-skin on this nanostructure. The nanoframe electrocatalyst with Pt-skin demonstrated extremely high activity with 36 times increase in mass activity and 22 times in specific activity over Pt/C catalysts.

In order to gain atomic insight into structural factors which contribute to trends in catalytic activity, materials of interest must be studied under reaction conditions (*in situ*). It is generally accepted that a catalyst characterized *ex situ* will not necessarily maintain the same properties under reaction conditions, and for that reason, these systems have been studied *in situ* by techniques such as sum frequency generation,[226] X-ray photoelectron spectroscopy (XPS),[227] and XAS.[62] XAS is an ideal technique for *in situ* studies because it is minimally invasive and the X-rays can penetrate through thin walls typically made of silicon nitride or carbon-based materials in specially designed reactors.[228] The technique can be used to gain information about oxidation states, electronic structure, and chemical ordering of materials among other properties. Recently, XAS has been widely used to study ORR catalysts *in situ* to illustrate the dependence of their catalytic activity on ordering of an alloy,[229] Pt shell thickness,[230] and Pt–Pt bond lengths[231] and to study oxide formation at the Pt-electrolyte interface.[102,232] Here, *ex situ* and, critically, *in situ* X-ray absorption spectroscopy techniques are used to lend more understanding to the nature and success of Pt-skin formation on Pt_3Ni nanoframes which have proven to be one of the best known ORR nanocatalysts to date.

3.3 Pt-Skin Formation on Pt_3Ni/C Catalyst

$PtNi_3$ rhombic dodecahedra were synthesized as previously reported (see Appendix A2).[187] The ideal synthetic result of monodisperse, rhombic dodecahedral nanoparticles with sufficient segregation of the Pt-rich phase to the edges is highly sensitive to certain conditions, including precise temperature of the solvent and incorporation of trace oxygen and water during the hot injection process. In contrast, the evolution to nanoframe is straightforward and can be carried out at a variety of temperatures for different lengths of time. It has been found that the extent of evolution from a dodecahedron to a hollow nanoframe is not critical to the overall performance of the nanocatalyst as excess nickel will always be washed away during electrochemical testing such that the final nanoframe catalyst has the composition Pt_3Ni after electrochemical testing. After the evolution process, the nanoframes were incorporated into the high surface area carbon support and the dry catalyst powder was annealed at 200 °C in air in order to remove the ligands and induce platinum surface segregation to form a Pt-skin structure (Fig. 3.1).[233] Temperatures above approximately 250 °C can cause the nanoframes to sinter, so special care was taken that the temperature never exceeded this limit. After annealing, the Pt_3Ni/C nanocatalyst was mixed with water to form the catalyst ink, and the glassy carbon RDE electrodes were prepared.

The success of Pt-skin structure formation was estimated by electrooxidation of carbon monoxide and underpotentially deposited hydrogen. It has been shown that both H_{upd} and CO_{ad} can be good estimates of platinum surface area by assuming ~210 $\mu C/cm^2$ transferred during a one-electron process (H_{upd}) or ~420 $\mu C/cm^2$ for a two-electron process (CO_{ad}).[163,234] On a Pt-skin surface, the binding to H_{upd} species is weakened such that the surface coverage of adsorbed hydrogen decreases by a factor of approximately one-third. Since CO_{ad} is a much more strongly bound species, its surface coverage on platinum does not change appreciably, making the surface area estimated by CO-stripping the more accurate method for a Pt-skin surface.

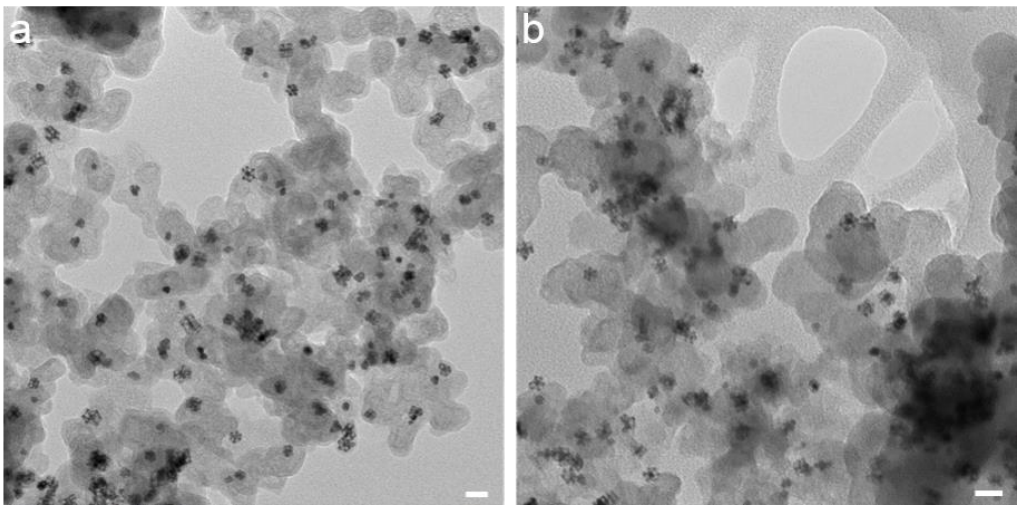


Figure 3.1. TEM images of as-prepared catalyst. (a) $Pt_3Ni(1.0)$ (b) $Pt_3Ni(1.5)$. Scale bars = 25 nm.

As mentioned above, characteristic ratios of CO_{ad}:H_{upd} ECSA have been measured for the Pt-skin surface of single-crystalline $Pt_3Ni(111)$ and the pure Pt(111) surface, yielding values of 1.5 and 1.0, respectively.[165] Pt-skin formation on PtNi nanoparticles has been previously demonstrated by first acid washing to prepare an atomically thin and rough Pt surface, followed by annealing to form a multilayered Pt-skin surface.[163] Similarly, in the case of Pt_3Ni nanoframes, successful platinum nanosegregation to form a Pt-skin is indicated by a CO_{ad}:H_{upd} ratio of 1.5. In contrast, nanoframe samples which demonstrate lower activity typically exhibit a CO_{ad}:H_{upd} ratio close to 1.0. The

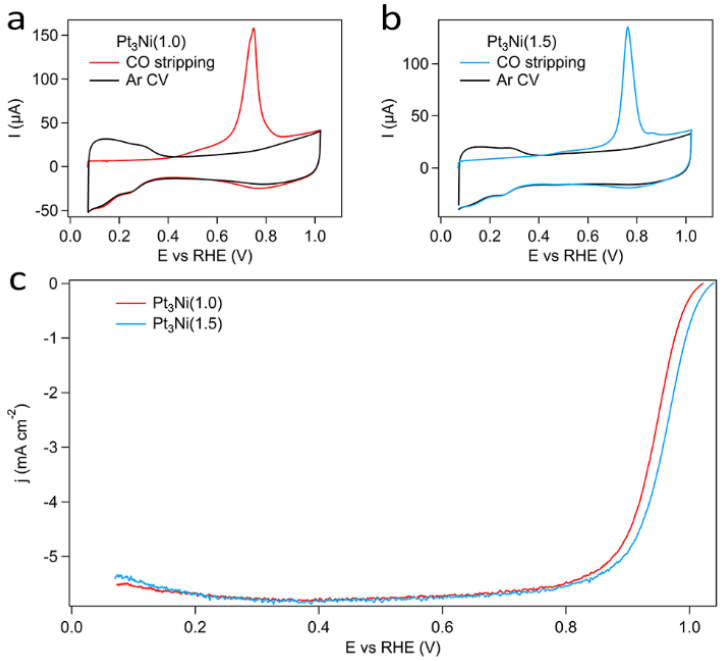


Figure 3.2. Electrochemical characterization of NFs. (a,b) CVs in Ar and electrooxidation of CO_{ad} used to estimate ECSA for different Pt_3Ni nanoframes. Nanoframes with CO_{ad}:H_{upd} ratio equal to 1.0 and 1.5 are referred to as $Pt_3Ni(1.0)$ and $Pt_3Ni(1.5)$, respectively. (c) ORR curves normalized to projected area of the electrode illustrate differences in activity between $Pt_3Ni(1.0)$ and $Pt_3Ni(1.5)$.

nanoframes are always synthesized in the same system, but the catalytic activity of the resulting structure does not always reach the values previously reported for a nanoframe with CO_{ad}:H_{upd} ratio of 1.5.[187] The H_{upd} and CO_{ad} cyclic voltammograms (CV) for Pt_3Ni nanoframes with evidently different types of surface conditions, demonstrated by CO_{ad}:H_{upd} ratios calculated as 1.0 and 1.5, are shown in Fig. 3.2a-b. These electrochemically determined ratios are indicators of the different binding strength between the surface and adsorbates. Fig. 3.2c shows that the CO_{ad}:H_{upd} ratio greatly affects the activity for ORR, with $Pt_3Ni(1.0)$ having a specific activity of 0.75 mA/cm^2 and $Pt_3Ni(1.5)$ having activity of 1.46 mA/cm^2 at 0.95 V vs the reversible hydrogen electrode (RHE). The reported specific activity is based on the CO-stripping measurement. In order to depict the differences in atomic structure of Pt_3Ni nanoframes with ECSA ratios of 1.5 and 1.0, *ex situ* and *in situ* XAS were employed.

3.4 *Ex Situ* XANES and EXAFS Analysis of As-Prepared Pt_3Ni/C

X-ray absorption spectroscopy at the Ni *K*-edge and Pt L_3-edge was carried out at ALS Beamline 10.3.2. The XANES region can provide information on oxidation state based on the edge position and white line intensity. The edge position is typically defined as the peak in the first derivative of the absorption spectrum and becomes more positive for more oxidized species due to differences in the final state energy after photo-ejection of a core electron and generation of the core hole.[235-237] The white line intensity is the main peak in the absorption spectrum just after the edge. It increases in intensity for an oxidized species because of the larger probability for an X-ray absorption event to occur due to the increased availability of electronic states.[238,239] As can be seen from Fig. 3.3a, after

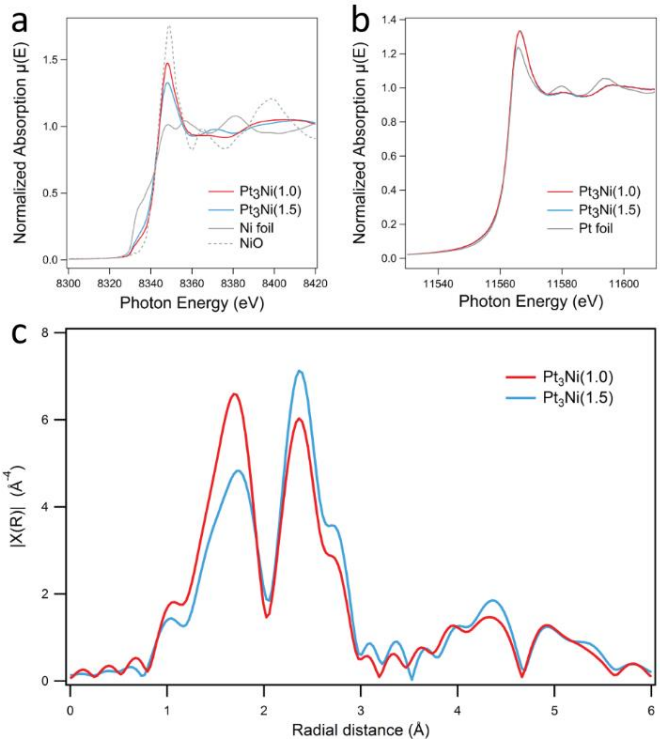


Figure 3.3. X-ray absorption spectroscopy of Pt_3Ni/C catalysts before electrochemistry. (a) Ni *K*-edge XANES compared to Ni foil and NiO powder standards. (b) Pt L_3-edge XANES compared to Pt foil standard. (c) Ni *K*-edge EXAFS spectra.

annealing of the catalyst in air, the nickel is in a more oxidized state relative to nickel metal. The extent of nickel oxidation is indicated by a positive increase of the absorption edge position in the range of 8331–8337 eV and an increase in the white line intensity at ~8348 eV. The level of nickel oxidation for both the $Pt_3Ni(1.0)$ and $Pt_3Ni(1.5)$ samples is between Ni^0 and Ni^{2+} when compared to XANES spectra of Ni foil and NiO standards. This demonstrates the co-existence of two nickel species: one in a surface nickel oxide that remains after the evolution and annealing processes and one in the Pt_3Ni alloy. According to previous literature on surface segregation in PtNi octahedra, nickel will segregate to the surface as an oxidized species after annealing at 200 °C in 1 bar O_2.[240] In the Pt_3Ni nanoframe system, nickel at or near the surface of the nanoframe after evolution from solid particle to nanoframe will be oxidized during annealing at 200 °C in air, while nickel in the bulk alloy will remain alloyed. The result is small oxidized clusters of nickel on the surface of the nanoframe which can be removed during electrochemical treatment. The nickel in $Pt_3Ni(1.0)$ is more oxidized than in $Pt_3Ni(1.5)$, indicating that a larger quantity of surface NiO clusters remain in the $Pt_3Ni(1.0)$ nanoframe after evolution and annealing. This confirms that after the evolution process, there was more nickel present at the surface of the nanoframe in $Pt_3Ni(1.0)$ relative to $Pt_3Ni(1.5)$. It is important to note that synchrotron-based XRD, which takes advantage of high photon flux and high energy, short wavelength X-rays, could not detect crystalline nickel oxide in the Pt_3Ni nanoframes (Fig. 3.4), indicating that the oxidized nickel species exist as very small domains of low crystallinity. The Pt L_3-edge XANES (Fig. 3.3b) indicates that the platinum in $Pt_3Ni(1.0)$ and $Pt_3Ni(1.5)$ has a similar oxidation state which is slightly more oxidized than bulk Pt in a Pt foil standard.

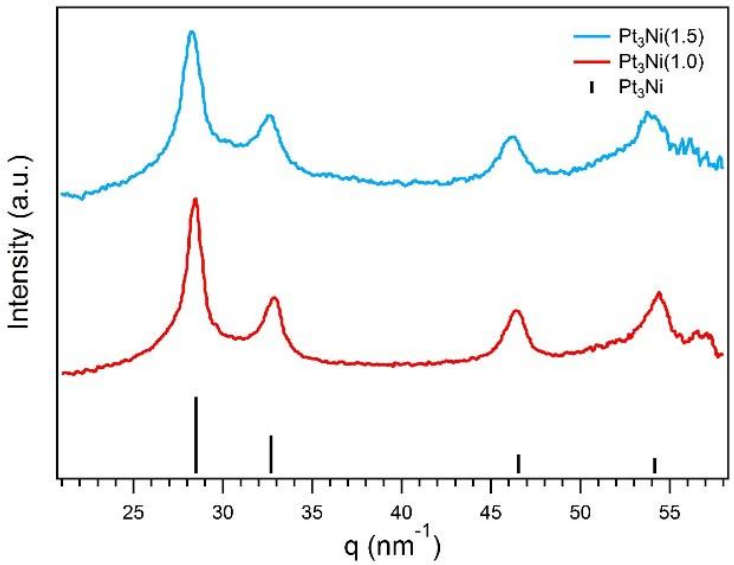


Figure 3.4. XRD of NFs. X-ray diffraction patterns of $Pt_3Ni(1.0)$ and $Pt_3Ni(1.5)$ as-prepared after annealing on carbon support.

While XANES provides information on oxidation state, EXAFS is utilized to acquire structural parameters such as coordination numbers, bond lengths, and the extent of alloying in a bimetallic nanoparticle.[241] In the post-edge region, the X-ray photon absorption creates a photoelectron wave which propagates outward from the absorbing atom. This wave can be scattered off of neighboring atoms, causing interference between the outward propagating wave and the backscattered wave. This

interference can be constructive or destructive and causes the fine structure in an X-ray absorption spectrum by modulating the absorption coefficient. Because the scattering of the photoelectron wave is dependent on the distance between atoms and the identity of those atoms, coordination information can be extracted from EXAFS data. EXAFS data at the Ni *K*-edge and Pt L_3-edge were co-refined in order to analyze the atomic structure of Pt_3Ni(1.0) and Pt_3Ni(1.5). After annealing of the catalyst and before electrochemistry, further proof of the surface nickel oxide can be seen in the Ni *K*-edge *R*-space EXAFS spectra in which there is a first coordination shell at ~1.7 Å indicative of Ni–O scattering (Fig. 3.3c). The EXAFS spectra in Fig. 3.5 were fit to a combination of a disordered fcc platinum nickel alloy model and a nickel oxide model. Due to the small nature of the nickel oxide species, only

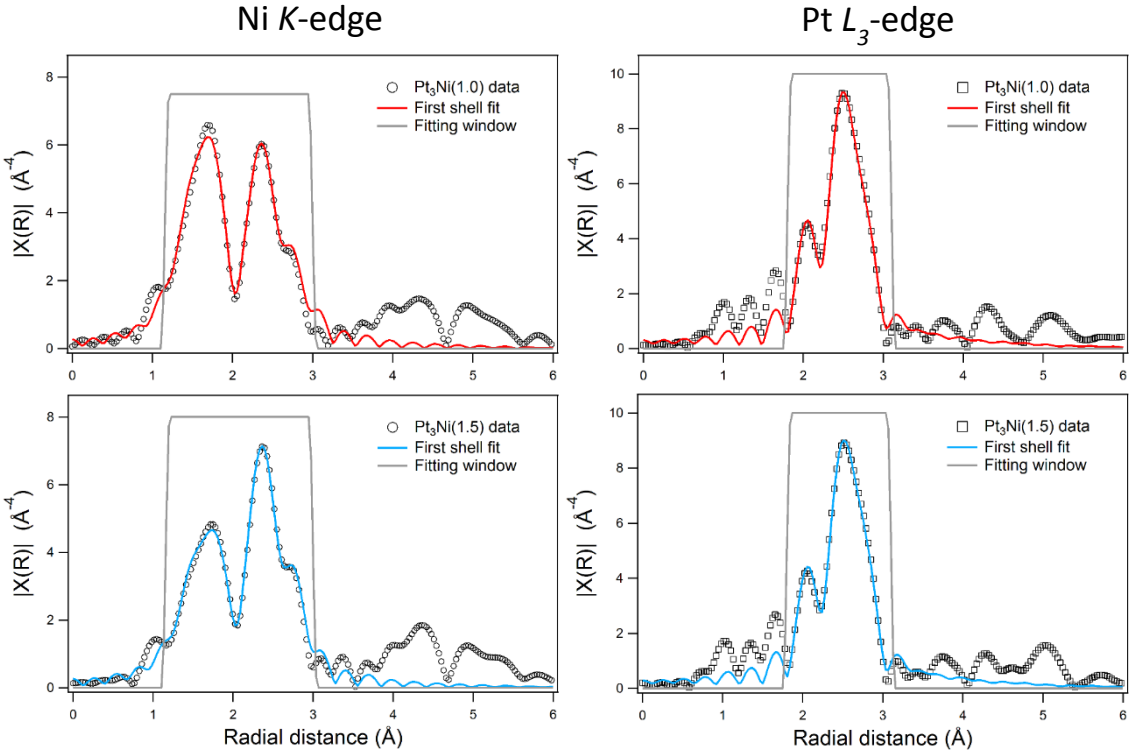


Figure 3.5. EXAFS of as-prepared catalysts. EXAFS fitting of first coordination shell for Ni *K*-edge and Pt L_3-edge data (after annealing and before electrochemistry). For Ni *K*-edge EXAFS, Δk = 2-13 Å^{-1} and ΔR = 1.2-3 Å. For Pt L_3-edge EXAFS, Δk = 2-14 Å^{-1} and ΔR = 1.8-3.1 Å.

a first-shell Ni–O scattering path was included in modeling the nickel oxide species because any further Ni–Ni or Ni–O scattering paths were not significant. The nickel–oxygen coordination number derived from the fit, shown in Table 3.1, supports the conclusion that the Pt_3Ni(1.0) nanoframe has a higher concentration of surface NiO clusters than Pt_3Ni(1.5). The fit also shows that platinum is already segregated to the surface in the Pt_3Ni(1.5) evidenced by the lower total coordination number for platinum than nickel. Surface atoms have fewer neighbors, reducing their average coordination number measured by EXAFS modeling.[242] In Pt_3Ni(1.0), nickel is still slightly enriched at the surface of the frames, supporting the observation of greater nickel oxide formation on these nanoframes. In summary, after annealing treatment, both nanoframe samples exhibit formation of oxidized nickel clusters at their surfaces. This allows for Pt-enrichment beneath the clusters, as demonstrated in the as-prepared EXAFS of Pt_3Ni(1.5).

Table 3.1. EXAFS fitting parameters of as-prepared nanoframe catalysts.[a]

	$Pt_3Ni(1.0)$	$Pt_3Ni(1.5)$
N_{PtNi}	4.4 (1.7)	3.1 (1.3)
N_{NiPt}	7.9 (1.5)	7.9 (1.4)
N_{PtPt}	4.7 (1.5)	5.0 (1.3)
N_{NiNi}	0.7 (0.4)	1.0 (0.6)
N_{Pt}	9.1 (3.2)	8.1 (2.6)
N_{Ni}	8.6 (1.9)	8.9 (2.0)
R_{PtNi}	2.661 (0.023)	2.664 (0.019)
R_{PtPt}	2.710 (0.010)	2.72 (0.010)
R_{NiNi}	2.637 (0.015)	2.646 (0.015)
N_{NiO}	4.8 (0.5)	3.4 (0.5)
R_{NiO}	2.050 (0.008)	2.051 (0.010)

[a]Values in parentheses are error bars determined from IFEFFIT.

3.5 *In Situ* XANES and EXAFS Analysis of Pt_3Ni/C

Before probing the catalyst *in situ*, the electrode was electrochemically annealed with a cycling process which is standard procedure in an RDE set up to allow the catalyst to reach a steady-state composition and surface structure. The catalyst film on carbon paper for XAS was prepared with similar thickness to an RDE catalyst film so that all metal sites were considered electrochemically accessible (see Appendix A2.5). After cycling of the electrode, XANES spectra were collected at the Ni *K*-edge and Pt L_3-edge at 0.9 V vs RHE under oxygen to replicate ORR conditions. First, it is evident in Fig. 3.6a through the decrease in white line intensity that the surface NiO has dissolved in the acidic electrolyte after potential cycling, giving the Ni XANES spectrum more metallic character. It was also found that at both metal edges, the XANES spectra were identical, and therefore, the oxidation states of both metals in both samples were deemed identical (Fig. 3.6a-b). The near-edge region of X-ray absorption probes electronic transitions from a core level into local, unoccupied states just above the Fermi level energy. During *in situ* ORR, the Fermi levels of the Pt_3Ni metallic samples are controlled by the potentiostat at an identical potential relative to a reference electrode potential.[40] Therefore, the probability of an X-ray absorption-induced transition into the unoccupied states is similar for these samples while under potential control, and their XANES spectra are identical. However, as can be seen from Fig. 3.6c-d, after the electrode is removed from the electrolyte, rinsed, and dried, the XANES spectra are no longer identical between $Pt_3Ni(1.0)$ and $Pt_3Ni(1.5)$. The Ni in $Pt_3Ni(1.0)$ is more oxidized while the Pt is more reduced, indicating increased donation of electron density from Ni to Pt in $Pt_3Ni(1.0)$.[243] The increased alloying in $Pt_3Ni(1.0)$ will be further supported by the EXAFS analysis discussed below. Fig. 3.6e shows a XANES difference spectrum at the Ni *K*-edge for $Pt_3Ni(1.0)$ and $Pt_3Ni(1.5)$ samples where the normalized absorption *in situ* is subtracted from the normalized absorption after ORR. After the catalyst is rinsed and dried under nitrogen, the nickel in $Pt_3Ni(1.0)$ is more easily oxidized as indicated by the more intense peak at the white line position,

approximately 16–17 eV after the edge. The platinum shell is not protecting the nickel as thoroughly in $Pt_3Ni(1.0)$, suggesting the surface has more low coordination sites and a thinner platinum shell, as illustrated in Fig. 3.6f. These conclusions will be further substantiated by EXAFS data.

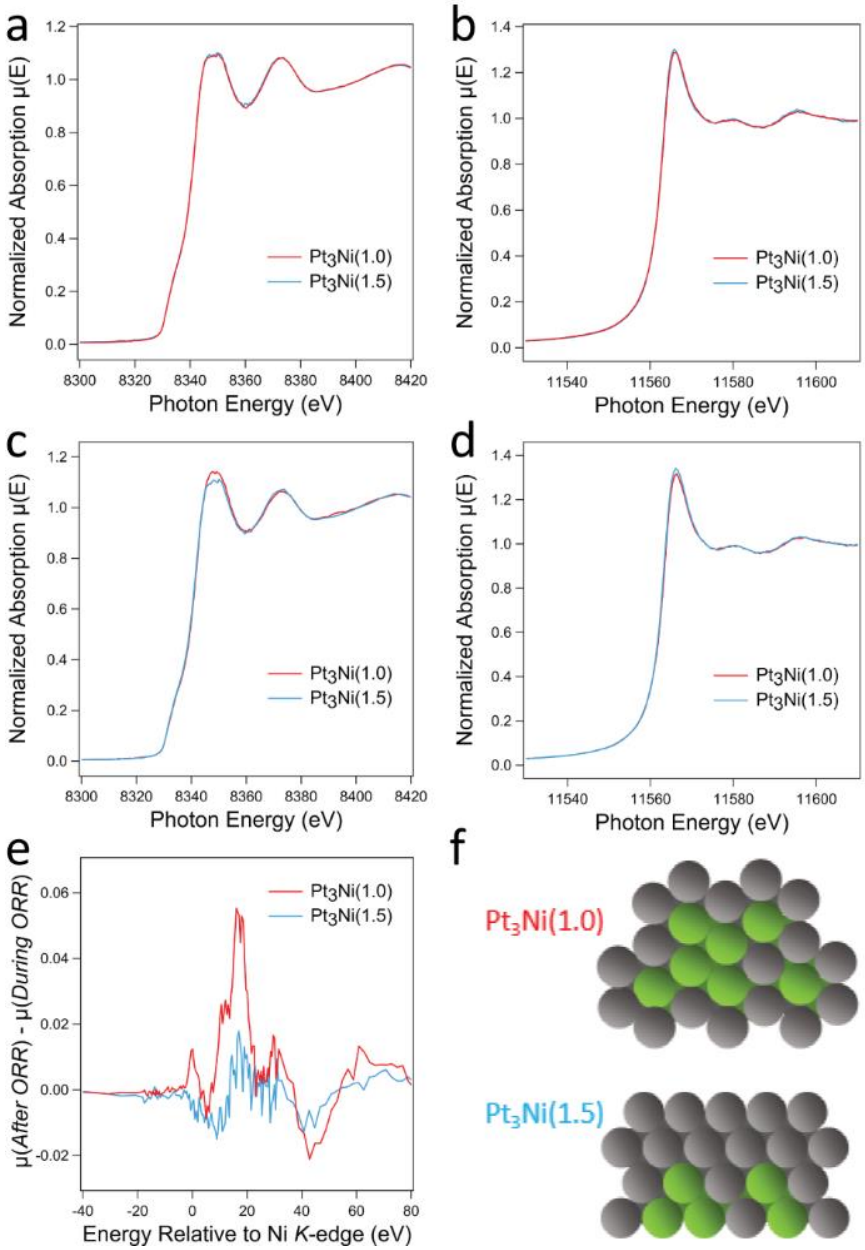


Figure 3.6. XANES of Pt_3Ni/C catalysts *in situ* and after electrochemistry. (a) Ni *K*-edge at 0.9 V. (b) Pt L_3-edge at 0.9 V. (c) Ni *K*-edge after *in situ*. (d) Pt L_3-edge after *in situ*. (e) Ni *K*-edge *in situ* XANES subtracted from after *in situ* XANES. (f) Model surfaces of $Pt_3Ni(1.0)$ and $Pt_3Ni(1.5)$, where gray atoms are Pt and green atoms are Ni.

In situ EXAFS analysis yields a clear picture of the differences in atomic distribution and structuring in $Pt_3Ni(1.0)$ and $Pt_3Ni(1.5)$. As stated earlier, the working electrode was cycled in order to condition the catalyst and then held at 0.9 V vs RHE for *in situ* ORR. The Fourier transformed EXAFS spectra

are shown in Fig. 3.7. EXAFS data for Pt and Ni foils were taken in order to execute a fit on the bulk sample and determine the S_0^2 parameter, which was then used during fitting of the nanoframe EXAFS spectra. A fit to the first shell was performed using identical bounds in *R*-space for $Pt_3Ni(1.0)$ and $Pt_3Ni(1.5)$. A disordered fcc Pt_3Ni model was created in order to generate the first shell homo- and heterometallic scattering paths. Coordination numbers, path lengths, and mean-square disorder

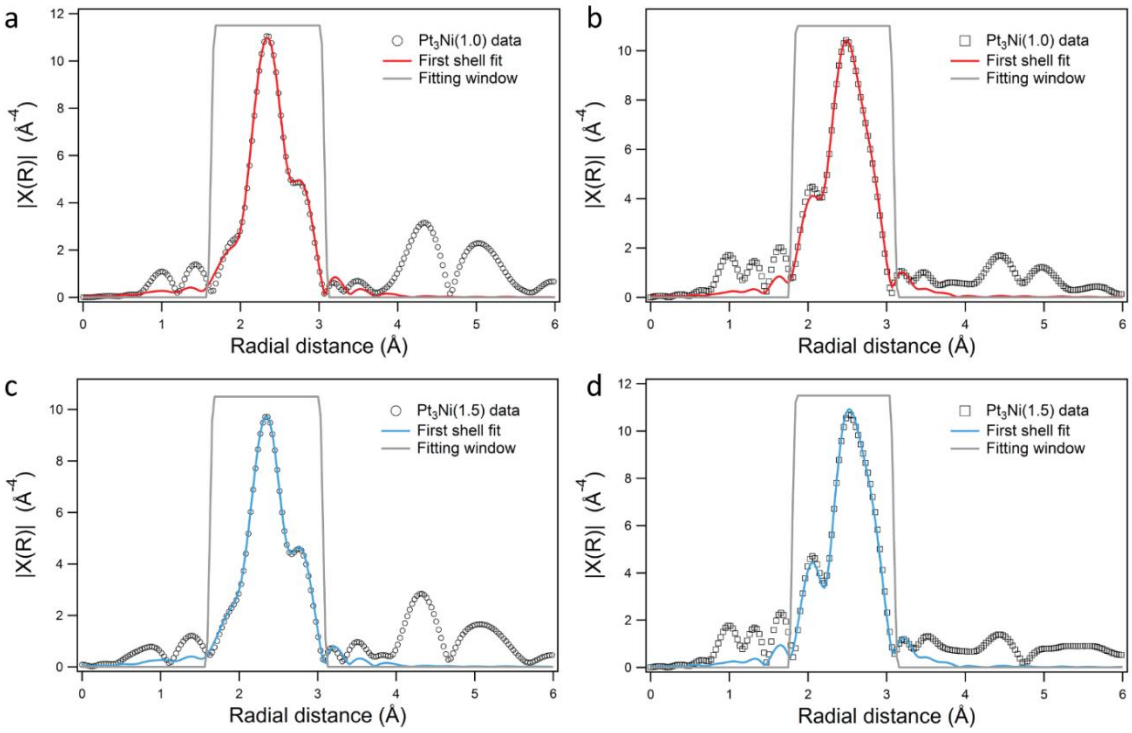


Figure 3.7. EXAFS of catalysts *in situ*. Fits to the first coordination shell: (a) Ni *K*-edge EXAFS of $Pt_3Ni(1.0)$. (b) Pt L_3-edge EXAFS of $Pt_3Ni(1.0)$. (c) Ni *K*-edge EXAFS of $Pt_3Ni(1.5)$. (d) Pt L_3-edge EXAFS of $Pt_3Ni(1.5)$. For Pt EXAFS, Δk = 2.0–13.5 Å^{-1} and ΔR = 1.8–3.1 Å. For Ni EXAFS, Δk = 2.0–12.0 Å^{-1} and ΔR = 1.6–3.1 Å.

parameters were allowed to float with the restraints that $R_{PtNi} = R_{NiPt}$ and $\sigma_{PtNi}^2 = \sigma_{NiPt}^2$. The identical fitting procedure was used for all first shell fits, and the fitted parameters are shown in Table 3.2. Extended shell fitting was unsuccessful due to the disordered nature of the alloy and the small dimension of a single nanoframe edge, which is approximately 2 nm in width, leading to a reduced amplitude of the outer shells. The initial observation in the first shell fit is that the total coordination numbers N_{Pt} and N_{Ni} are similar for both samples, with N_{Pt} significantly smaller than N_{Ni}. As mentioned previously, this indicates that Pt atoms have segregated to the surface to form some variation of the desired Pt-skin structure because of the lower coordination number of surface atoms. It can also be seen that the heterometallic coordination of nickel to platinum is decreased in $Pt_3Ni(1.5)$, and correspondingly the homometallic coordination is increased. This depicts the nanoframe of $Pt_3Ni(1.5)$ as one with more segregation of Pt from Ni, which is also indicated by the smaller extent of alloying parameters for platinum, J_{Pt}, calculated for $Pt_3Ni(1.5)$ versus $Pt_3Ni(1.0)$. The extent of alloying parameters are calculated using the coordination numbers determined from EXAFS according to the method developed by Hwang et al.[244]

Table 3.2. EXAFS fitting parameters of nanoframe catalysts during *in situ* ORR.[a]

	Pt_3Ni(1.0)	**Pt_3Ni(1.5)**
N_{PtNi}	2.5 (0.5)	1.8 (0.5)
N_{NiPt}	6.4 (0.9)	6.4 (1.1)
N_{PtPt}	6.0 (0.7)	6.9 (0.8)
N_{NiNi}	3.9 (0.7)	4.0 (1.0)
N_{Pt}	8.5 (1.2)	8.7 (1.3)
N_{Ni}	10.3 (1.6)	10.4 (2.1)
R_{PtNi}	2.657 (0.006)	2.666 (0.007)
R_{PtPt}	2.716 (0.004)	2.728 (0.004)
R_{NiNi}	2.648 (0.007)	2.655 (0.010)
J_{Pt} (%)	117	82
J_{Ni} (%)	83	82

[a]Values in parentheses are error bars determined from IFEFFIT.

The composition of the nanoframe can be determined by Eq. 3.1[245]

$$\frac{X_{Pt}}{X_{Ni}} = \frac{N_{NiPt}}{N_{PtNi}} \tag{3.1}$$

The sensitivity of the EXAFS measurement allows for estimation of slight variations in composition of Pt_3Ni(1.0) and Pt_3Ni(1.5) from the nominal value of the thermodynamically favorable, ordered Pt_3Ni state. It was determined from *in situ* EXAFS measurements that Pt_3Ni(1.0) was 28% nickel while Pt_3Ni(1.5) was 22% nickel. It is expected that the composition will not be exactly that of Pt_3Ni because the final composition of the nanoframe must be influenced by the amount of platinum segregation to the edge of the initial dodecahedra that were synthesized. The spontaneous corrosion to the nanoframe is a kinetically controlled process that does not access the thermodynamically stable, ordered Pt_3Ni phase, given the disordered structure of the initial bimetallic particle. A nickel-rich nanoframe in the case of Pt_3Ni(1.0) is further supported by the shorter bond lengths which were measured by EXAFS modeling. Due to a slightly larger incorporation of the smaller element, nickel, the bond lengths in Pt_3Ni(1.0) are shorter.

The *ex situ* post-ORR EXAFS data were collected after the catalyst film was rinsed with ultrapure water and dried under N_2 (Fig. 3.8). It must be emphasized that the EXAFS analysis showed the same trends in coordination numbers, bond lengths, extent of alloying, and alloy composition between Pt_3Ni(1.0) and Pt_3Ni(1.5) after ORR as the *in situ* measurement, indicating good reproducibility of the technique (Table 3.3).

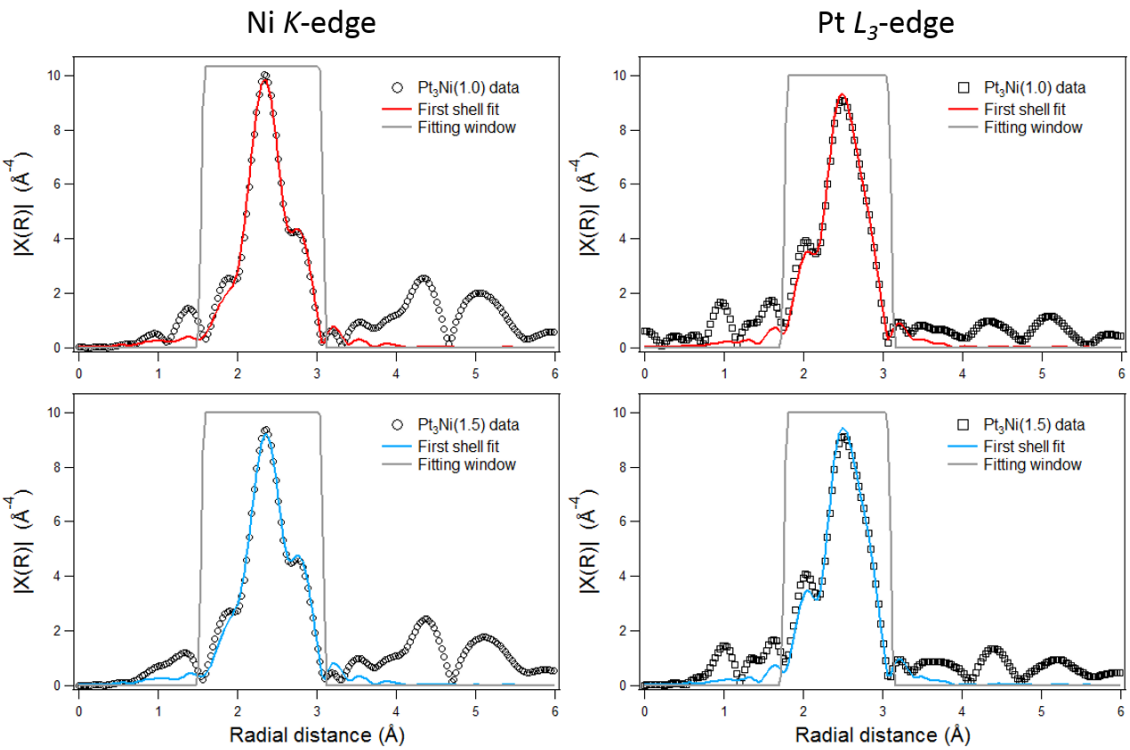


Figure 3.8. EXAFS of catalysts after electrochemistry. Fitting of first coordination shell for Ni *K*-edge and Pt L_3-edge data of the nanoframe catalyst after electrochemistry (rinsed with deionized water and dried under N_2). For Ni *K*-edge EXAFS, Δk = 2-12 Å^{-1} and ΔR = 1.5-3.1 Å. For Pt L_3-edge EXAFS, Δk = 2-13.5 Å^{-1} and ΔR = 1.8-3.1 Å.

Table 3.3. EXAFS fitting parameters of catalysts after electrochemistry.[a]

	Pt_3Ni(1.0)	**Pt_3Ni(1.5)**
N_{PtNi}	2.1 (0.7)	1.6 (0.7)
N_{NiPt}	5.7 (1.0)	5.5 (1.3)
N_{PtPt}	5.6 (1.0)	6.3 (1.2)
N_{NiNi}	4.1 (1.0)	4.4 (1.2)
N_{Pt}	7.7 (1.7)	7.9 (1.9)
N_{Ni}	9.8 (2.0)	9.9 (2.5)
R_{PtNi}	2.66 (0.008)	2.671 (0.007)
R_{PtPt}	2.715 (0.008)	2.725 (0.010)
R_{NiNi}	2.651 (0.009)	2.659 (0.010)
J_{Pt} (%)	109	79
J_{Ni} (%)	77	74

[a]Values in parentheses are error bars determined from IFEFFIT.

3.6 Model of *Ex Situ* and *In Situ* Pt_3Ni/C Surfaces

The information gathered from *ex situ* and *in situ* XANES and EXAFS measurements on Pt_3Ni nanoframe ORR catalysts provides an understanding of the structure of the more active $Pt_3Ni(1.5)$ catalysts. After evolution from nanopolyhedra to nanoframes, the nanoframes have platinum and nickel present at their surfaces, with $Pt_3Ni(1.5)$ slightly enriched in platinum at its surface. The annealing process in air atmosphere induces the formation of surface nickel oxide clusters while allowing for Pt enrichment beneath the nickel oxide clusters in $Pt_3Ni(1.5)$. $Pt_3Ni(1.5)$ has fewer nickel oxide clusters due to a larger presence of platinum on the surface of the nanoframe. The larger concentration of platinum on the surface of the $Pt_3Ni(1.5)$ nanoframe after the evolution process is attributed to better segregation of platinum to the edges of the initially synthesized rhombic dodecahedron. Anisotropic elemental distribution and phase segregation within a bimetallic nanocrystal have been previously observed in Pt–Ni octahedra as well,[155] and play a key role in the successful spontaneous corrosion of a solid rhombic dodecahedron into a $Pt_3Ni(1.5)$ nanoframe. The complete formation of the Pt-rich framework at the edges of the initial solid polyhedron makes it easier to extract nickel from the interior of the polyhedron during the spontaneous corrosion to a hollow nanoframe. Fig. 3.9a-b illustrates the differences between the surface and alloying conditions of a cross-section of an edge of the $Pt_3Ni(1.0)$ and $Pt_3Ni(1.5)$ nanoframe before electrochemistry. The

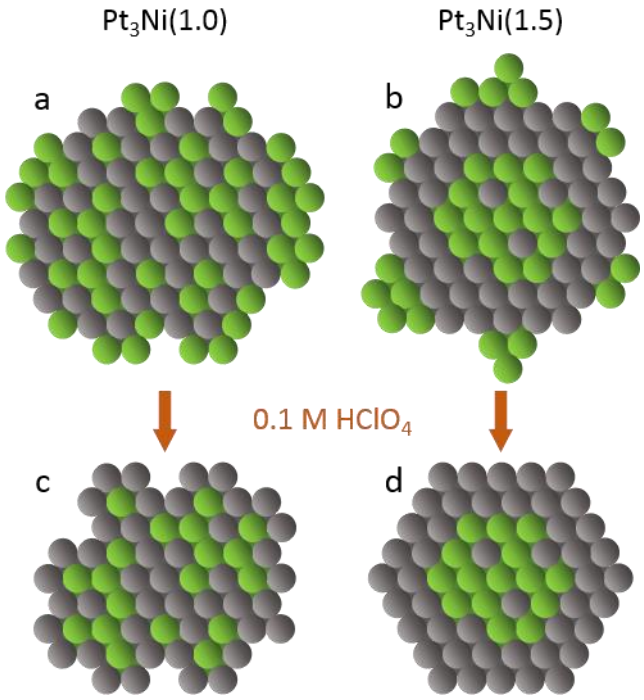


Figure 3.9. Nanoframe atomic structure models. Models of the atomic level structure of the edge of the $Pt_3Ni(1.0)$ and $Pt_3Ni(1.5)$ nanoframes (shown in cross-section) before electrochemistry (a,b) and *in situ* during ORR catalysis (c,d). Gray atoms are Pt and green atoms are Ni.

nickel atoms at the surface are representative of nickel oxide clusters which form after annealing in air. Once the nanoframe samples are immersed in the electrolyte, 0.1 M $HClO_4$, and electrochemically annealed, the nickel oxide is dissolved from the surface, leaving pure platinum. *In situ* EXAFS analysis

reveals more significant segregation of Pt from Ni in $Pt_3Ni(1.5)$ and slightly nickel-rich composition of $Pt_3Ni(1.0)$. The alloying data extracted from the EXAFS analysis of $Pt_3Ni(1.0)$ and $Pt_3Ni(1.5)$ once removed from electrolyte, rinsed, and dried, reflected identical differences as during *in situ* measurements. However, it was observed that nickel in the $Pt_3Ni(1.0)$ nanoframe was slightly more oxidized compared to that in the $Pt_3Ni(1.5)$ after exposure to air, which is further evidence that nickel is present closer to the surface, covered by a thinner, lower-coordinated platinum shell. The conclusions made from this analysis before, during, and after ORR electrochemical measurements lead to the model shown in Fig. 3.9c-d for the *in situ* atomic structuring of the edge of a nanoframe. The ideal nanoframe catalyst represented by $Pt_3Ni(1.5)$ forms a more uniform Pt-skin due to its increased segregation of platinum from nickel and slightly platinum-rich composition. The ability to form the ideal Pt-skin on the nanoframe is primarily predetermined by the initial synthesis of the rhombic dodecahedra and the amount of platinum segregation to the edges which is achieved. The extent of evolution toward the nanoframe, accelerated by solution-phase heating in the presence of oxygen, and the annealing step, are less critical to the formation of the ideal surface condition. If the segregation of platinum to the edges of the rhombic dodecahedron is not sufficient, the final nanoframe is likely to be enriched in nickel and have excessive nickel present at the surface of the nanoframe during annealing, preventing successful Pt-skin formation and causing a rough platinum surface to be exposed during electrochemistry. As has been observed on PtNi nanoparticles, the rough platinum surface exhibits a CO_{ad}:H_{upd} ratio of 1.0.[163] This decreased ratio compared to the $Pt_3Ni(1.5)$ is driven by adsorbates being more strongly bound due to the higher concentration of low coordination surface sites on the rougher platinum surface of the $Pt_3Ni(1.0)$. If the rhombic dodecahedron is synthesized with the desirable segregation of platinum to its edges, the nickel can be more thoroughly removed from the interior of the nanoframe and the nanoframe will form the desired Pt-skin during annealing. This ideal surface segregation of platinum changes the surface *d*-band electronic structure such that adsorbates are bound more weakly, simultaneously leading to the CO_{ad}:H_{upd} ratio of 1.5 and dramatically increased activity for the ORR.

3.7 Conclusions

In summary, surface-sensitive electrochemical techniques and *ex situ* and *in situ* XAS were used to identify differences in atomic-level structure of Pt_3Ni nanoframe catalysts which led to differences in their ORR activity. ECSA estimated from voltammograms of adsorbed H_{upd} and CO_{ad} were used to identify nanoframes with CO_{ad}:H_{upd} surface area ratios of 1.0 and 1.5. The ratio of 1.0 indicates the surface of the nanoframe that correlates with lesser activity for the ORR. In addition, the as-prepared $Pt_3Ni(1.0)$ demonstrated more abundant surface nickel oxide formation as compared to $Pt_3Ni(1.5)$. This nickel oxide was dissolved from the surface via electrochemical cycling in the acidic electrolyte, leaving behind a platinum surface. *In situ* EXAFS demonstrated that $Pt_3Ni(1.0)$ had a larger extent of alloying while $Pt_3Ni(1.5)$ had more significant segregation of Pt to the surface of the nanoframe. It was concluded that $Pt_3Ni(1.0)$ has a thinner, rougher Pt surface caused by insufficient segregation of Pt to the surface. $Pt_3Ni(1.5)$ exhibits extremely high ORR activity due to its significant segregation of Pt from Ni, allowing for better formation of a Pt-skin. The activity of a given nanoframe sample was resolved to be primarily pre-determined by the level of platinum enrichment at the edges of the initial rhombic dodecahedron.

4. Mechanism of Pt-Ni Rhombic Dodecahedron Growth

Portions of the content and figures of this chapter are reprinted or adapted with permission from Z. Niu†, N. Becknell†, Y. Yu, D. Kim, C. Chen, N. Kornienko, G. A. Somorjai, P. Yang, "Anisotropic phase segregation and migration of Pt in nanocrystals en route to nanoframe catalysts", Nat. Mater., 2016, 15, 1188. DOI: 10.1038/nmat4724. Copyright 2016 Macmillan Publishers Ltd: Nature Materials.

4.1 Preface

The discovery of Pt_3Ni nanoframes was somewhat fortuitous, and therefore the synthetic mechanism enabling this complex structure was not well understood. In order to take advantage of all of this system's capabilities, the mechanisms behind the formation of Pt-Ni rhombic dodecahedra required deeper exploration. In Chapter 4, quasi-*in situ* sampling of the rhombic dodecahedron synthesis was coupled with a complete set of materials characterization techniques to elucidate the multiple mechanistic steps that facilitate the synthesis of Pt-Ni rhombic dodecahedra with specific phase segregation patterns.

4.2 Introduction

Metal nanocatalysts are an important sector of heterogeneous catalysis because their high surface-to-mass ratio allows for efficient use of expensive, catalytically active transition metals.[193] Discovery of novel nanocatalysts is vital in increasing catalytic efficiency to conserve energy and precious metals in various processes.[23] Two strategies heavily utilized in the discovery of novel nanocatalysts are composition[246] and shape[247,248] control. These approaches, in particular, have been central to the advancement of oxygen reduction electrocatalysis. Platinum alloys have shown dramatic improvement over pure platinum,[82,83,163] and platinum–nickel octahedra have consistently demonstrated activity improvements over their spherical counterparts.[149,150,152-154,225] However, new strategies are needed to push the activity and stability of platinum-based nanocatalysts to more impressive numbers which can make an impact in the fuel cell market.[22,23]

One strategy coming to the forefront of catalyst innovation is nanoscopic design of bimetallic catalyst structures through spatial segregation of the elements. Element-specific segregation in the Pt–Ni alloy system has been an intensively studied topic due to the early observation of a Pt-enriched {111} surface after vacuum annealing and its use as an extraordinary model oxygen reduction electrocatalyst.[82,89] Naturally, Pt–Ni octahedral nanocatalysts were synthesized to attempt to replicate the unique nanosegregation of Pt to the {111} facets, but it was observed that {111} facets were Ni-rich, and therefore corroded from the octahedra during electrochemical testing.[154] Recently, an in-depth study by Gan et al. explained that, during Pt–Ni octahedra synthesis, platinum was reduced first

into hexapod-like concave nanocrystals on which nickel would undergo step-induced growth into the concave surfaces of the hexapod, forming the Ni-rich facets.[155] Oh et al. observed similar hexapod-like Pt-rich arms in their Pt–Ni octahedral system, but in the presence of carbon monoxide some Pt then migrated to the edges of the octahedron, creating a structure similar to a nanoframe.[189]

Yang et al. observed similar phenomena during the synthesis of $PtNi_3$ and $PtCo_3$ rhombic dodecahedra, which had a Pt-rich phase segregated to their edges.[187,249,250] Until now, it was not understood how the Pt-rich phase segregated to the edges of the rhombic dodecahedron and what was the driving force for this phenomenon. However, in this work, the formation mechanism of Pt-Ni rhombic dodecahedra has been fully described by analyzing the reaction at a slower rate with quasi-*in situ* sampling. The growth is divided into distinct stages of Pt-rich phase segregation and subsequent phase migration. It is found that initially, a Pt-rich seed particle forms on which overgrowth occurs in both the <111> and <200> growth directions. This distinctive bidirectional growth and segregation of the Pt-rich phase structurally guides the formation of the dodecahedron and provides a pathway for Pt atoms to migrate outwards to the vertices and edges of the dodecahedron and become enriched on the edges. By stopping the nanoparticle growth at specific times, the segregation of Pt to the edges of the rhombic dodecahedron can be controlled, and is shown to dictate the oxygen reduction activity of the nanoframes which result from the corrosion of the rhombic dodecahedra.

4.3 Pre-Rhombic Dodecahedron Observations

The Pt–Ni rhombic dodecahedra (RD) were synthesized by hot-injection of metal precursors in oleylamine at a lower synthetic temperature than reported in Chapter 3 (265 °C)[249] to track the growth process over a longer period of time (see Appendix A3). Intermediate structures were captured from

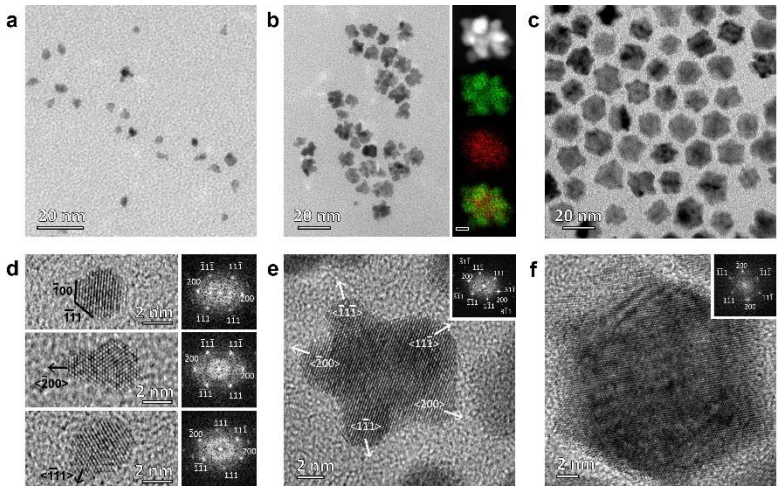


Figure 4.1. Formation process of the rhombic dodecahedra. TEM (a–c) and corresponding HRTEM (d–f) images of interim products obtained from the growth solution when its color is green, yellow, and brown, respectively. HAADF-STEM and EDS elemental mapping images (b, right) of a typical particle in (b): green is Pt and red is Ni, scale bar, 2 nm. FFTs of the corresponding HRTEM images (d, right; insets in e and f) indicate the growth directions of elongated nanoparticles and branched nanostructures. Moiré patterns (f) indicate the superimposition of two phases with different lattice constants present in the particle.[251]

the growth solution, which turned from green to yellow, brown, and finally black in about one hour. The initial Pt–Ni nanoparticles (Fig. 4.1a) collected from the green growth solution had an average size of 3.3 ± 1.4 nm and a composition of $Pt_{70}Ni_{30}$, as determined by EDS. Their morphology is either near-spherical (dominated by {111} and {100} facets) or elongated in the <111> or <200> directions as shown in the HRTEM images (Fig. 4.1d). When the solution turned yellow, these small nanoparticles had grown into branched structures with a size range of 4–15 nm (Fig. 4.1b). The growth directions of the short arms are <111> and <200> (Fig. 4.1e and Fig. 4.2), identical to those of the initial non-spherical particles. This indicates that the initial small particles serve as seeds on which bidirectional overgrowth occurs along the <111> and <200> directions much faster than other directions.[252] The HAADF-STEM and EDS mapping images of a typical branched particle

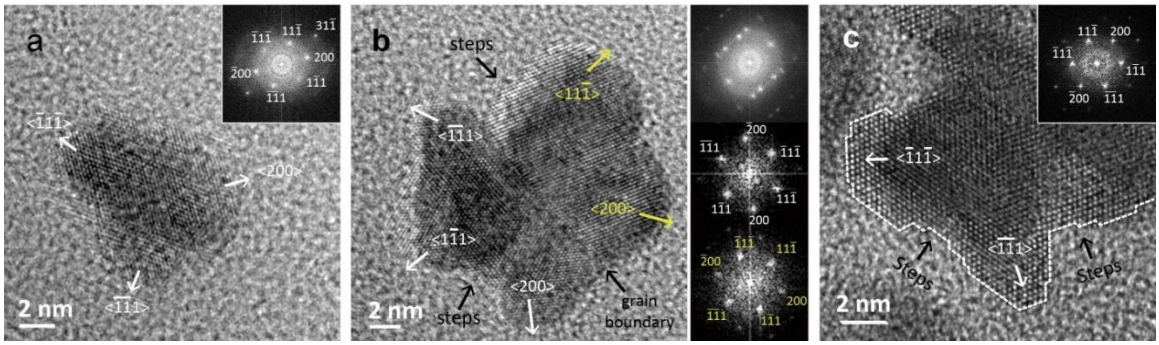


Figure 4.2. HRTEM images of interim ill-defined branches. The growth directions of the short arms in these branch structures, collected when the growth solution is yellow, are identified as <111> and <200>, regardless of the particle sizes. Insets in (a) and (c), as well as the right panel of (b) show the corresponding FFTs. Most branch particles are single crystals, while some have grain boundaries as shown in (b). Step sites are observed at the bottom of the short arms as indicated by black arrows in (b) and (c).

demonstrate that Pt is homogeneously distributed within the whole particle, whereas Ni is mainly distributed around the centre (Fig. 4.1b, right). The composition of these branched structures was $Pt_{49}Ni_{51}$. The higher Ni content compared to the initial nanoparticles suggests the reduction of Ni is accelerated during this period, possibly induced by step sites between the arms of the growing branched structures, as indicated in Fig. 4.2c.[155,156] These step sites are located precisely where the growth of the Ni-rich phase is observed in EDS mapping. When the growth solution became brown, most branched particles had grown into well-defined polyhedra with an average size of 13 ± 5 nm (Fig. 4.1c, f). The polyhedra have been identified as rhombic dodecahedra on the basis of typical projections along different zone axes.[187] The Ni content increased significantly to $Pt_{12}Ni_{88}$, which could result from continuous Ni-rich phase deposition on step sites until reaching the top of the arms and filling out the rhombic dodecahedron.

4.4 Rhombic Dodecahedron Progression and Corrosion to 3-D Nanostructures

Fig. 4.3a–c shows TEM images of products obtained at 3, 10 and 30 min after the growth solution had turned black. They are denoted as RD-3, RD-10 and RD-30, respectively. The average size is

similar for RD-3 (16 nm, standard deviation σ = 1.6) and RD-10 (17 nm, σ = 2.1), but increases for RD-30 (22 nm, σ = 2.6) (Fig. 4.4a). To expose the distribution of the Pt-rich phase in the particles, the Ni-rich phase was selectively removed by chemical corrosion and these structures were termed RD-3-cor, RD-10-cor and RD-30-cor, respectively. RD-3 evolved to structures (Fig. 4.3d and Fig. 4.5) that

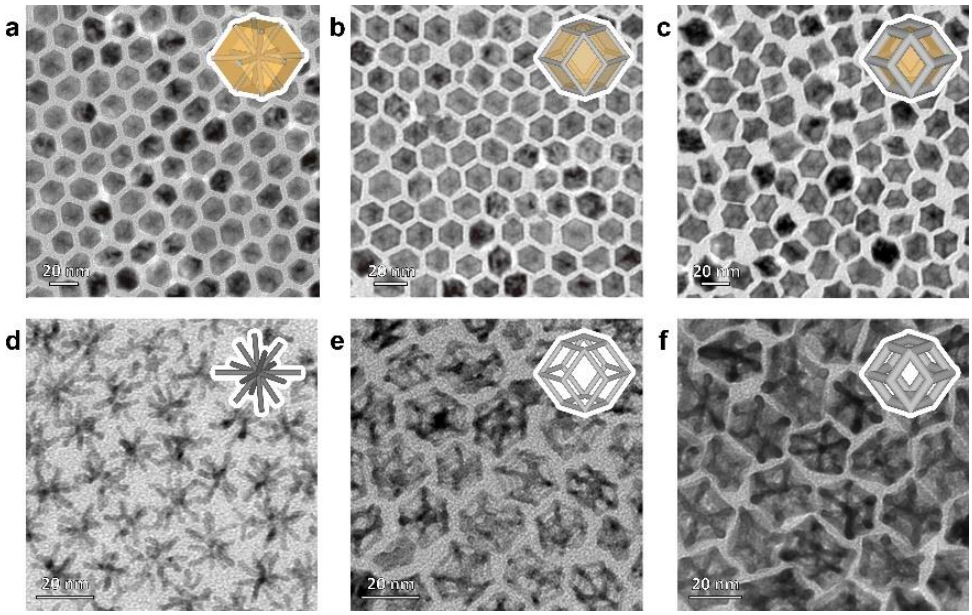


Figure 4.3. Development of RD and corrosion to three-dimensional nanostructures. (a–c) TEM images of rhombic dodecahedra with growth times of 3 min (a), 10 min (b) and 30 min (c) after the growth solution turns black. (d–f) TEM images of the corresponding products of (a–c) after removal of the Ni-rich phase by selective chemical corrosion, which reveal the morphology of the Pt-rich phase in the parent solid particles. Insets in (a–f) are geometrical models, in which the grey color represents Pt-rich phase and orange represents Ni-rich phase.

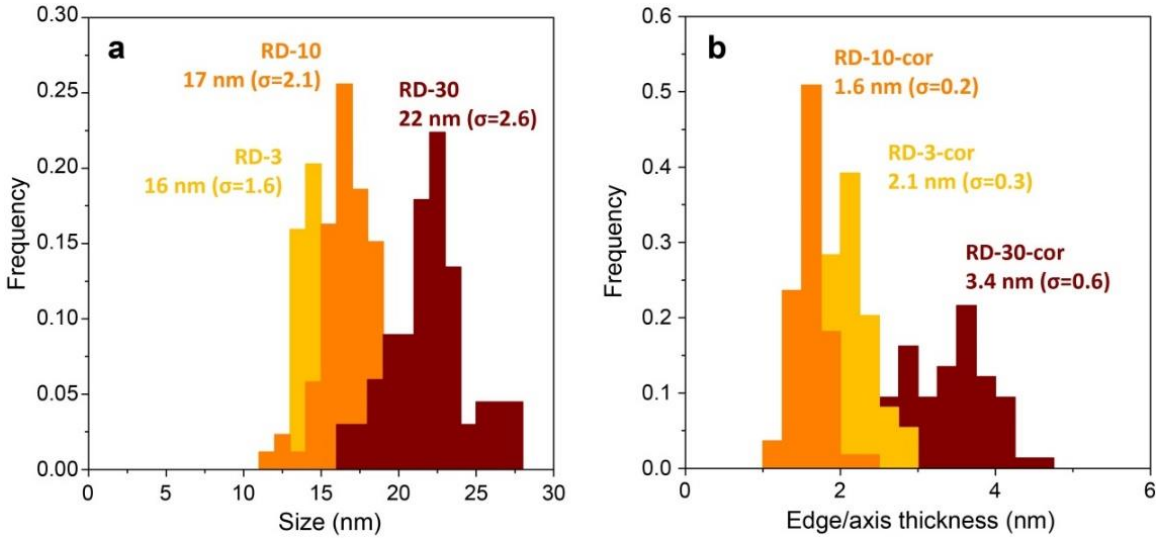


Figure 4.4. Size distributions of solid Pt-Ni RD and corroded products. (a) Histograms of size distributions of RD-3, RD-10, and RD-30. (b) Histograms of axis or edge thickness distributions of RD-3-cor, RD-10-cor, and RD-30-cor.

have multiple long arms with a thickness of 2.1 nm (σ = 0.3, Fig. 4.4b). The arms are identified as the 14 axes of the parent rhombic dodecahedron stretching from origin to vertex (Fig. 4.6), on the basis of the representative projected geometries (Fig. 4.7a–c). Therefore, RD-3-cor is named a tetradecapod. There are two types of axes in a rhombic dodecahedron, with the crystallography of a fcc alloy dictating that an axis is along either the <111> or <200> directions. The HRTEM and corresponding fast Fourier transforms (FFT, Fig. 4.7d–f) agree perfectly with this model. It should be restated that the <111> and <200> directions are precisely the growth directions of the branched intermediates (Fig. 4.1e and Fig. 4.2), so the Pt-rich phase had only further segregated to the axes inside RD-3, leaving uniform arms in the RD-3-cor tetradecapod. Alternatively, RD-10 and RD-30 transformed into nanoframes after the corrosion (Fig. 4.3e, f), consistent with the previous finding of Yang et al.[187] The average thickness of the frames' edges increased from 1.6 nm (σ = 0.2) for RD-10 to 3.4 nm (σ = 0.6) for RD-30 (Fig. 4.4b), suggesting more Pt enriched on the edges with prolonged growth time.

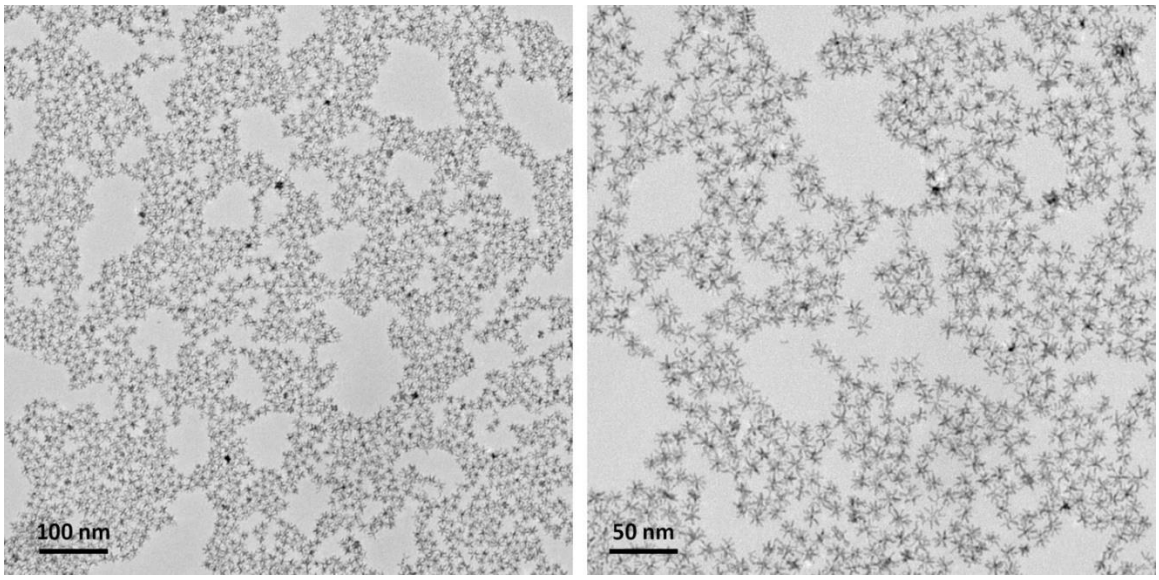


Figure 4.5. TEM of RD-3-cor with different magnifications. Low-magnification image illustrates that the uniformity of the product is maintained after chemical-corrosion. High-magnification image illustrates the many projections possible for a tetradecapod.

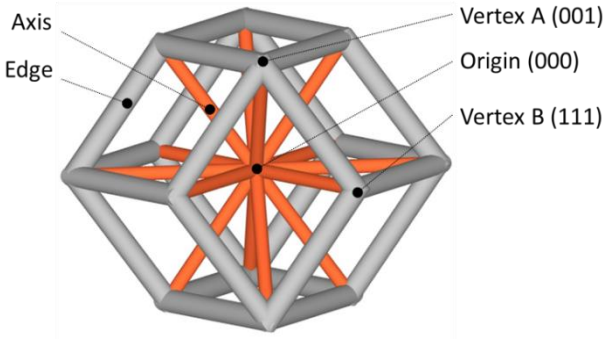


Figure 4.6. Geometric model of rhombic dodecahedron. The differences between the identifiers used in the text are indicated: *axis*, *edge*, two types of *vertex* and *origin* are labeled.

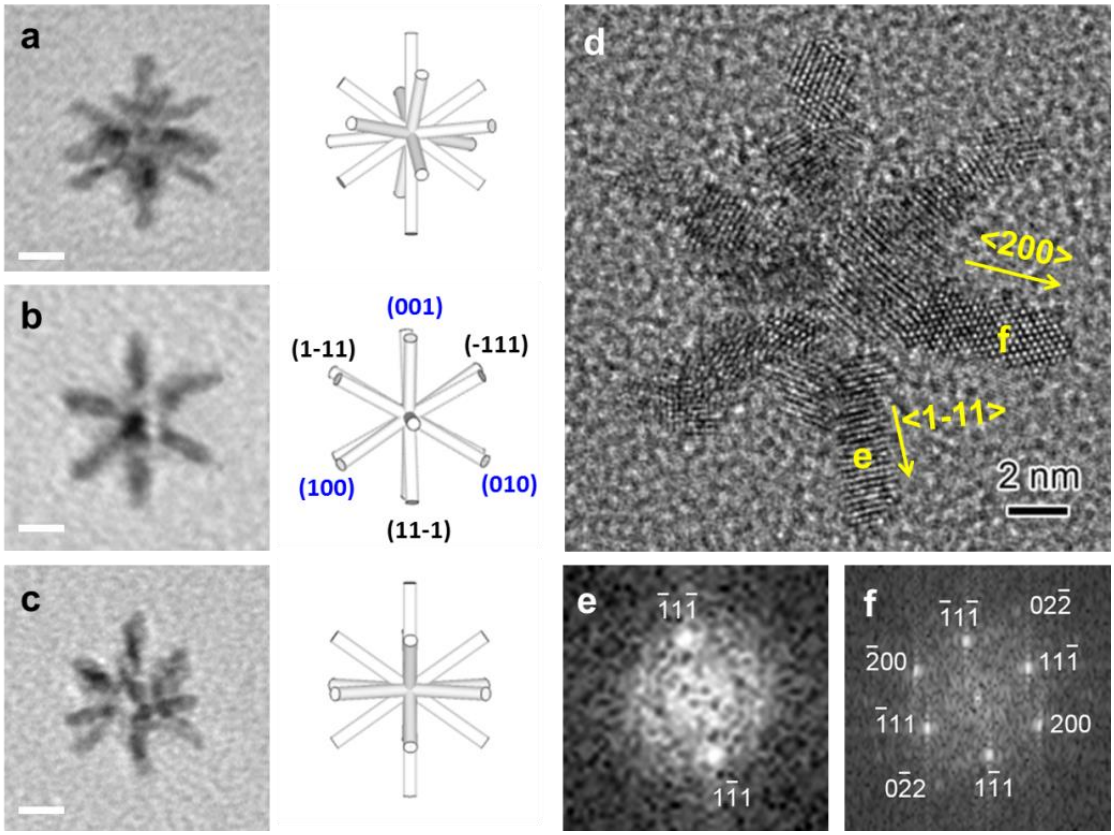


Figure 4.7. In-depth examination of tetradecapod geometry. (a–c) TEM images of the RD-3-cor tetradecapod with typical projections that are similar to the geometrical models to their right. (d) HRTEM image of a typical tetradecapod viewed along [111] zone axis. The growth directions of the marked two arms are along <1-11> and <200> as indicated by corresponding FFTs (e, f). The structure is in perfect agreement with the geometrical model (b, right). Scale bars in a–c are 5 nm.

The spatial distributions of Pt and Ni in the rhombic dodecahedra at different growth times were further characterized by HAADF-STEM and EDS mapping (Fig. 4.8a–c). The samples were viewed along the [111] zone axis to compare their hexagonal projections. It clearly shows that Ni is distributed homogeneously in all three stages of the dodecahedron, whereas Pt is mainly distributed on the diagonals of the hexagon for RD-3, and also on the six sides of the hexagon in RD-10 and RD-30. This is consistent with the three-dimensional models in which the Pt-rich phase segregated on the 14 axes for RD-3 and on the 24 edges for RD-10 and RD-30. Notably, RD-30 has much thicker Pt-rich diagonals and sides than RD-10, which were conserved in the corroded product. In RD-3-cor, RD-10-cor and RD-30-cor, the Pt and Ni are distributed homogeneously within the respective tetradecapod or frame, and each has an identical composition of $Pt_{75}Ni_{25}$, based on EDS (Fig. 4.8d-f).

The bulk compositions of RD-3, RD-10 and RD-30 determined by EDS coincided well with the ICP-OES results (Table 4.1). RD-3 and RD-10 possessed the same Ni:Pt ratio (9:1). However, the Ni:Pt ratio drastically decreased to 3:1 for RD-30 due to the continued Pt enrichment on the edges of the dodecahedra. XPS showed that Ni enriched on the surface in RD-3, whereas Pt enriched on the surface in RD-10 and RD-30 (Table 4.1). This is consistent with the structural models.

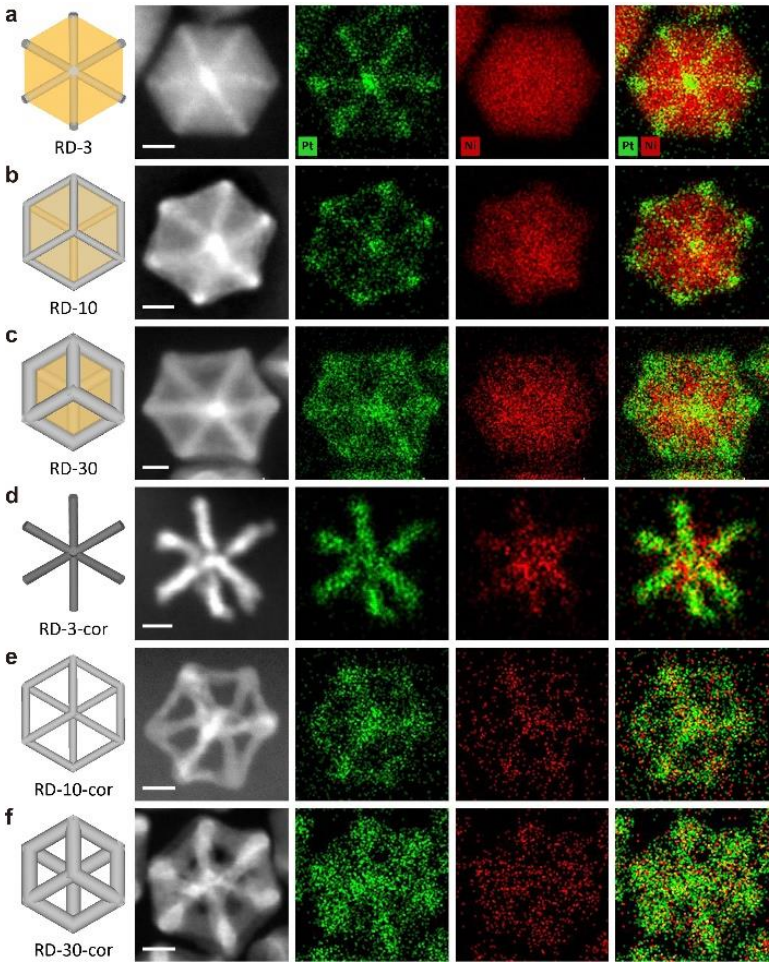


Figure 4.8. STEM–EDS analysis of segregation and migration of Pt in Pt–Ni RD. (a-f) HAADF-STEM and EDS mapping images of rhombic dodecahedra with different growth times of 3 min (a), 10 min (b) and 30 min (c), and their corresponding chemically corroded products (d–f). The intensity of the HAADF image is approximately proportional to atomic number (Z^2).[253] In RD-3, the bright signal represents the Pt-rich arms stretching from the origin to the vertices of the dodecahedron. In RD-10 and RD-30, the bright signal represents the Pt-rich edges of the dodecahedron which construct the nanoframe. In the EDS maps, green color represents Pt and red color represents Ni. Whereas Ni is homogeneously distributed in all three types of rhombic dodecahedra, Pt enriches at diagonals for RD-3 and at both diagonals and six sides for RD-10 and RD-30. In all images, scale bar, 6 nm.

Table 4.1. Compositions of RD-3, RD-10 and RD-30 determined by EDS, ICP and XPS.

Method	Ni:Pt atomic ratio		
	RD-3	RD-10	RD-30
EDS	9:1	9:1	3:1
ICP	9:1	9:1	3:1
XPS	15:1	6:1	2:1

4.5 Phase Segregation in Rhombic Dodecahedra

XRD patterns of RD-3, RD-10 and RD-30 (Fig. 4.9a) were used to characterize their distinctive phase segregation. The diffraction peaks of RD-3 and RD-10 are characteristic of the expected fcc alloy. Using Vegard's rule, their compositions are roughly estimated to be Pt_8Ni_{92}, but this does not account for the asymmetry observed in the diffraction peaks. The asymmetry toward the left confirms that there is a segregated Pt-rich phase diffracting at lower 2Θ values which coexists with the sharply diffracting Ni-rich phase. With increasing reaction time (RD-30), the asymmetric peaks split into two sets of diffraction patterns, which are assigned to a Pt-rich phase ($Pt_{61}Ni_{39}$) and a Ni-rich phase (Pt_8Ni_{92}), again based on Vegard's rule. The peak position of the Ni-rich phase does not change during the entire growth. It is evident that there is a core Pt_8Ni_{92} phase that does not change composition, while Pt enriches on the edges of the dodecahedra and causes the Pt-rich phase to grow larger in lattice constant and in crystallite size. The XRD patterns of the chemically corroded products are also exhibited in Fig. 4.9a. The asymmetric and split diffraction peaks become a single set of symmetric peaks after chemical corrosion, indicating one phase with an estimated composition of $Pt_{75}Ni_{25}$ from Vegard's rule.

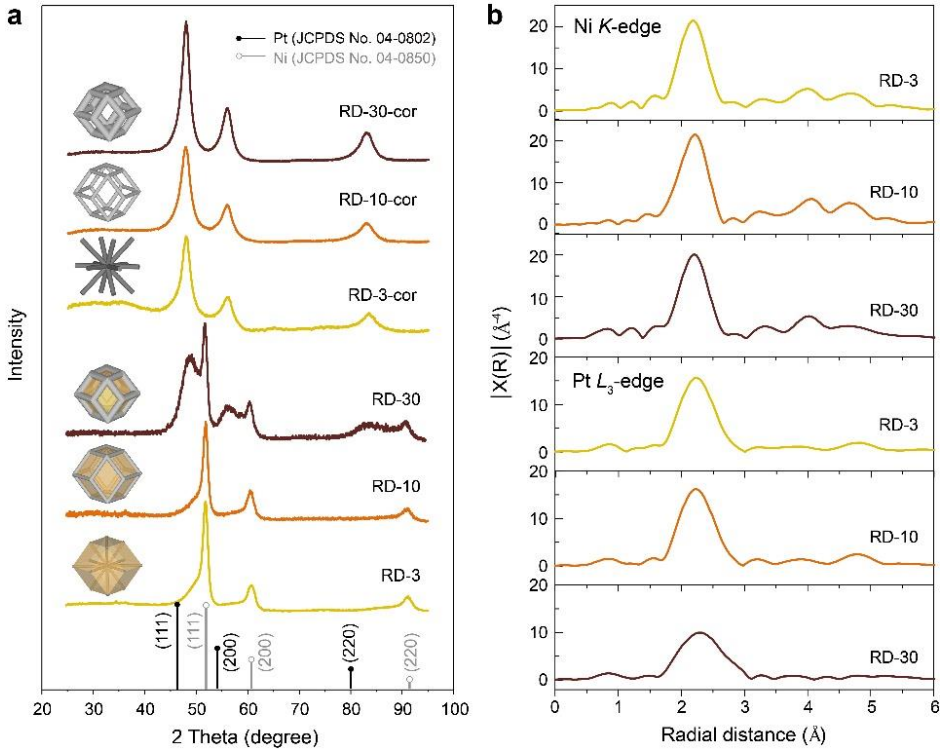


Figure 4.9. Structural evolution over time in Pt–Ni RD. (a) Powder X-ray diffraction patterns of rhombic dodecahedra and their corresponding chemically corroded products. RD-3 and RD-10 show asymmetric diffraction peaks at lower 2Θ that indicate the coexistence of segregated Pt-rich phase. The asymmetric peaks split into two sets of diffraction patterns for RD-30, in which more Pt had grown on the edges. (b) Ni *K*-edge and Pt L_3-edge EXAFS spectra of rhombic dodecahedra. RD-3 and RD-10 have similar EXAFS spectra due to their nearly identical bulk compositions, while RD-30 has lower intensity in its first-shell peaks at the Ni *K*-edge and Pt L_3-edge due to its increased phase segregation and Pt enrichment.

Phase segregation in the rhombic dodecahedra was further confirmed by EXAFS data taken at the Ni *K*-edge and Pt L_3-edge (Fig. 4.9b). For RD-3 and RD-10, the Ni *K*-edge and Pt L_3-edge EXAFS data were successfully co-fit using paths from a disordered fcc $Pt_{10}Ni_{90}$ model (Fig. 4.10).[254,255] The EXAFS fit to RD-30 was performed using paths from a $Pt_{25}Ni_{75}$ disordered fcc model. Additional information

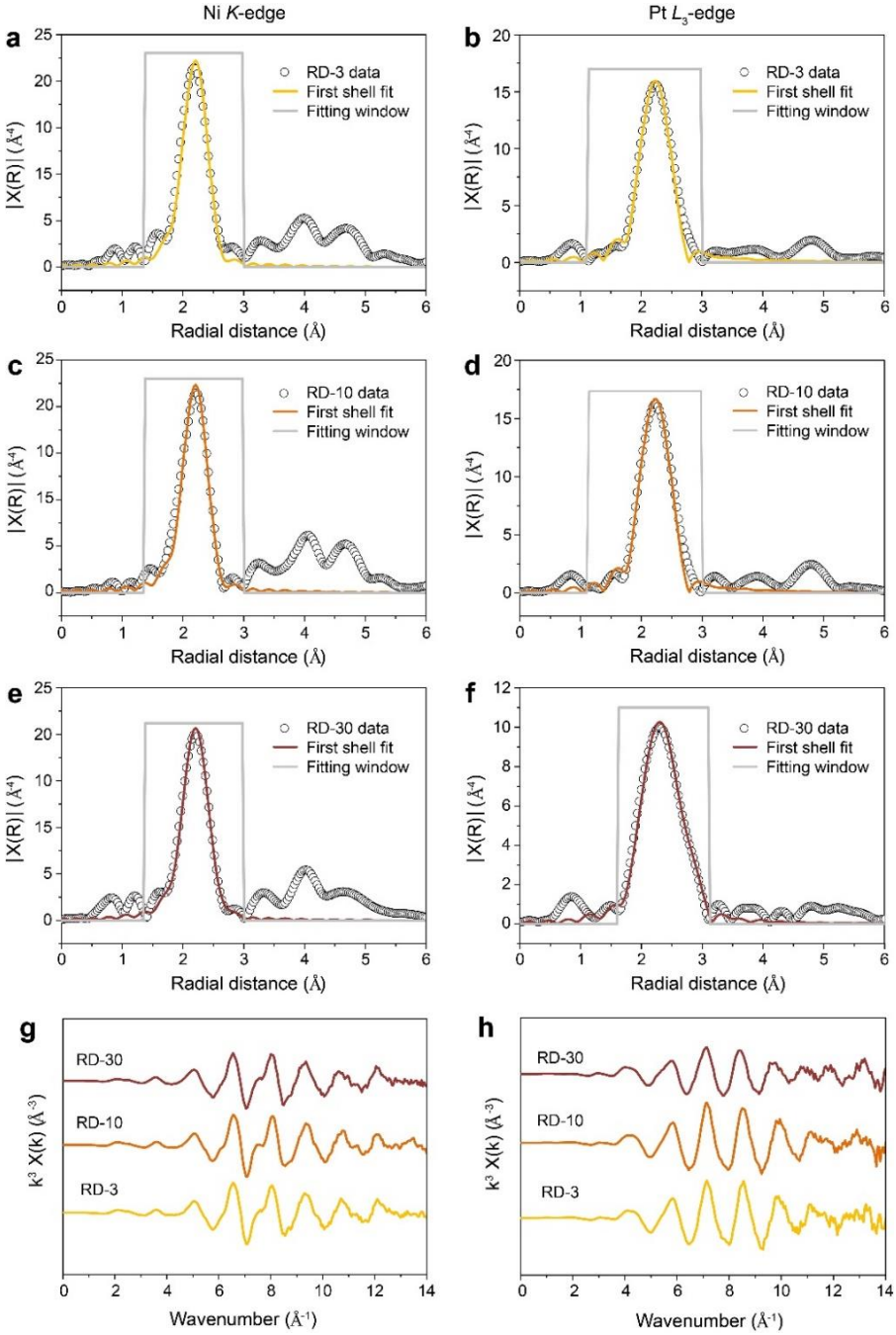


Figure 4.10. EXAFS results for Pt-Ni rhombic dodecahedra. Ni *K*-edge (left column) and Pt L_3-edge (right column) EXAFS spectra and fits to the first coordination shell (a–f). Numerical results of each fit are displayed in Table 4.2. Raw k^3-weighted $\chi(k)$ EXAFS spectra for Ni *K*-edge (g) and Pt L_3-edge (h) for Pt-Ni rhombic dodecahedra. The ΔR fitting windows are indicated on the plots and the Δk fitting windows were 2-14 Å^{-1} for the Ni *K*-edge and 2-12 Å^{-1} for the Pt L_3-edge.

on the fitting procedure is provided in Appendix A3.6. For each sample, the EXAFS-determined coordination numbers were used to calculate the extent of alloying parameters (Table 4.2),[244] which illustrate that Pt and Ni in RD-30 were significantly more segregated from each other than in either RD-3 or RD-10. This more significant phase segregation led to the peak-splitting observed in the XRD pattern for RD-30, whereas the phase segregation in RD-3 and RD-10 caused only peak asymmetry in the XRD patterns.

Table 4.2. EXAFS fitting parameters for RD-3, RD-10, and RD-30.[a]

	RD-3 (co-fit)	**RD-10 (co-fit)**	**RD-30 (co-fit)**
$\Delta E_{0,Ni}$	6.0 (0.9)	6.1 (0.8)	5.8 (0.6)
$\Delta E_{0,Pt}$	7.5 (2.0)	7.3 (1.8)	8.5 (1.2)
N_{NiNi}	7.8 (1.0)	7.2 (0.8)	7.1 (0.6)
N_{NiPt}	1.1 (0.2)	1.1 (0.2)	1.6 (0.3)
N_{PtNi}	9.7 (1.8)	10.0 (1.8)	4.7 (0.9)
N_{PtPt}	-	-	5.9 (1.5)
R_{NiNi}	2.50 (1)	2.50 (1)	2.50 (1)
R_{NiPt}	2.57 (1)	2.57 (1)	2.59 (1)
R_{PtNi}	2.57 (1)	2.57 (1)	2.59 (1)
R_{PtPt}	-	-	2.72 (1)
σ^2_{NiNi}	0.0070 (11)	0.0065 (10)	0.0070 (10)
σ^2_{NiPt}	0.0082 (15)	0.0081 (13)	0.0073 (16)
σ^2_{PtNi}	0.0082 (15)	0.0081 (13)	0.0073 (16)
σ^2_{PtPt}	-	-	0.0065 (17)
R-factor	2.5%	2.0%	0.7%
J_{Ni}	124%	133%	74%
J_{Pt}	111%	111%	59%

[a]Values in parentheses are error bars determined from IFEFFIT.

4.6 Mechanism of Pt Segregation in Rhombic Dodecahedra

An important, yet unaddressed question is how RD-3 with Pt-rich phase segregated to the inner axes progresses to RD-10 with Pt-rich phase segregated to the outer edges. Considering the extremely high similarity of RD-3 and RD-10 in terms of XRD patterns, EXAFS structures, and ICP compositions, it is proposed that their dissimilar elemental distributions are caused by the outward, anisotropic migration of Pt. One would then anticipate that an intermediate structure between RD-3 and RD-10 would have Pt-rich phase segregation on both axes and edges. As shown in Fig. 4.11, the rhombic dodecahedra turned into incomplete nanoframes with Pt-rich phase remaining on both edges and axes after chemical corrosion. In addition, the conversion of RD-3 into RD-10 was attempted under *ex situ* conditions. If RD-3 was separated from the growth solution and annealed in neat oleylamine at 230 °C under N_2, it could be corroded into nanoframes, rather than tetradecapods, because Pt had migrated from the axes to the edges (Fig. 4.12). These control experiments further illustrate the outward, anisotropic migration of Pt from the axes, although the underlying driving force must still be explained.

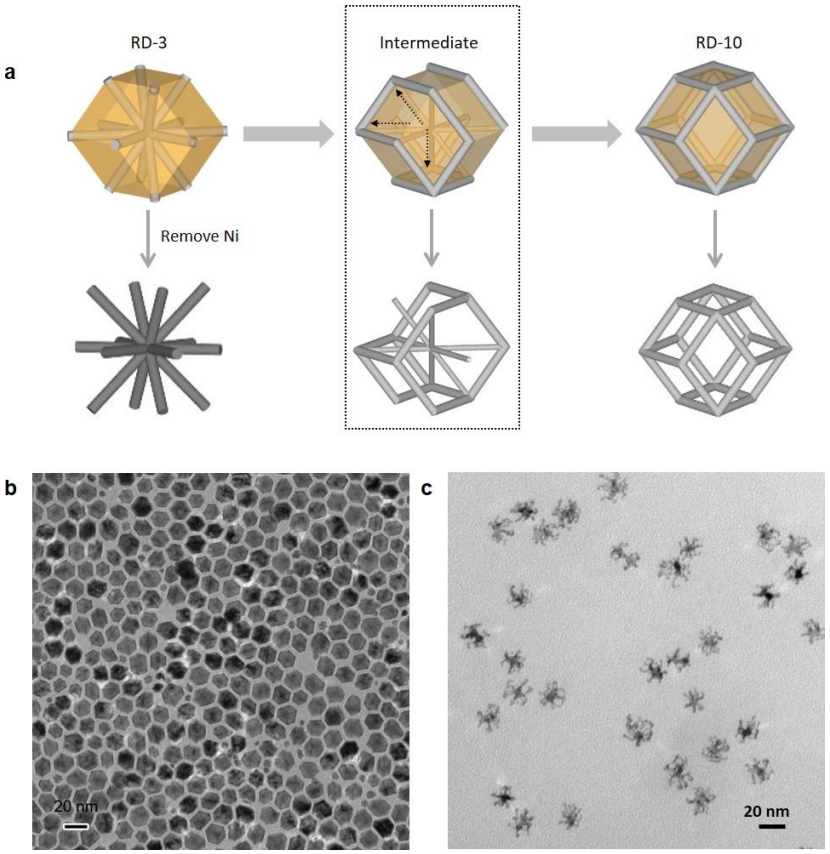


Figure 4.11. Intermediate three-dimensional structures between tetradecapod and nanoframe. (a) Schematic illustration of phase migration from RD-3 to RD-10 via an intermediate structure with Pt-rich phase segregated on both axes and edges. TEM images of products (b) stopped between RD-3 and RD-10 and the corresponding products after chemical corrosion (c). The corroded structures show Pt-rich phase co-exists on both axes and edges.

In a bimetallic alloy, the overall Gibbs energy of the particle must be minimized during any phase segregation that occurs.[93,240,256] Preferential elemental segregation to the surface can result from differences in surface energy and/or atomic radius between the two metals. However, the segregation phenomena must overwhelm the influence of the chemical ordering energy of the alloy system.[240] The Pt–Ni system has ordered phases for $Pt_{25}Ni_{75}$ or $Pt_{50}Ni_{50}$ compositions,[257,258] but the ordering of a given phase at any stage of the growth is not observed by XRD and is unexpected due to the synthetic temperature used.[259] Therefore, the element with lower surface energy is more likely to segregate to the surface unless a significant strain energy is induced by the larger element (which may or may not have lower surface energy), causing it to surface segregate to reduce the strain. Both phenomena are observed in the Pt–Ni rhombic dodecahedron. The rhombic dodecahedral shape exposes exclusively {110} facets, and the surface energies of Pt{110} and Ni{110} are 2.819 and 2.368 $J\,m^{-2}$, respectively.[91] Therefore, it is expected that Ni would preferentially segregate to the faces of the dodecahedron. However, Pt is much larger than Ni, with their atomic radii being 1.39 Å (Pt) and 1.24 Å (Ni).[260] Consequently, the larger Pt atoms on the interior of RD-3 tend to migrate outwards to relieve the internal strain, transitioning to the RD-10 structure. The Pt atoms migrate to vertex and edge sites in RD-10 and RD-30 because Ni-rich facets are highly favored by the lower surface energy

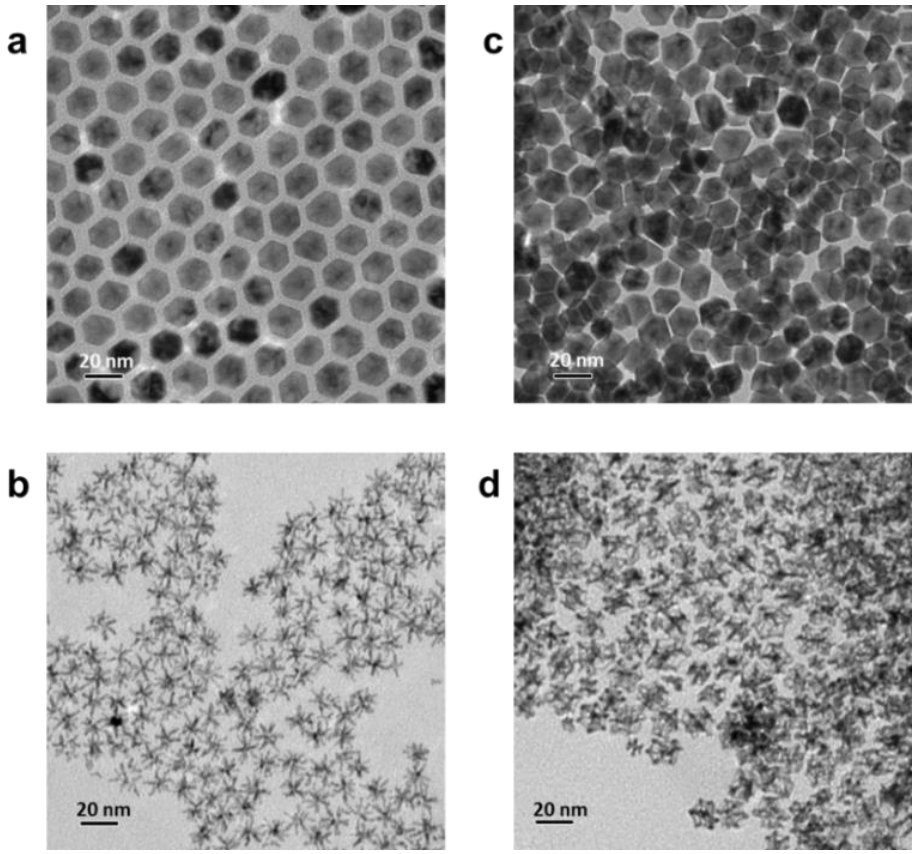


Figure 4.12. *Ex situ* annealing converts RD-3 into "RD-10-like" dodecahedron. TEM images of RD-3 (a) and corresponding RD-3-cor (b), as well as RD-3 after *ex situ* annealing (c) and corresponding corroded product (d). The two distinct pathways are 1) a→b or 2) a→c→d.

of Ni{110}. The progression from an ill-defined branched structure (Fig. 4.1b) to a uniform Pt-rich tetradecapod (Fig. 4.3d and Fig. 4.5) illustrates that Pt furthered its segregation to the axes of the dodecahedron before migrating to the edges. This observation, along with the intermediate structures with partial branch and frame morphology (Fig. 4.11c), implies that RD-3 progresses to RD-10 through migration of Pt along the Pt-rich axes of the dodecahedron to the vertices, and then to the edges. The anisotropic migration is likely guided by the energetic favorability of large Pt atoms diffusing through a Pt-rich phase along the axes, as opposed to diffusing through the Pt_8Ni_{92} phase surrounding the axes in the interior of RD-3 and RD-10.[189]

Having thoroughly characterized the typical products obtained in the growth of Pt–Ni rhombic dodecahedra, the discrete stages can now be pieced together into a whole picture. Fig. 4.13 plots the trend in Pt and Ni content in the products obtained during the whole growth process. From the initial $Pt_{70}Ni_{30}$ nanoparticles, the Ni content increased first to $Pt_{49}Ni_{51}$ for the branched intermediates, and then to $Pt_{12}Ni_{88}$ for the primary rhombic dodecahedra. The substantial increase in Ni content during this period can be attributed to Ni deposition on the low-coordination sites of intermediate structures,[155,156] which arose from anisotropic overgrowth of Pt on the non-spherical seeds. The nickel content then increased slightly more, becoming the $Pt_{10}Ni_{90}$ rhombic dodecahedra (RD-3). The Ni:Pt ratio remained nearly unchanged through RD-10. At the same time, Pt segregated to the axes (RD-3)

and then migrated through the axes onto the edges (RD-10) to minimize the energy penalties arising from the strain of the larger Pt atoms inside the Ni-rich lattice. After the anisotropic migration, the Pt content slowly increased to $Pt_{35}Ni_{65}$ with increasing growth time (40 min). As the well-defined rhombic dodecahedron has fewer step sites, the Ni deposition becomes greatly suppressed during the Pt enrichment stage. The increase in Pt content comes from continued Pt reduction from the remaining precursor in solution onto the edges of RD-10. The Pt-rich phase migration (RD-3 to RD-10) and enrichment (RD-10 to RD-30) are both selectively onto the edges and not the facets of the rhombic dodecahedra, due to the higher surface energy of Pt{110} than Ni{110}. The comprehensive growth trajectory is presented in Fig. 4.13.

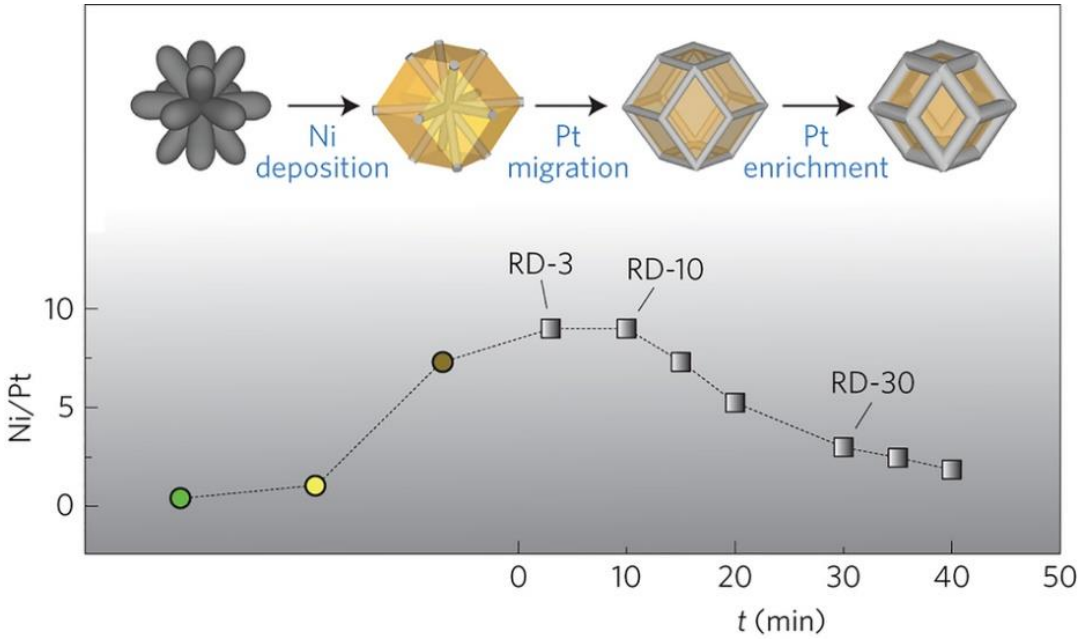


Figure 4.13. Summary of the complete growth process of a Pt–Ni rhombic dodecahedron. The composition plot indicates that Ni content in the products increases first and then decreases. Compositions in the plot are determined by EDS for circles and by ICP for squares. The colors of the circular points represent the colors of the growth solution from which the products were obtained. The schematic illustration of the growth mechanism exhibits three growth regimes: Ni deposition on the step sites of Pt-rich branch structures; anisotropic migration of Pt from axes to edges; continued enrichment of Pt on edges. In the scheme, grey color represents the Pt-rich phase while orange represents the Ni-rich phase.

The results of this study lend insight into novel methods for constructing nanocatalysts with desired performance using designed phase segregation patterns. This concept was demonstrated by measuring the oxygen reduction activity of RD-3-cor, RD-10-cor and RD-30-cor (Fig. 4.14). The advantage of controlling Pt segregation to the edges of the rhombic dodecahedron is clear in that both the specific activity and mass activity of the open nanostructures can be tuned to higher values by allowing Pt edge segregation to increase. The activity trend observed demonstrates the beneficial effects of tuning morphology and size, which can affect the coordination and strain of surface atoms performing catalysis.[107,154]

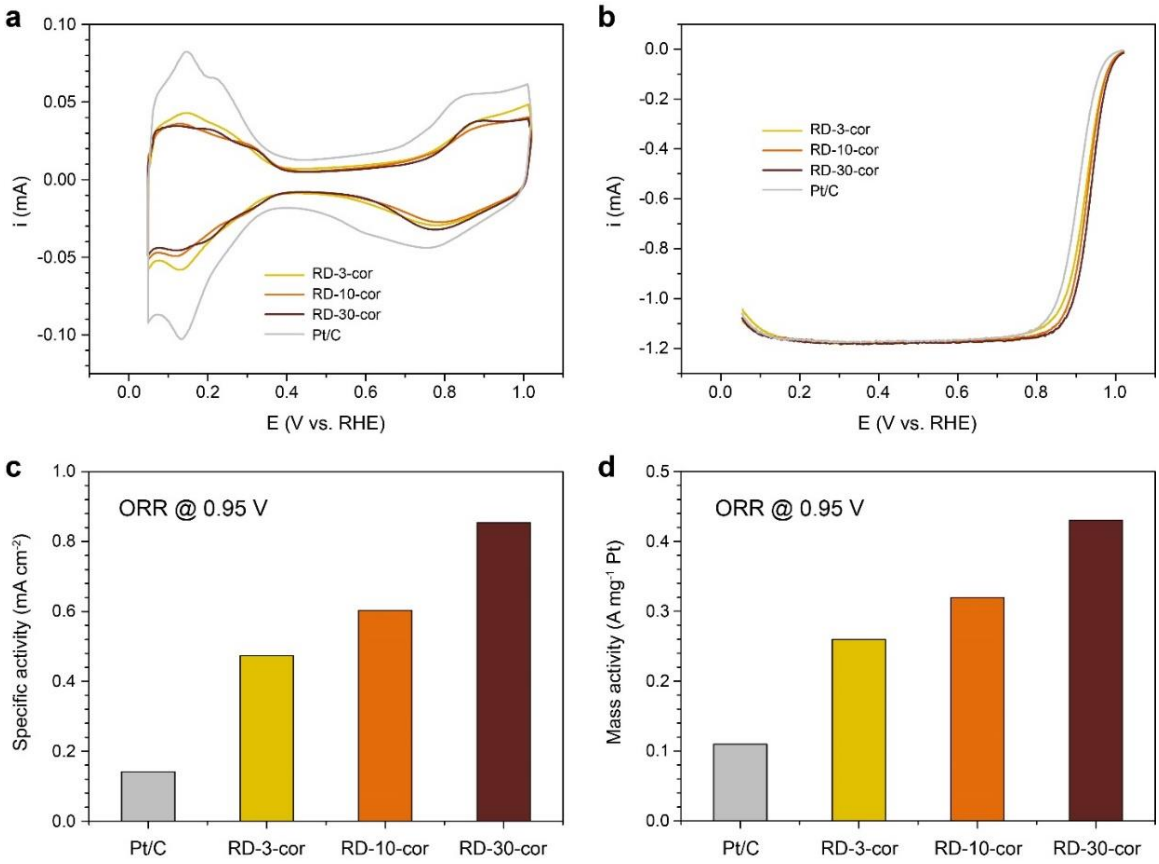


Figure 4.14. Oxygen reduction activity of tetradecapods and nanoframes. Hydrogen underpotential deposition cyclic voltammograms (a) performed in Ar-saturated 0.1 M $HClO_4$ at 50 mV/s. Rotating disk electrode oxygen reduction curves (b) collected in O_2-saturated 0.1 M $HClO_4$ at 20 mV/s with a rotation rate of 1,600 rpm. Specific activity (c) and mass activity (d) of tetradecapods and nanoframes compared to commercial Pt/C. All Pt-Ni catalysts had a CO_{ad}:H_{upd} = 1.0, where CO_{ad} and H_{upd} represent the ECSA calculated from the CO-stripping and hydrogen underpotential deposition techniques, repsectively.[249] Specific surface area measurements were determined to be 54.4 m^2/g_{Pt} (RD-3), 53.0 m^2/g_{Pt} (RD-10), and 50.4 m^2/g_{Pt} (RD-30).

4.7 Conclusions

This work has revealed through Pt–Ni rhombic dodecahedra that the growth of shaped, bimetallic nanostructures is a complex, concurrent evolution of their composition, element spatial distribution, and morphology. Such intricate phenomena are consequences of a series of fundamental chemistries, including un-matched reduction potentials of metal precursors, anisotropic overgrowth on preformed seeds, step-induced metal deposition, and site-dependent phase segregation and migration. The growth trajectory of a bimetallic nanostructure therefore relies on how these fundamental steps are maneuvered. The anisotropic overgrowth can be modified by the type of seed present in the growth solution and the ligand coordination strength to the facets of the seed.[139,261,262] It is possible that the growth direction could be exclusively along the <111> or <200> directions if the seeds take an octahedral or cubic shape or if ligand binding is favored on either the {111} or {100} facets. In the growth of Pt–Ni rhombic dodecahedra, the near-spherical seeds had {111} and {100} facets and the

overgrowth was bidirectional. Unidirectional overgrowth along the <200> direction was observed in the growth of Pt–Ni octahedra using dimethylformamide-solvated acetylacetonate as the ligand. The final product exhibited a phase segregation pattern with Ni enriched on the {111} facets of the octahedron.[155]

After the initial anisotropic growth, anisotropic migration of the segregated phase can further tune the functionality of the nanocrystal. In Pt–Ni rhombic dodecahedra, phase segregation and migration allowed for $Pt_{75}Ni_{25}$ tetradecapods or nanoframes to be obtained after chemical corrosion of nickel inside the particles. The nanoframe structure was previously demonstrated as capable of drastically improving material utility and ORR activity due to its open structure with three-dimensional molecular accessibility. This unique electrocatalyst design was made possible through distinct stages of the nanocrystal growth. Pt-rich anisotropic growth provided the structure-directing seed to form rhombic dodecahedra. The Pt-rich phase then migrated anisotropically through the axes of the dodecahedron to its vertices and edges, which were further enriched with Pt. These findings highlight the importance of anisotropic growth and site-dependent phase segregation and migration mechanisms for controlling the compositional heterogeneity in bimetallic nanostructures, offering a radically different approach to the fabrication of nanocatalysts with enhanced performance.

5. Excavated Nanoframes

Portions of the content of this chapter are reprinted or adapted with permission from N. Becknell[†], Y. Son[†], D. Kim, Y. Yu, Z. Niu, T. Lei, B. T. Sneed, K. L. More, N. M. Markovic, V. R. Stamenkovic, P. Yang, "Tunable Architecture of Rhombic Dodecahedral Pt-Ni Nanoframe Electrocatalysts", Manuscript in preparation.

5.1 Preface

The improved understanding of the complete mechanism behind the formation of a Pt-Ni rhombic dodecahedron, which can be etched into a hollow Pt_3Ni nanoframe, opened up new opportunities to control the anisotropy of Pt. This could enable new shapes and/or surface features to be exposed on a nanocrystal catalyst, leading to novel properties. In Chapter 5, a simple control over the Pt and Ni precursor ratio was used to drastically alter the Pt anisotropy within the rhombic dodecahedron such that an excavated nanoframe, with no hollow spaces but extremely thin interior sheets, was synthesized. The excavated nanoframe demonstrated excellent activity for the oxygen reduction reaction.

5.2 Introduction

The PEMFC is a critical technology to enhance the clean, sustainable production and usage of energy for society, implementing hydrogen as the energy storage medium.[23] Hydrogen fuel for the PEMFC can be obtained by water electrolysis powered by a renewable energy source, completing the sustainable and carbon-free water cycle.[3,263] Initial applications of PEMFCs have been to replace the gasoline engine in powering personal vehicles.[21] A major roadblock preventing PEMFCs from increased infiltration into the transportation sector is the cost of the platinum-based catalysts that perform the ORR in the cathode.[23] Although Pt shows the highest catalytic activity among the elements of the periodic table, its necessity must be reduced within a fuel cell cathode in order to be cost-competitive with gasoline powered vehicles.[22]

In order to improve the ORR reaction rate and diminish Pt loading in the cathode, major efforts have been placed on the study of Pt alloys with cheap, 3d transition metals.[24,83,125,187,264] Implementation of these alloys, which demonstrate higher activity than pure Pt, in nanoparticle catalysts allows for the Pt-based mass activity to reach the magnitude required to significantly reduce the cost of PEMFCs while maintaining performance, though improvement is still needed. Specifically, evaluating and discovering optimal element spatial distributions at both the atomic level and the nanoscale has been a major area of focus. Stamenkovic et al. have shown that activity can be enhanced by inducing surface atomic rearrangement to create Pt-skin structures from Pt-skeleton surfaces in Pt-Ni alloys.[82,163,165,249] In Pt-skin structures, it is the atomic scale segregation of Ni just beneath the pure Pt surface that tunes the electronic structure of the surface for enhanced ORR activity. On the nanoscale, control over the element spatial distribution in bimetallic alloys can create unique nanoparticle structures that enhance

the activity for ORR.[154,265] By taking advantage of various mechanistic steps in nanoparticle synthesis, such as nucleation, step-induced deposition, and atomic diffusion, an anisotropic distribution of one or both elements within a bimetallic nanoparticle can be obtained.[155] In recent reports, Pt-rich edges could be formed in Pt-Ni and Pt-Co rhombic dodecahedral nanoparticles through Pt migration from the interior of the rhombic dodecahedron and segregation to the edges.[187,250] These Pt-rich edges remained after corrosion of the Ni-rich interior, resulting in Pt_3Ni or Pt_3Co nanoframes (NF). Here, control of the element spatial distribution in Pt-Ni rhombic dodecahedra is used to prepare different Pt anisotropy within the dodecahedron. The resulting nanoframe has a unique morphology leading to enhanced ORR catalytic activity.

5.3 Control of Pt Anisotropy in Rhombic Dodecahedra

By control of the concentration and ratio of Pt and Ni precursors (see Appendix A4 for details), thereby adjusting their chemical potentials, the three-dimensional elemental distributions in solid rhombic dodecahedra (SD) was altered to have either only Pt-rich edges (Fig. 5.1a) or Pt-rich edges together with Pt-rich sheets inside the SD (Fig. 5.1b). The synthetic mechanism of formation of the Pt-Ni SD as discussed in Chapter 4 begins with the formation of Pt-rich branches followed by step-induced Ni deposition between the branches (Fig. 5.2).[265] At this stage, it was discovered that preferential deposition of Pt could be induced by lowering the Ni precursor concentration and

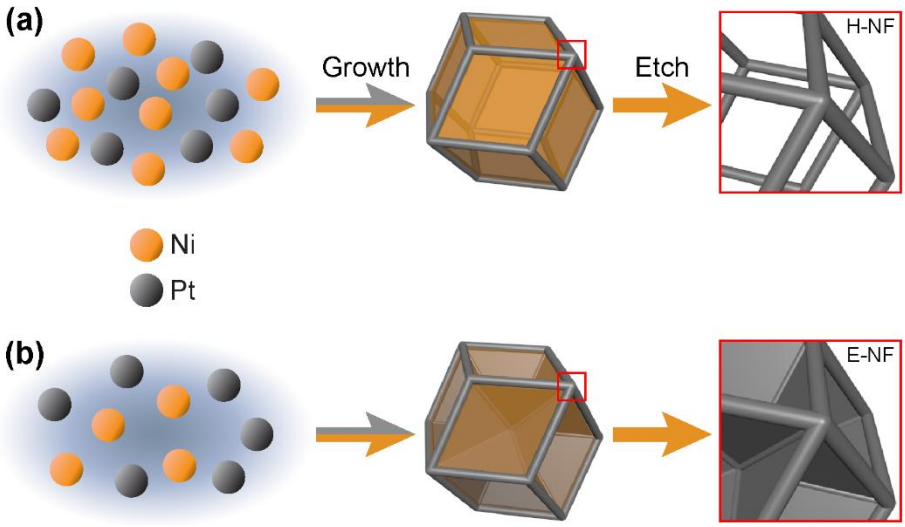


Figure 5.1. Scheme of Pt anisotropy control strategy. Illustration of the synthetic difference between (a) hollow nanoframe (H-NF) and (b) excavated nanoframe (E-NF). In the models, orange represents Ni-rich regions and gray represents Pt-rich regions.

reducing its chemical potential. The faster deposition rate of Pt than Ni led to higher Pt composition of the SD. During the growth process, the excess Pt was deposited between the Pt-rich branches in addition to segregating to the edges and branches, resulting in Pt-rich sheets inside the SD. The sheets are bordered by both interior branches and exterior edges of the SD. Ni eventually deposited in the concave sites formed by the growing branches and sheets in order to fill out the rhombic dodecahedron. This synthetic control allowed for excavated nanoframes (E-NF) to be formed after Ni corrosion that contain not only Pt-rich edges, but also {110}-terminated sheets extending inward

from the edge of the nanoframe. If the Ni concentration was kept high during the synthesis, hollow nanoframes (H-NF) similar in morphology to the previous work could be obtained.[187,249,250,265] The E-NF demonstrated significantly enhanced ORR specific activity over the H-NF due to its extended surface facets and was able to maintain high mass activity due to the thin sheet structure.

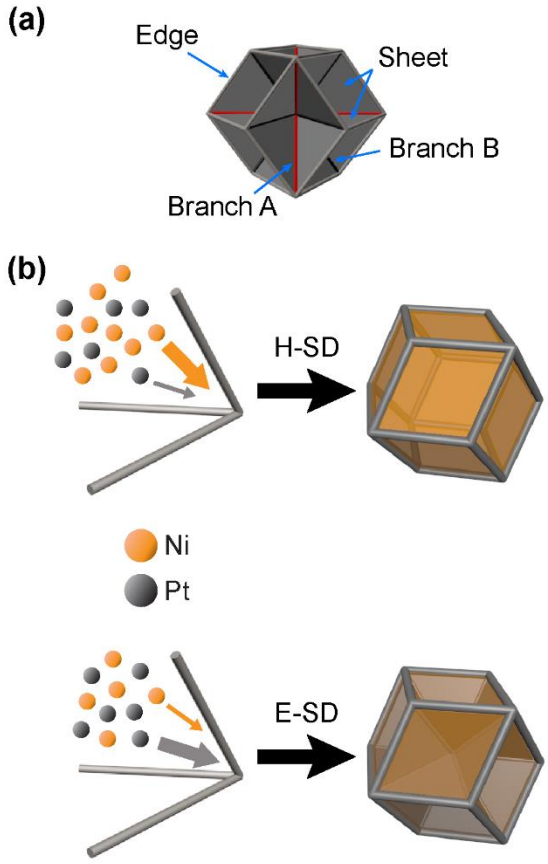


Figure 5.2. Rhombic dodecahedron growth schemes. (a) Explanation of terminology used throughout this chapter to describe the locations of the atoms. On its exterior, the rhombic dodecahedron has 24 *edges*. On its interior, it also has 6 *branches* of type A (red) and 8 *branches* of type B (black) that extend from the origin to each vertex. Branch A grows in the <100> direction while branch B grows in the <111> direction. There are 24 triangular *sheets* whose sides are made up of one branch A, one branch B, and one edge. (b) The synthetic mechanism for the formation of Pt-Ni rhombic dodecahedra as described in Chapter 4 suggests that solid dodecahedra (H-SD), which can be etched into H-NF, are formed by Ni deposition that is favored (indicated by thick orange arrow) between branch sites.[265] Therefore, after lowering the Ni precursor concentration, Pt deposition became more favorable (indicated by thick gray arrow), leading to solid dodecahedra (E-SD) that can be etched into E-NF. Eleven of the fourteen branches have been left out of the scheme for clarity. In the models, orange represents Ni-rich regions and gray represents Pt-rich regions.

Fig. 5.3a-d shows TEM and scanning electron microscopy (SEM) images for H-NF and E-NF. Though the SD precursors to H-NF and E-NF (H-SD and E-SD) exhibited similar morphology to each other (Fig. 5.4), Fig. 5.3a-b demonstrates the clear hollowness inside H-NF, while E-NF displayed sheet-like structures extending inward from the edges of the nanoframe in Fig. 5.3c-d. As

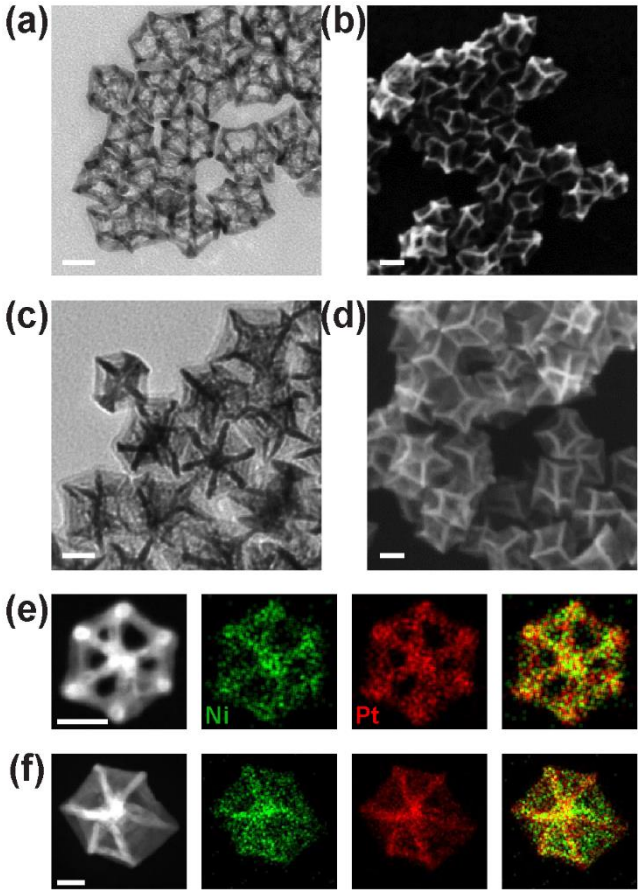


Figure 5.3. Comparison of hollow and excavated nanoframes. TEM and SEM images of (a, b) H-NF and (c, d) E-NF (scale bars represent 20 nm). STEM-HAADF image and STEM-EDS mapping of (e) H-NF and (f) E-NF oriented in the <111> direction (scale bars represent 10 nm).

shown in Fig. 5.1, the NF edges (and sheets in the case of E-NF) remain after corrosion of Ni due to their Pt-rich composition. Fig. 5.3e-f shows STEM- HAADF images and STEM-EDS mapping of pristine H-NF and E-NF oriented in the <111> direction. The lack of Pt and Ni signal inside H-NF is evident, whereas E-NF exhibited a uniform distribution of Pt and Ni throughout its structure between the edges. For reference, Fig. 5.5a shows STEM-HAADF and STEM-EDS for E-NF in the

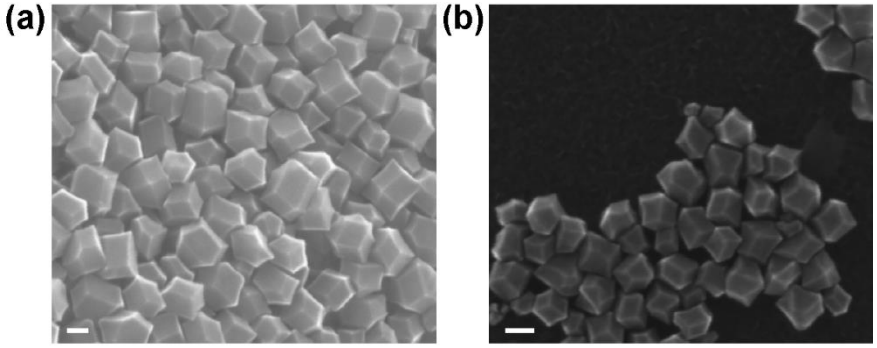


Figure 5.4. Morphology of solid dodecahedral nanoparticles. SEM images of solid rhombic dodecahedral precursors to (a) hollow nanoframe and (b) excavated nanoframe. The solid precursors to the nanoframes were named H-SD and E-SD, respectively. Scale bars represent 30 nm.

<110> direction with clear sheet formation extending from edge to edge. Fig. 5.5b and 5.5c show dense and uniform Ni distribution in H-SD and E-SD, respectively, because the Ni has not yet been corroded. Similar to the NF case, E-SD exhibited Pt distribution throughout the particle while Pt signal can only be observed on the edges of H-SD. Here, the two major differences between the synthesis of SD in this work and previous work are emphasized.[187] First, the amount of Ni^{2+} precursor used for H-SD and E-SD is ~120% and ~70%, respectively, of the amount used in previous work in order to control anisotropic Pt segregation and tune the morphologies of the resulting nanoframes. Second, in this work, the precursors are dissolved in oleylamine before injection, while in the previous work, the precursor solution was aqueous.

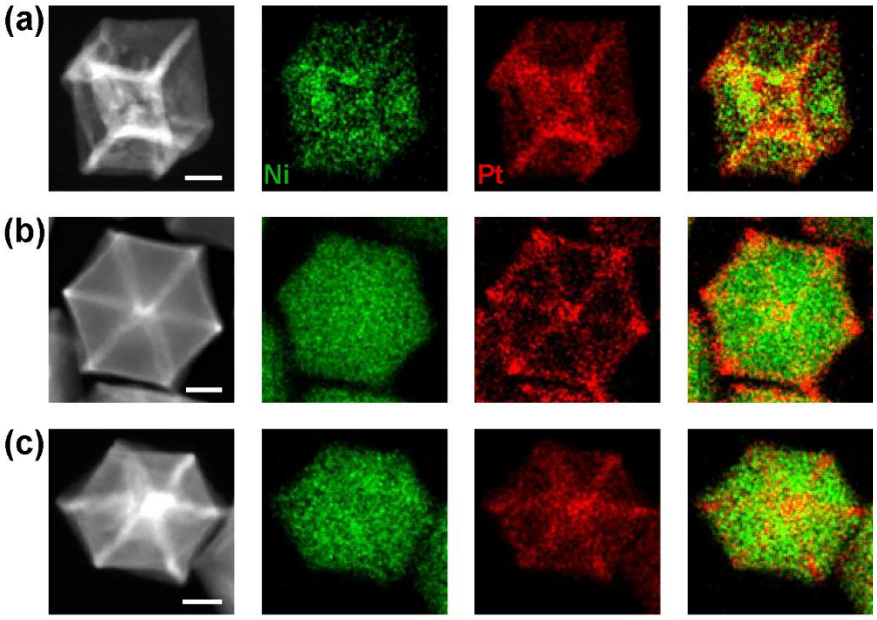


Figure 5.5. Elemental mapping of hollow and excavated anisotropies. STEM-HAADF and EDS mapping of (a) E-NF, oriented in the <110> direction, and (b) H-SD and (c) E-SD, both oriented in the <111> direction. Scale bars represent 10 nm.

5.4 Phase Segregation in Rhombic Dodecahedra

Fig. 5.6a shows powder XRD patterns of NFs and corresponding SD samples. All samples showed face-centered cubic crystalline structure with diffraction peak positioning dependent on the composition of Pt and Ni. Both NFs had (111) peak positions at lower 2Θ than the corresponding SDs due to their Pt-rich compositions after Ni corrosion. E-NF had narrower diffraction peaks than H-NF, with E-NF and H-NF measuring 1.13° and 1.83° full width at half maximum (FWHM), respectively, at the (111) peak position (Fig. 5.6b). Based on the Scherrer equation, with all other variables being equal, the smaller FWHM in the E-NF pattern is a manifestation of a larger crystal grain size.[266] This is consistent with E-NF having an extended sheet structure connected to the edges of the frame that results in larger grains. Fig. 5.6c and 5.6d indicate the degree of asymmetry in the (111) peak of H-SD and E-SD. The (111) peak of H-SD has a sharp component from the large grain of Ni-rich phase in H-SD. Due to the significant segregation of Pt to the edges of H-SD, there is also an obvious asymmetry toward lower 2Θ. E-SD also revealed phase separation, though the Pt

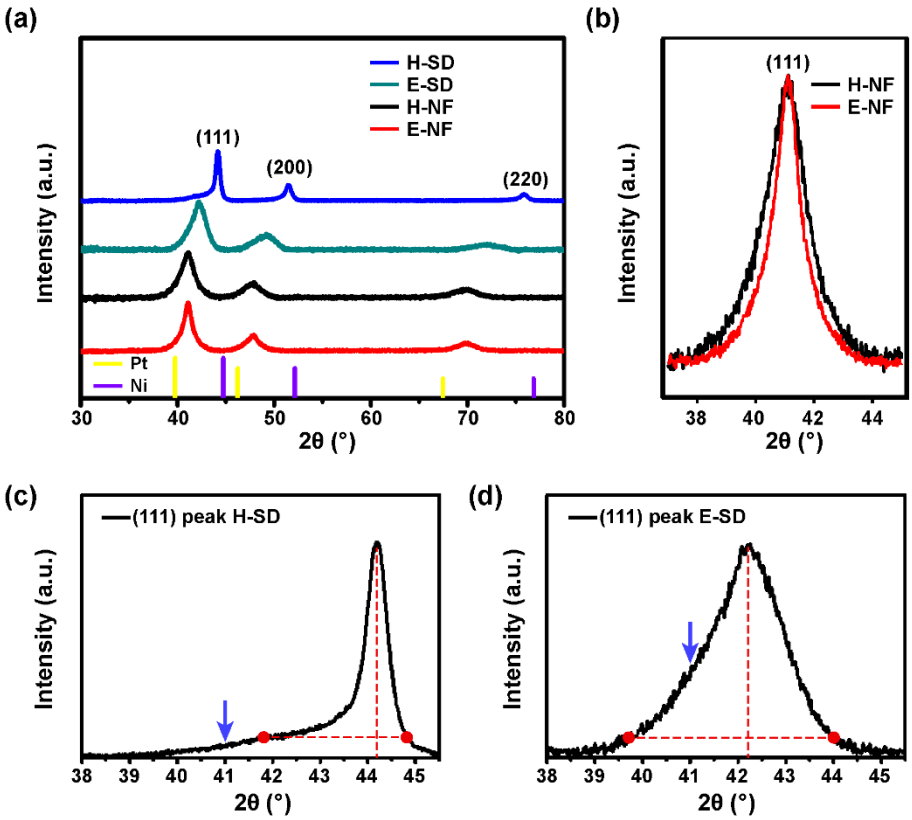


Figure 5.6. X-ray diffraction of solid nanoparticles and nanoframes. (a) XRD patterns for H-SD, E-SD, H-NF, and E-NF. (b) Magnified and overlapped (111) peak of H-NF and E-NF showing larger FWHM for H-NF. Magnified asymmetry of the (111) peak for (c) H-SD and (d) E-SD. Blue arrows in (c) and (d) correspond to the position of the (111) peak of NFs. Red dashed lines are a guide to indicate the degree of asymmetry of each peak.

segregation was evidently less than in H-SD as observed by the smaller degree of asymmetry. The blue arrows in Fig. 5.6c-d indicate the (111) peak position of the corresponding NFs, which is the diffraction contribution from the Pt-rich phase in the SD samples. In addition to the (111) peak position of E-SD being at lower 2Θ than that of H-SD, the intensity at the position of the blue arrow is much larger in E-SD, indicating a larger fraction of the Pt-rich phase.

Table 5.1 presents experimental composition measurements of NFs and SDs. As previously mentioned, the XRD patterns of both SD samples showed severe asymmetry due to phase segregation

Table 5.1. Compositions of hollow and excavated solid nanoparticles and nanoframes.

	ICP	XPS
H-SD	Pt_9Ni_{91}	$Pt_{19}Ni_{81}$
E-SD	$Pt_{29}Ni_{71}$	$Pt_{32}Ni_{68}$
H-NF	$Pt_{67}Ni_{33}$	$Pt_{80}Ni_{20}$
E-NF	$Pt_{65}Ni_{35}$	$Pt_{73}Ni_{27}$

such that it is difficult to assign a specific composition for each sample based on XRD. However, bulk composition information could be obtained from ICP-OES. In addition, the surface composition was obtained from XPS measurements. According to the Beer-Lambert law, the intensity of emitted photoelectrons reaching the electron analyzer in XPS exponentially decays with the depth from which the electrons are emitted.[267] Thus, the composition results from XPS represent the surface-focused composition. The surface composition of H-SD showed increased Pt concentration compared to the bulk due to Pt segregation to the edges of the rhombic dodecahedron. In contrast, E-SD showed very similar Pt composition at the surface and in the bulk. This comparison indicated that the Pt-rich domains evident from XRD and STEM-EDS must be located equally on the exterior and interior of E-SD. These Pt-rich domains survive after chemical corrosion of Ni as the outer frame edges and connected inner sheet structure in E-NF. Therefore, by comparing XPS and ICP composition results between H-SD and E-SD, it was obvious that the location of the thin sheet structure of E-NF was consistent with the TEM analysis.

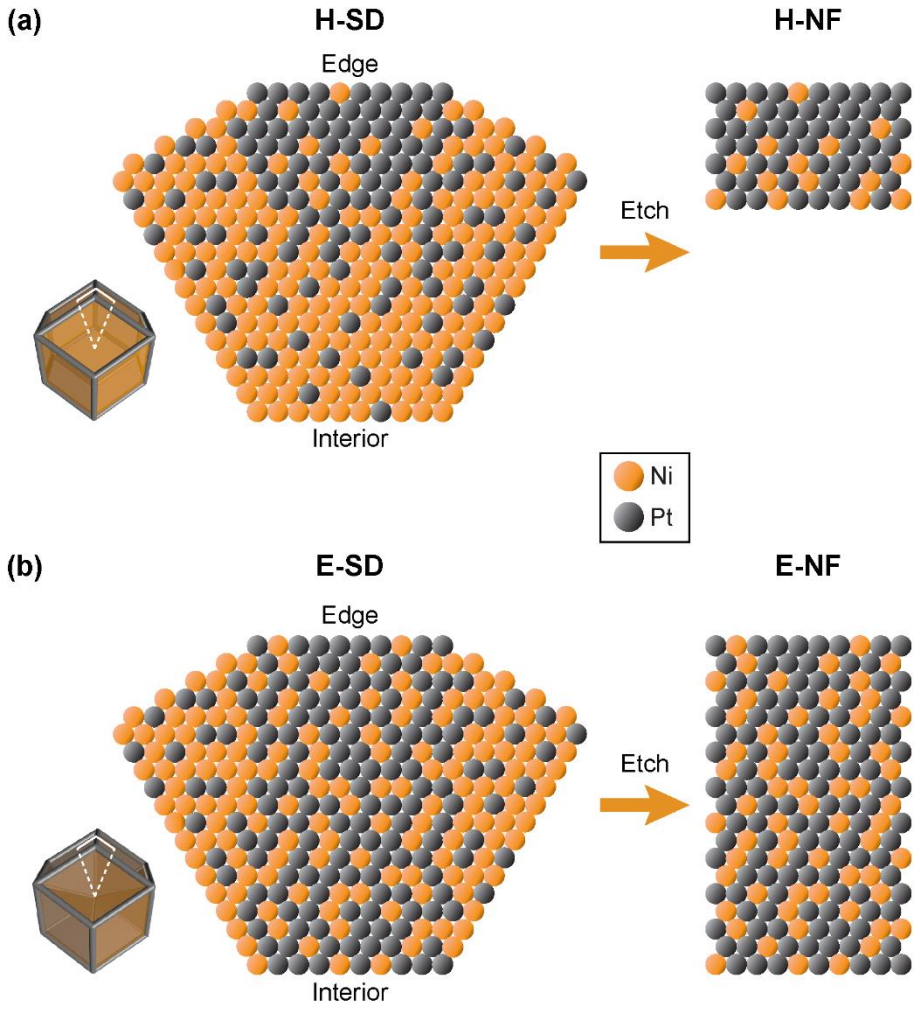


Figure 5.7. Elemental segregation in hollow and excavated solid nanoparticles. Schematic diagram of atomic compositional gradient for (a) H-SD and (b) E-SD and their chemical etching into NFs. White border in three-dimensional SD models indicates cross-section of SD that is atomically modeled in two dimensions. In the 3-D models, orange represents Ni-rich regions and gray represents Pt-rich regions.

In addition, the composition results from ICP and XPS for H-NF and E-NF were compared, with both NFs demonstrating more Pt-rich surface compositions compared to their bulk compositions. However, H-NF exhibited more severe Pt enrichment on its surface. This is consistent with the original phase segregation patterns in as-synthesized H-SD and E-SD. As demonstrated through XRD and STEM-EDS measurements, E-SD had less segregation of Pt from Ni, allowing for the sheet structures to remain after corrosion of Ni. Therefore, it was expected and confirmed by comparison of XPS and ICP that after corrosion, E-NF would have more Ni in the near-surface region than H-NF. A representative scheme of the contrasting elemental segregation gradients in H-SD and E-SD, which led to different near-surface Ni compositions in H-NF and E-NF, is demonstrated in Fig. 5.7. The reduced segregation of Pt from Ni in E-NF was further confirmed by EXAFS analysis (Fig. 5.8) of H-NF and E-NF, where E-NF demonstrated a greater extent of alloying (J_{Pt} and J_{Ni}) compared to H-NF (Table 5.2, see Appendix A4.5 for additional details).[244] Since the extended sheet structure in

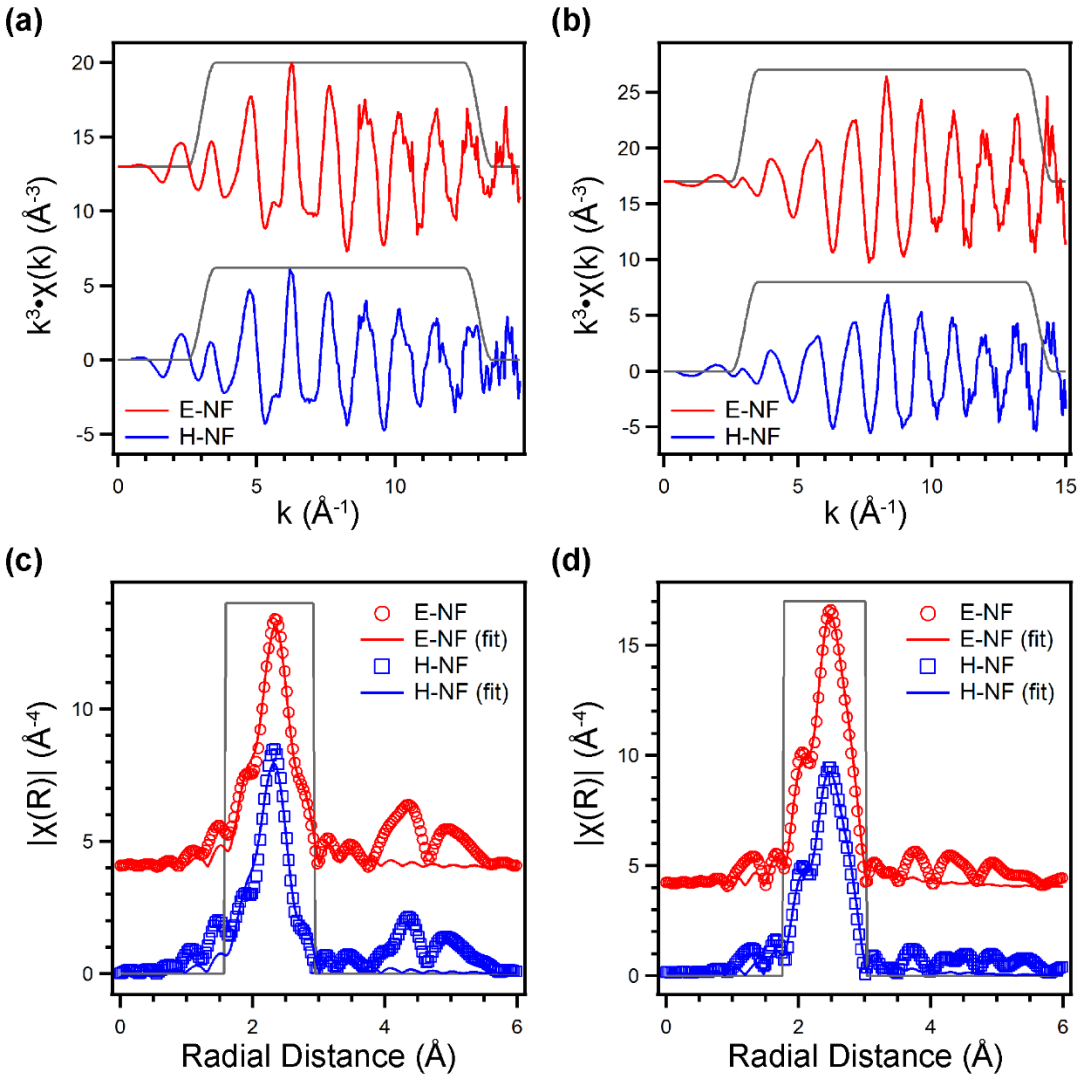


Figure 5.8. EXAFS of hollow and solid nanoframes. EXAFS χ(k) data at the (a) Ni K-edge and (b) Pt L_3-edge for both H-NF and E-NF. Magnitude of Fourier transformed EXAFS spectra for R-space plots at the (c) Ni K-edge and (d) Pt L_3-edge. All plots show either k-space or R-space fitting windows in gray, which were applied during co-fits of the Ni and Pt edges for each sample.

E-NF has a larger Ni ratio in the near-surface region, Ni will influence the electronic structure of the catalyst surface to a greater degree than in H-NF. It is well known that Pt-Ni alloys have a downshift in the *d*-band center position of the catalyst surface compared to pure Pt, leading to weaker binding with surface adsorbates.[67,83,84] This trend has been shown to induce higher catalytic activity in Pt-Ni alloy ORR catalysts compared to pure Pt.[82] In addition, the extended sheet structure of E-NF is likely to have fewer low-coordinated sites. It was demonstrated by EXAFS that the coordination number of Pt in H-NF is significantly lower on average than E-NF (Table 5.2), indicating that H-NF would have more low-coordinated sites that bind oxygenated adsorbates more strongly during ORR.[108] Since H-NF has a combination of a more Pt-rich surface with more low-coordinated sites than E-NF, it is expected that it will bind ORR-related adsorbates too strongly, resulting in lower intrinsic ORR activity for H-NF.

Table 5.2. EXAFS fitting results for hollow and excavated nanoframes.[a]

	H-NF	**E-NF**
R_{PtNi}	2.63 (1)	2.63 (1)
R_{PtPt}	2.70 (1)	2.71 (1)
R_{NiPt}	2.63 (1)	2.63 (1)
R_{NiNi}	2.61 (1)	2.61 (1)
σ^2_{PtNi}	0.0073 (22)	0.0066 (13)
σ^2_{PtPt}	0.0074 (12)	0.0065 (8)
σ^2_{NiPt}	0.0073 (22)	0.0066 (13)
σ^2_{NiNi}	0.0159 (32)	0.0144 (23)
N_{PtNi}	2.0 (8)	2.7 (6)
N_{PtPt}	7.4 (1.8)	7.9 (1.4)
$N_{Pt,total}$	9.4 (2.6)	10.6 (2.0)
N_{NiPt}	3.0 (1.0)	3.6 (7)
N_{NiNi}	6.9 (1.9)	5.9 (1.2)
$N_{Ni,total}$	9.9 (2.9)	9.5 (1.9)
$\Delta E_{0,Pt}$	5.9 (1.2)	6.8 (8)
$\Delta E_{0,Ni}$	3.2 (1.0)	3.9 (7)
R-factor	0.0095	0.0044
Red. χ^2	298	123
J_{Pt}	64%	73%
J_{Ni}	45%	58%

[a]Values in parentheses are error bars determined from IFEFFIT.

5.5 Morphology of Excavated Nanoframe

As mentioned above, it has been shown in Chapter 4 that in the formation process of Pt-Ni rhombic dodecahedra, a branched nanoparticle forms from the initial nucleated seed. It was also demonstrated that, in order to form the SD precursor to a hollow nanoframe, the Pt that was originally part of the branched seed migrated outward to the edges of the rhombic dodecahedron.[265] Under lower Ni concentration, as is the case for synthesis of E-SD, Pt could be favorably deposited between the

branches such that some Pt will stay inside E-SD even after the formation of Pt-rich exterior edges. After chemical corrosion, the excess Pt that had deposited inside E-SD formed the sheet structure that is bounded by the interior branches and exterior edges in E-NF. The most probable model for E-NF (Fig. 5.9a) was established based on the mechanism of Pt-Ni rhombic dodecahedron formation

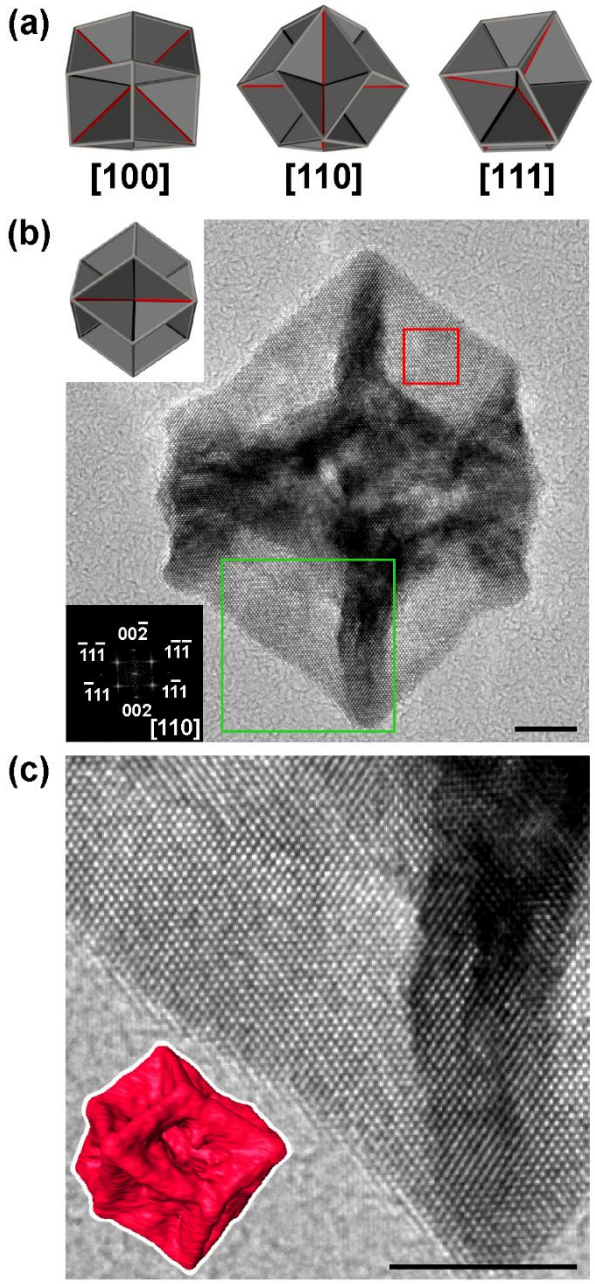


Figure 5.9. Three-dimensional morphology of the excavated nanoframe. (a) The model of the excavated nanoframe shown in three orientations, where red indicates branches of type A and black indicates branches of type B. See Fig. 5.2 for more details. (b) HRTEM image of the excavated nanoframe oriented in <110> direction. The top left inset is the corresponding model of the excavated nanoframe in the identical orientation. The bottom left inset is the FFT of the image in the red box. (c) Magnified HRTEM image of thin sheet in excavated nanoframe from green box in (b), with ET rendering of excavated nanoframe in inset. All scale bars represent 5 nm.

and the TEM and SEM images collected for E-NF. In this model, all inner sheets are perpendicular to the <110> direction and it is therefore expected that the sheets will have {110} surfaces. In order to confirm the model, HRTEM images and electron tomography (ET) of E-NF were collected. Although most 2-D projections of this model contain two overlapping sheets, if the model E-NF is oriented in the <110> direction, a region exists where the electron beam must pass through only one sheet, as shown in Fig. 5.9b. This image corresponds well with the model of E-NF oriented in the same direction (top left inset). The FFT of a single sheet (bottom left inset, taken from portion of image in red box) confirmed that E-NF was oriented in the <110> direction. Fig. 5.9c shows the high crystallinity in the region of a single-sheet and an ET rendering of E-NF, demonstrating the excavation of the rhombic dodecahedron. In summary, these sheet structures were found to remain in the {110} planes extending inward from the edges of the NF after chemical corrosion, suggesting that they are terminated with primarily {110} facets.

5.6 Oxygen Reduction Activity of Excavated Nanoframes

We loaded the three-dimensional nanostructures, either H-NF or E-NF, on carbon support to compare their catalytic performance toward ORR. Fig. 5.10 shows a typical TEM image of H-NF and E-NF deposited on carbon, illustrating that the dispersion of both NFs was uniform over the carbon support. H-NF and E-NF were electrochemically tested using the rotating disk electrode method and benchmarked against a commercial Pt/C catalyst. The CVs in Fig. 5.12a illustrate that both NF catalysts have high SSA. The SSA, measured by the H_{upd} process, was 60.2 m^2/g_{Pt} for H-NF and 48.1 m^2/g_{Pt} for E-NF, which are both slightly less than that of commercial Pt/C (76.1 m^2/g_{Pt}). The SSA of E-NF was lower than that of H-NF due to its interior sheets, making it a quasi-2D structure instead of the quasi-1-D rods of H-NF. Electrooxidation of adsorbed CO (also known as CO-stripping) on H-NF and E-NF provided similar ECSA to H_{upd} such that the ratio $ECSA_{CO}/ECSA_{Hupd}$ was found to be 1.03 for both electrocatalysts (Fig. 5.11). This confirms that the Pt-skin structure does not exist on these nanoframes due to the differences in synthetic method, corrosion to nanoframe, and annealing treatments.[165] However, it is demonstrated below that even without Pt-skin formation, E-NF could achieve extremely high activity.

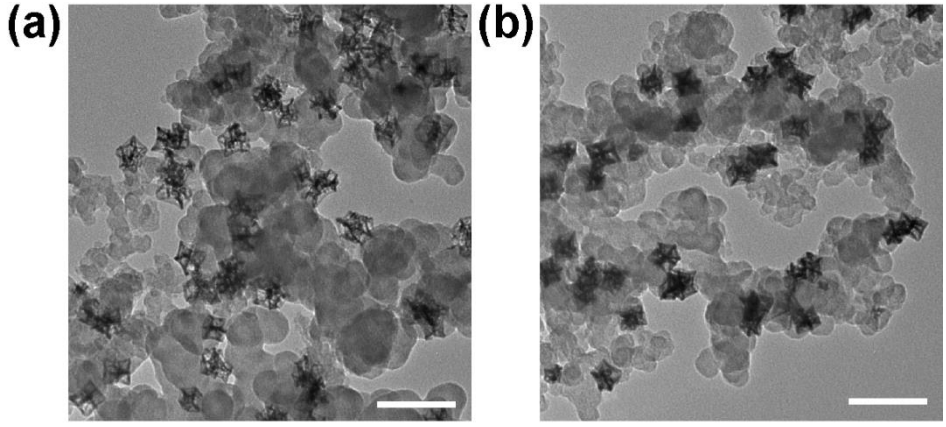


Figure 5.10. TEM of as-loaded nanoframes on carbon support. TEM images of (a) H-NF and (b) E-NF after loading on carbon. Scale bars represent 100 nm.

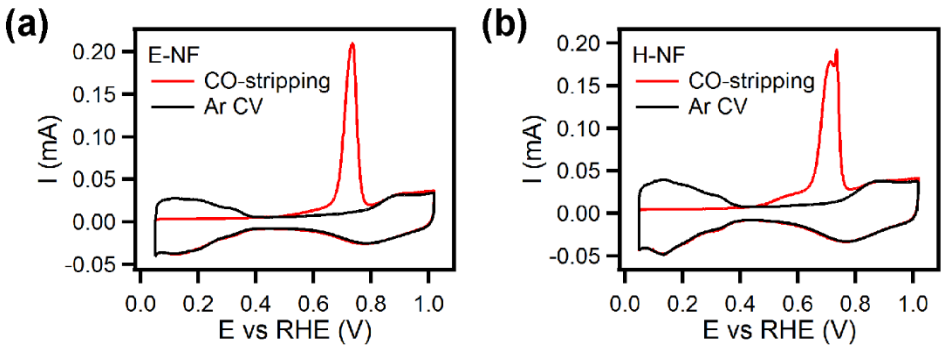


Figure 5.11. Pt-skeleton formation on excavated and hollow nanoframes. Representative CO-stripping and hydrogen underpotential deposition measurements for (a) E-NF and (b) H-NF recorded at room temperature in Ar-saturated 0.1 M $HClO_4$ solution with a sweep rate of 50 mV/s. CO-stripping measurement is recorded after catalyst is poisoned with CO, and excess CO is purged by Ar. Both E-NF and H-NF exhibited ratios of $ECSA_{CO}/ECSA_{Hupd}$ = 1.03, indicating no Pt-skin formation.[165]

A positive shift in the onset of hydroxyl adsorption of ~18 mV occurred for E-NF versus that of H-NF, accompanied by a negative shift in the underpotential deposition of hydrogen. Both of these shifts indicate weaker binding to surface species in the following order: E-NF < H-NF < Pt/C. This result is in agreement with increased near-surface Ni alloying with Pt and fewer low-coordinated sites of the E-NF surface compared to the H-NF surface observed by various methods. The ORR measurement was performed in 0.1 M $HClO_4$ solution saturated with oxygen at a sweep rate of 20 mV/s and a rotation rate of 1600 rpm. As shown in Fig. 5.12b, the ORR polarization curves

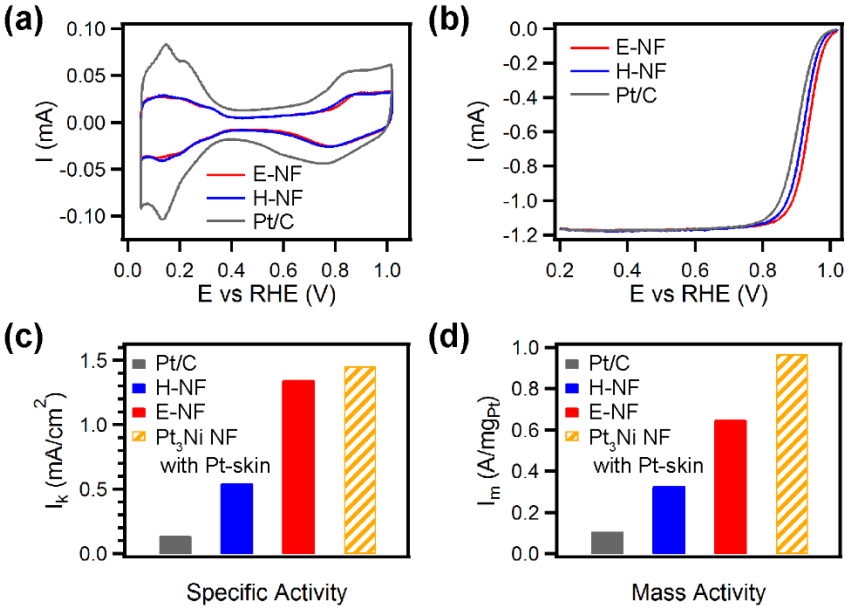


Figure 5.12. Oxygen reduction activity of excavated nanoframes. (a) Cyclic voltammograms recorded at room temperature in Ar-saturated 0.1 M $HClO_4$ solution with a sweep rate of 50 mV/s. All potentials are reported versus RHE. (b) ORR polarization curves recorded at room temperature in O_2-saturated 0.1 M $HClO_4$ solution with a sweep rate of 20 mV/s and a rotation rate of 1600 rpm. (c) Specific activity and (d) mass activity at 0.95 V vs RHE for Pt/C, H-NF, and E-NF as compared to Pt_3Ni NFs with Pt-skin.[187]

demonstrate an increase in activity along the following trend: Pt/C < H-NF < E-NF. The calculated kinetic current density at 0.95 V vs RHE was normalized over the ECSA determined by H_{upd} and Pt mass loading to give the specific activity and mass activity, respectively, and compared to the earlier study of Pt_3Ni NF with Pt-skin (Fig. 5.12c,d). Of the catalysts studied in this work, E-NF exhibits the highest specific and mass activity, ~10 and 6 times higher than that of commercial Pt/C, respectively. E-NF shows specific activity of 1.35 mA/cm^2, a 145% specific activity enhancement compared with H-NF (0.55 mA/cm^2). The enhanced electrocatalytic performance of E-NF is attributed to its extended surface facets which are more enriched in Ni and have fewer low-coordinated sites than the surface of H-NF. While the quasi-2-D structure of E-NF does lower its SSA, the thin nature of the sheets in E-NF allows it to maintain high mass activity, approximately twice that of H-NF. This emphasizes the importance of control of the three-dimensional elemental distribution in alloy nanocrystals to the design of ORR catalysts with new morphologies that enhance activity. If Pt-skin can be achieved on this quasi-2-D structure, the activity could be dramatically increased.

5.7 Conclusions

In conclusion, the three-dimensional elemental distribution within Pt-Ni rhombic dodecahedra was successfully controlled, leading to structural differentiation after Ni corrosion into either hollow or excavated NFs. The excavated NF exhibited interior Pt-rich sheets extending from outer Pt-rich edges to inner Pt-rich branches, whereas the hollow NF had empty space inside Pt-rich edges. These differences resulted in dramatic ORR activity improvement for the excavated NF. This work revealed the clear relationship between structural properties and electrochemical performance, such as the importance of the Ni content in the near-surface region and the extended sheet structure. These design strategies can be implemented in various bimetallic nanocrystal catalysts for electrochemical or other catalytic applications.

6. Concluding Remarks

Following the discovery of Pt_3Ni nanoframes that are highly active for the oxygen reduction reaction, the synthetic concept was applied to other systems such as Pt-Co polyhedral nanoparticles that also evolved into nanoframes. This work provided insight into the complexities of attaining uniformly-shaped polyhedra with segregation of Pt to their edges and the special qualities of the Pt-Ni alloy system. The exploration of the Pt-Co system exposed the lack of understanding of the Pt-Ni rhombic dodecahedral system that needed to be fulfilled before new compositions and morphologies of nanoframes could be perfected. Fundamental studies of the Pt-Ni system were undertaken to understand the origin of the high activity for ORR of the Pt_3Ni nanoframe and the synthetic mechanisms behind the formation of the Pt-Ni rhombic dodecahedra.

X-ray absorption spectroscopy provided sensitivity to the atomic coordination of Pt and Ni within the ultrathin edges of the nanoframe. The technique was applied *in situ* to probe the catalyst structure as it performed the oxygen reduction. It was determined that the best nanoframe samples had the highly-desired Pt-skin structure that produced their high activity. However, samples with significantly lower activity were determined to be lacking the Pt-skin structure. The broad spectrum of nanoframe quality revealed the need for further investigation into the mechanisms behind Pt-Ni rhombic dodecahedra synthesis. If the mechanism of Pt-enrichment at the edges of the Pt-Ni rhombic dodecahedra could be elucidated, then it was possible that the consistency of nanoframe synthesis could be improved.

The mechanism of rhombic dodecahedra synthesis was explored via quasi-*in situ* sampling of the synthetic process at lower temperature, in order to draw out the synthesis to longer times. In this way, discrete stages of the dodecahedron formation process could be characterized with multiple techniques. A compositional oscillation was observed in which the initial seed nanoparticles were Pt-rich and grew into anisotropic branch structures, which had step sites between them that catalyzed Ni deposition, causing the composition to become Ni-rich. The rhombic dodecahedron was formed, at which point Pt migrated from the interior axes of the particle to the exterior edges, forming the Pt-rich framework. The understanding of this complex synthetic mechanism led to new ideas for tuning the structure of the nanoframe.

By altering the nanoframe growth conditions to incorporate less Ni in the synthesis, Pt deposition could be accelerated on the branched seeds that form initially. Pt localization between the branches was observed, such that the Pt did not fully migrate to the exterior edges. When the Ni was corroded, a network of two-dimensional sheets remained inside the nanoframe, contrary to the previous hollow morphology; the new nanoframe was termed an excavated nanoframe. The extended surfaces of these sheets had fewer low-coordinated sites that bind oxygenated adsorbates too strongly during the ORR. Therefore, the surface of the excavated nanoframe was highly active for the ORR.

The intersection of chemical, physical, and material sciences enabled the thorough exploration of highly active ORR catalysts in this dissertation. Fundamental understanding and application of the synthesis, electron and X-ray characterization techniques, and surface science studies can lead to truly magnificent understanding of a nanomaterial. By pushing forward the frontiers of nanomaterial characterization techniques and nanomaterial design concepts, new complexities that were previously unimaginable can be introduced. In-depth exploration of next-generation nanomaterials will continue to lead to novel properties and applications that can positively influence society, especially in the energy and sustainability sector. These efforts will be critical to the quality of life of future generations, and it is hoped that this dissertation can contribute in some small way to the fundamental understanding of materials solutions to the challenges scientists face.

References

1. Dresselhaus M, Thomas I. Alternative energy technologies. *Nature* 2001, **414**(6861)**:** 332-337.

2. Lewis NS, Nocera DG. Powering the planet: Chemical challenges in solar energy utilization. *Proceedings of the National Academy of Sciences of the United States of America* 2006, **103**(43)**:** 15729-15735.

3. Seh ZW, Kibsgaard J, Dickens CF, Chorkendorff I, Norskov JK, Jaramillo TF. Combining theory and experiment in electrocatalysis: Insights into materials design. *Science* 2017, **355**(6321)**:** 146-+.

4. Tans P, Keeling R. Trends in Atmospheric Carbon Dioxide.

5. Keeling CD, Whorf TP, Wahlen M, van der Plicht J. Interannual extremes in the rate of rise of atmospheric carbon dioxide since 1980. *Nature* 1995, **375**(6533)**:** 666.

6. Petit J-R, Jouzel J, Raynaud D, Barkov NI, Barnola J-M, Basile I*, et al.* Climate and atmospheric history of the past 420,000 years from the Vostok ice core, Antarctica. *Nature* 1999, **399**(6735)**:** 429-436.

7. Oda T, Maksyutov S. A very high-resolution (1 km× 1 km) global fossil fuel CO 2 emission inventory derived using a point source database and satellite observations of nighttime lights. *Atmospheric Chemistry and Physics* 2011, **11**(2)**:** 543-556.

8. Cox PM, Betts RA, Jones CD, Spall SA, Totterdell IJ. Acceleration of global warming due to carbon-cycle feedbacks in a coupled climate model. *Nature* 2000, **408**(6809)**:** 184-187.

9. Hoegh-Guldberg O, Mumby PJ, Hooten AJ, Steneck RS, Greenfield P, Gomez E*, et al.* Coral reefs under rapid climate change and ocean acidification. *Science* 2007, **318**(5857)**:** 1737-1742.

10. Hughes TP, Kerry JT, Álvarez-Noriega M, Álvarez-Romero JG, Anderson KD, Baird AH*, et al.* Global warming and recurrent mass bleaching of corals. *Nature* 2017, **543**(7645)**:** 373-377.

11. Parmesan C, Yohe G. A globally coherent fingerprint of climate change impacts across natural systems. *Nature* 2003, **421**(6918)**:** 37-42.

12. Parmesan C. Ecological and evolutionary responses to recent climate change. *Annu Rev Ecol Evol Syst* 2006, **37:** 637-669.

13. Hoffmann AA, Sgrò CM. Climate change and evolutionary adaptation. *Nature* 2011, **470**(7335)**:** 479-485.

14. Kim D, Sakimoto KK, Hong D, Yang P. Artificial Photosynthesis for Sustainable Fuel and Chemical Production. *Angewandte Chemie International Edition* 2015.

15. Berner RA. The long-term carbon cycle, fossil fuels and atmospheric composition. *Nature* 2003, **426**(6964)**:** 323-326.

16. Sabine CL, Feely RA, Gruber N, Key RM, Lee K, Bullister JL*, et al.* The oceanic sink for anthropogenic CO2. *Science* 2004, **305**(5682)**:** 367-371.

17. Archer D. Carbon cycle: Checking the thermostat. *Nature Geoscience* 2008, **1**(5)**:** 289-290.

18. Le Quéré C, Raupach MR, Canadell JG, Marland G, Bopp L, Ciais P*, et al.* Trends in the sources and sinks of carbon dioxide. *Nature Geoscience* 2009, **2**(12)**:** 831-836.

19. Lacis AA, Schmidt GA, Rind D, Ruedy RA. Atmospheric CO2: Principal control knob governing Earth's temperature. *Science* 2010, **330**(6002)**:** 356-359.

20. Wagner FT, Lakshmanan B, Mathias MF. Electrochemistry and the future of the automobile. *J Phys Chem Lett* 2010, **1**(14)**:** 2204-2219.

21. Borup R, Meyers J, Pivovar B, Kim YS, Mukundan R, Garland N*, et al.* Scientific aspects of polymer electrolyte fuel cell durability and degradation. *Chem Rev* 2007, **107**(10)**:** 3904-3951.

22. Gasteiger HA, Marković NM. Just a Dream—or Future Reality? *Science* 2009, **324**(5923)**:** 48-49.

23. Debe MK. Electrocatalyst approaches and challenges for automotive fuel cells. *Nature* 2012, **486**(7401)**:** 43-51.

24. Nørskov JK, Rossmeisl J, Logadottir A, Lindqvist L, Kitchin JR, Bligaard T*, et al.* Origin of the overpotential for oxygen reduction at a fuel-cell cathode. *Journal of Physical Chemistry B* 2004, **108**(46)**:** 17886-17892.

25. Climent V, Marković N, Ross P. Kinetics of Oxygen Reduction on an Epitaxial Film of Palladium on Pt (111)†. *The Journal of Physical Chemistry B* 2000, **104**(14)**:** 3116-3120.

26. Xiao L, Zhuang L, Liu Y, Lu J. Activating Pd by morphology tailoring for oxygen reduction. *Journal of the American Chemical Society* 2008, **131**(2)**:** 602-608.

27. Antolini E. Palladium in fuel cell catalysis. *Energy & Environmental Science* 2009, **2**(9)**:** 915-931.

28. Bashyam R, Zelenay P. A class of non-precious metal composite catalysts for fuel cells. *Nature* 2006, **443**(7107)**:** 63-66.

29. Wu G, More KL, Johnston CM, Zelenay P. High-performance electrocatalysts for oxygen reduction derived from polyaniline, iron, and cobalt. *Science* 2011, **332**(6028)**:** 443-447.

30. Lefèvre M, Proietti E, Jaouen F, Dodelet J-P. Iron-based catalysts with improved oxygen reduction activity in polymer electrolyte fuel cells. *Science* 2009, **324**(5923)**:** 71-74.

31. Chen Z, Higgins D, Yu A, Zhang L, Zhang J. A review on non-precious metal electrocatalysts for PEM fuel cells. *Energy & Environmental Science* 2011, **4**(9)**:** 3167-3192.

32. Qu L, Liu Y, Baek J-B, Dai L. Nitrogen-doped graphene as efficient metal-free electrocatalyst for oxygen reduction in fuel cells. *ACS nano* 2010, **4**(3)**:** 1321-1326.

33. Sheng Z-H, Shao L, Chen J-J, Bao W-J, Wang F-B, Xia X-H. Catalyst-free synthesis of nitrogen-doped graphene via thermal annealing graphite oxide with melamine and its excellent electrocatalysis. *ACS nano* 2011, **5**(6)**:** 4350-4358.

34. Li Y, Zhou W, Wang H, Xie L, Liang Y, Wei F*, et al.* An oxygen reduction electrocatalyst based on carbon nanotube-graphene complexes. *Nature nanotechnology* 2012, **7**(6)**:** 394-400.

35. Wang H, Maiyalagan T, Wang X. Review on recent progress in nitrogen-doped graphene: synthesis, characterization, and its potential applications. *Acs Catalysis* 2012, **2**(5)**:** 781-794.

36. Dai L, Xue Y, Qu L, Choi H-J, Baek J-B. Metal-free catalysts for oxygen reduction reaction. *Chemical reviews* 2015, **115**(11)**:** 4823-4892.

37. Liang YY, Li YG, Wang HL, Zhou JG, Wang J, Regier T*, et al.* Co3O4 nanocrystals on graphene as a synergistic catalyst for oxygen reduction reaction. *Nature Materials* 2011, **10**(10)**:** 780-786.

38. Wu Z-S, Yang S, Sun Y, Parvez K, Feng X, Müllen K. 3D nitrogen-doped graphene aerogel-supported Fe3O4 nanoparticles as efficient electrocatalysts for the oxygen reduction reaction. *Journal of the American Chemical Society* 2012, **134**(22)**:** 9082-9085.

39. Guo D, Shibuya R, Akiba C, Saji S, Kondo T, Nakamura J. Active sites of nitrogen-doped carbon materials for oxygen reduction reaction clarified using model catalysts. *Science* 2016, **351**(6271)**:** 361-365.

40. Bard AJ, Faulkner LR. *Electrochemical methods: fundamentals and applications*, vol. 2. Wiley New York, 1980.

41. Markovic NM, Gasteiger HA, Ross Jr PN. Oxygen reduction on platinum low-index single-crystal surfaces in sulfuric acid solution: rotating ring-Pt (hkl) disk studies. *The Journal of Physical Chemistry* 1995, **99**(11)**:** 3411-3415.

42. Markovic NM, Gasteiger HA, Ross PN. Oxygen reduction on platinum low-index single-crystal surfaces in alkaline solution: rotating ring diskPt (hkl) studies. *The Journal of Physical Chemistry* 1996, **100**(16)**:** 6715-6721.

43. Markovic N, Gasteiger H, Ross PN. Kinetics of oxygen reduction on Pt (hkl) electrodes: implications for the crystallite size effect with supported Pt electrocatalysts. *Journal of the Electrochemical Society* 1997, **144**(5)**:** 1591-1597.

44. Markovic NM, Schmidt TJ, Stamenkovic V, Ross PN. Oxygen Reduction Reaction on Pt and Pt Bimetallic Surfaces: A Selective Review. *Fuel Cells* 2001, **1**(2)**:** 105-116.

45. Snyder J, Danilovic N, Paulikas AP, Tripkovic D, Strmcnik D, Markovic NM*, et al.* Thin Film Approach to Single Crystalline Electrochemistry. *The Journal of Physical Chemistry C* 2013, **117**(45)**:** 23790-23796.

46. Paulus U, Schmidt T, Gasteiger H, Behm R. Oxygen reduction on a high-surface area Pt/Vulcan carbon catalyst: a thin-film rotating ring-disk electrode study. *Journal of Electroanalytical Chemistry* 2001, **495**(2)**:** 134-145.

47. Wang J, Markovic N, Adzic R. Kinetic analysis of oxygen reduction on Pt (111) in acid solutions: intrinsic kinetic parameters and anion adsorption effects. *The Journal of Physical Chemistry B* 2004, **108**(13)**:** 4127-4133.

48. Antolini E. Carbon supports for low-temperature fuel cell catalysts. *Applied Catalysis B: Environmental* 2009, **88**(1)**:** 1-24.

49. Zhou Y, Neyerlin K, Olson TS, Pylypenko S, Bult J, Dinh HN*, et al.* Enhancement of Pt and Pt-alloy fuel cell catalyst activity and durability via nitrogen-modified carbon supports. *Energy & Environmental Science* 2010, **3**(10)**:** 1437-1446.

50. Schmidt TJ, Gasteiger HA, Stab GD, Urban PM, Kolb DM, Behm RJ. Characterization of high-surface area electrocatalysts using a rotating disk electrode configuration. *Journal of the Electrochemical Society* 1998, **145**(7)**:** 2354-2358.

51. Mayrhofer KJJ, Strmcnik D, Blizanac BB, Stamenkovic V, Arenz M, Markovic NM. Measurement of oxygen reduction activities via the rotating disc electrode method: From Pt model surfaces to carbon-supported high surface area catalysts. *Electrochimica Acta* 2008, **53**(7)**:** 3181-3188.

52. Subbaraman R, Strmcnik D, Stamenkovic V, Markovic NM. Three phase interfaces at electrified metal− solid electrolyte systems 1. Study of the Pt (hkl)− Nafion interface. *The Journal of Physical Chemistry C* 2010, **114**(18)**:** 8414-8422.

53. Garsany Y, Singer IL, Swider-Lyons KE. Impact of film drying procedures on RDE characterization of Pt/VC electrocatalysts. *Journal of electroanalytical chemistry* 2011, **662**(2)**:** 396-406.

54. Shinozaki K, Zack JW, Pylypenko S, Pivovar BS, Kocha SS. Oxygen reduction reaction measurements on platinum electrocatalysts utilizing rotating disk electrode technique II. Influence of ink formulation, catalyst layer uniformity and thickness. *Journal of The Electrochemical Society* 2015, **162**(12)**:** F1384-F1396.

55. van der Vliet D, Strmcnik DS, Wang C, Stamenkovic VR, Markovic NM, Koper MTM. On the importance of correcting for the uncompensated Ohmic resistance in model experiments of the Oxygen Reduction Reaction. *Journal of Electroanalytical Chemistry* 2010, **647**(1)**:** 29-34.

56. Garsany Y, Baturina OA, Swider-Lyons KE, Kocha SS. Experimental methods for quantifying the activity of platinum electrocatalysts for the oxygen reduction reaction. *Analytical chemistry* 2010, **82**(15)**:** 6321-6328.

57. Shinozaki K, Zack JW, Richards RM, Pivovar BS, Kocha SS. Oxygen Reduction Reaction Measurements on Platinum Electrocatalysts Utilizing Rotating Disk Electrode Technique I. Impact of Impurities, Measurement Protocols and Applied Corrections. *Journal of The Electrochemical Society* 2015, **162**(10)**:** F1144-F1158.

58. Garsany Y, Ge J, St-Pierre J, Rocheleau R, Swider-Lyons K. Standardizing thin-film rotating disk electrode measurements of the oxygen reduction activity of Pt/C. *ECS Transactions* 2013, **58**(1)**:** 3-14.

59. Garsany Y, Ge J, St-Pierre J, Rocheleau R, Swider-Lyons KE. Analytical procedure for accurate comparison of rotating disk electrode results for the oxygen reduction activity of Pt/C. *Journal of The Electrochemical Society* 2014, **161**(5)**:** F628-F640.

60. Lopes PP, Strmcnik D, Tripkovic D, Connell JG, Stamenkovic V, Markovic NM. Relationships between atomic level surface structure and stability/activity of platinum surface atoms in aqueous environments. *ACS Catalysis* 2016, **6**(4)**:** 2536-2544.

61. Mukerjee S, Srinivasan S. Enhanced electrocatalysis of oxygen reduction on platinum alloys in proton exchange membrane fuel cells. *Journal of Electroanalytical Chemistry* 1993, **357**(1-2)**:** 201-224.

62. Mukerjee S, Srinivasan S, Soriaga MP, McBreen J. Role of structural and electronic-properties of pt and pt alloys on electrocatalysis of oxygen reduction - an in-situ xanes and exafs investigation. *Journal of the Electrochemical Society* 1995, **142**(5)**:** 1409-1422.

63. Mukerjee S, Srinivasan S, Soriaga MP, McBreen J. Effect of preparation conditions of pt alloys on their electronic, structural, and electrocatalytic activities for oxygen reduction-xrd, xas, and electrochemical studies. *Journal of Physical Chemistry* 1995, **99**(13)**:** 4577-4589.

64. Toda T, Igarashi H, Uchida H, Watanabe M. Enhancement of the electroreduction of oxygen on Pt alloys with Fe, Ni, and Co. *Journal of the Electrochemical Society* 1999, **146**(10)**:** 3750-3756.

65. Toda T, Igarashi H, Watanabe M. Enhancement of the electrocatalytic O-2 reduction on Pt-Fe alloys. *Journal of Electroanalytical Chemistry* 1999, **460**(1-2)**:** 258-262.

66. Stamenkovic VR, Mun BS, Mayrhofer KJJ, Ross PN, Markovic NM. Effect of surface composition on electronic structure, stability, and electrocatalytic properties of Pt-transition metal alloys: Pt-skin versus Pt-skeleton surfaces. *Journal of the American Chemical Society* 2006, **128**(27)**:** 8813-8819.

67. Kitchin JR, Nørskov JK, Barteau MA, Chen JG. Modification of the surface electronic and chemical properties of Pt(111) by subsurface 3d transition metals. *Journal of Chemical Physics* 2004, **120**(21)**:** 10240-10246.

68. Watanabe M, Tryk DA, Wakisaka M, Yano H, Uchida H. Overview of recent developments in oxygen reduction electrocatalysis. *Electrochimica Acta* 2012, **84:** 187-201.

69. Paulus UA, Wokaun A, Scherer GG, Schmidt TJ, Stamenkovic V, Markovic NM*, et al.* Oxygen reduction on high surface area Pt-based alloy catalysts in comparison to well defined smooth bulk alloy electrodes. *Electrochimica Acta* 2002, **47**(22-23)**:** 3787-3798.

70. Hammer B, Nørskov JK. Theoretical surface science and catalysis - Calculations and concepts. *Advances in Catalysis, Vol 45: Impact of Surface Science on Catalysis* 2000, **45:** 71-129.

71. Nørskov JK, Abild-Pedersen F, Studt F, Bligaard T. Density functional theory in surface chemistry and catalysis. *Proceedings of the National Academy of Sciences of the United States of America* 2011, **108**(3)**:** 937-943.

72. Hammer B, Nørskov J. Why gold is the noblest of all the metals. *Nature* 1995, **376**(6537)**:** 238-240.

73. Nilsson A, Pettersson L, Hammer B, Bligaard T, Christensen CH, Nørskov JK. The electronic structure effect in heterogeneous catalysis. *Catalysis letters* 2005, **100**(3-4)**:** 111-114.

74. Ruban A, Hammer B, Stoltze P, Skriver HL, Nørskov JK. Surface electronic structure and reactivity of transition and noble metals. *Journal of Molecular Catalysis A: Chemical* 1997, **115**(3)**:** 421-429.

75. Nørskov JK, Bligaard T, Logadottir A, Bahn S, Hansen LB, Bollinger M*, et al.* Universality in heterogeneous catalysis. *Journal of Catalysis* 2002, **209**(2)**:** 275-278.

76. Greeley J, Stephens I, Bondarenko A, Johansson TP, Hansen HA, Jaramillo T*, et al.* Alloys of platinum and early transition metals as oxygen reduction electrocatalysts. *Nature chemistry* 2009, **1**(7)**:** 552-556.

77. Viswanathan V, Hansen HA, Rossmeisl J, Nørskov JK. Universality in oxygen reduction electrocatalysis on metal surfaces. *ACS Catalysis* 2012, **2**(8)**:** 1654-1660.

78. Bligaard T, Nørskov JK, Dahl S, Matthiesen J, Christensen CH, Sehested J. The Bronsted-Evans-Polanyi relation and the volcano curve in heterogeneous catalysis. *Journal of Catalysis* 2004, **224**(1)**:** 206-217.

79. Medford AJ, Vojvodic A, Hummelshøj JS, Voss J, Abild-Pedersen F, Studt F*, et al.* From the Sabatier principle to a predictive theory of transition-metal heterogeneous catalysis. *Journal of Catalysis* 2015, **328:** 36-42.

80. Greeley J, Mavrikakis M. Alloy catalysts designed from first principles. *Nature materials* 2004, **3**(11)**:** 810-815.

81. Mun BS, Watanabe M, Rossi M, Stamenkovic V, Markovic NM, Ross PN. A study of electronic structures of Pt3M (M=Ti,V,Cr,Fe,Co,Ni) polycrystalline alloys with valence-band photoemission spectroscopy. *Journal of Chemical Physics* 2005, **123**(20)**:** 4.

82. Stamenkovic VR, Fowler B, Mun BS, Wang GF, Ross PN, Lucas CA*, et al.* Improved oxygen reduction activity on Pt3Ni(111) via increased surface site availability. *Science* 2007, **315**(5811)**:** 493-497.

83. Stamenkovic VR, Mun BS, Arenz M, Mayrhofer KJJ, Lucas CA, Wang GF*, et al.* Trends in electrocatalysis on extended and nanoscale Pt-bimetallic alloy surfaces. *Nature Materials* 2007, **6**(3)**:** 241-247.

84. Stamenkovic V, Mun BS, Mayrhofer KJJ, Ross PN, Markovic NM, Rossmeisl J*, et al.* Changing the activity of electrocatalysts for oxygen reduction by tuning the surface electronic structure. *Angewandte Chemie-International Edition* 2006, **45**(18)**:** 2897-2901.

85. Stephens IE, Bondarenko AS, Perez-Alonso FJ, Calle-Vallejo F, Bech L, Johansson TP*, et al.* Tuning the activity of Pt(111) for oxygen electroreduction by subsurface alloying. *J Am Chem Soc* 2011, **133**(14)**:** 5485-5491.

86. Paulus UA, Wokaun A, Scherer GG, Schmidt TJ, Stamenkovic V, Radmilovic V*, et al.* Oxygen reduction on carbon-supported Pt-Ni and Pt-Co alloy catalysts. *Journal of Physical Chemistry B* 2002, **106**(16)**:** 4181-4191.

87. Stamenkovic V, Schmidt TJ, Ross PN, Markovic NM. Surface composition effects in electrocatalysis: Kinetics of oxygen reduction on well-defined Pt3Ni and Pt3Co alloy surfaces. *Journal of Physical Chemistry B* 2002, **106**(46)**:** 11970-11979.

88. Stamenkovic V, Schmidt TJ, Ross PN, Markovic NM. Surface segregation effects in electrocatalysis: kinetics of oxygen reduction reaction on polycrystalline Pt3Ni alloy surfaces. *Journal of Electroanalytical Chemistry* 2003, **554:** 191-199.

89. Gauthier Y, Joly Y, Baudoing R, Rundgren J. Surface-sandwich segregation on nondilute bimetallic alloys: Pt 50 Ni 50 and Pt 78 Ni 22 probed by low-energy electron diffraction. *Physical Review B* 1985, **31**(10)**:** 6216.

90. Abrikosov I, Ruban A, Skriver HL, Johansson B. Calculated orientation dependence of surface segregations in Pt 50 Ni 50. *Physical Review B* 1994, **50**(3)**:** 2039.

91. Vitos L, Ruban A, Skriver HL, Kollar J. The surface energy of metals. *Surface Science* 1998, **411**(1)**:** 186-202.

92. Ruban AV, Skriver HL, Nørskov JK. Surface segregation energies in transition-metal alloys. *Physical Review B* 1999, **59**(24)**:** 15990-16000.

93. Wang GF, Van Hove MA, Ross PN, Baskes MI. Monte Carlo simulations of segregation in Pt-Ni catalyst nanoparticles. *Journal of Chemical Physics* 2005, **122**(2).

94. Xu Y, Ruban AV, Mavrikakis M. Adsorption and dissociation of O-2 on Pt-Co and Pt-Fe alloys. *Journal of the American Chemical Society* 2004, **126**(14)**:** 4717-4725.

95. Greeley J, Nørskov JK. Combinatorial density functional theory-based screening of surface alloys for the oxygen reduction reaction. *The Journal of Physical Chemistry C* 2009, **113**(12)**:** 4932-4939.

96. Stephens IE, Bondarenko AS, Grønbjerg U, Rossmeisl J, Chorkendorff I. Understanding the electrocatalysis of oxygen reduction on platinum and its alloys. *Energy & Environmental Science* 2012, **5**(5)**:** 6744-6762.

97. Hernandez-Fernandez P, Masini F, McCarthy DN, Strebel CE, Friebel D, Deiana D*, et al.* Mass-selected nanoparticles of PtxY as model catalysts for oxygen electroreduction. *Nature Chemistry* 2014, **6**(8)**:** 732-738.

98. Johansson TP, Ulrikkeholm ET, Hernandez-Fernandez P, Malacrida P, Hansen HA, Bandarenka A*, et al.* Pt Skin Versus Pt Skeleton Structures of Pt3Sc as Electrocatalysts for Oxygen Reduction. *Topics in Catalysis* 2014, **57**(1-4)**:** 245-254.

99. Escudero-Escribano M, Malacrida P, Hansen MH, Vej-Hansen UG, Velázquez-Palenzuela A, Tripkovic V*, et al.* Tuning the activity of Pt alloy electrocatalysts by means of the lanthanide contraction. *Science* 2016, **352**(6281)**:** 73-76.

100. Mavrikakis M, Hammer B, Nørskov JK. Effect of strain on the reactivity of metal surfaces. *Physical Review Letters* 1998, **81**(13)**:** 2819-2822.

101. Strmcnik DS, Rebec P, Gaberscek M, Tripkovic D, Stamenkovic V, Lucas C*, et al.* Relationship between the surface coverage of spectator species and the rate of electrocatalytic reactions. *Journal of Physical Chemistry C* 2007, **111**(50)**:** 18672-18678.

102. Casalongue HS, Kaya S, Viswanathan V, Miller DJ, Friebel D, Hansen HA*, et al.* Direct observation of the oxygenated species during oxygen reduction on a platinum fuel cell cathode. *Nature communications* 2013, **4**.

103. Somorjai GA, Li Y. *Introduction to surface chemistry and catalysis*. John Wiley & Sons, 2010.

104. Mayrhofer KJJ, Blizanac BB, Arenz M, Stamenkovic VR, Ross PN, Markovic NM. The impact of geometric and surface electronic properties of Pt-catalysts on the particle size effect in electocatalysis. *Journal of Physical Chemistry B* 2005, **109**(30)**:** 14433-14440.

105. Nesselberger M, Ashton S, Meier JC, Katsounaros I, Mayrhofer KJ, Arenz M. The particle size effect on the oxygen reduction reaction activity of Pt catalysts: influence of electrolyte and relation to single crystal models. *Journal of the American Chemical Society* 2011, **133**(43)**:** 17428-17433.

106. Greeley J, Rossmeisl J, Hellmann A, Nørskov J. Theoretical trends in particle size effects for the oxygen reduction reaction. *Zeitschrift für Physikalische Chemie* 2007, **221**(9-10)**:** 1209-1220.

107. Shao M, Peles A, Shoemaker K. Electrocatalysis on platinum nanoparticles: particle size effect on oxygen reduction reaction activity. *Nano letters* 2011, **11**(9)**:** 3714-3719.

108. Wang C, van der Vilet D, Chang KC, You HD, Strmcnik D, Schlueter JA*, et al.* Monodisperse Pt3Co Nanoparticles as a Catalyst for the Oxygen Reduction Reaction: Size-Dependent Activity. *Journal of Physical Chemistry C* 2009, **113**(45)**:** 19365-19368.

109. Zhang JL, Vukmirovic MB, Xu Y, Mavrikakis M, Adzic RR. Controlling the catalytic activity of platinum-monolayer electrocatalysts for oxygen reduction with different substrates. *Angewandte Chemie-International Edition* 2005, **44**(14)**:** 2132-2135.

110. Adzic RR, Zhang J, Sasaki K, Vukmirovic MB, Shao M, Wang J*, et al.* Platinum monolayer fuel cell electrocatalysts. *Topics in Catalysis* 2007, **46**(3-4)**:** 249-262.

111. Sasaki K, Naohara H, Cai Y, Choi YM, Liu P, Vukmirovic MB*, et al.* Core-Protected Platinum Monolayer Shell High-Stability Electrocatalysts for Fuel-Cell Cathodes. *Angewandte Chemie International Edition* 2010, **49**(46)**:** 8602-8607.

112. Wang JX, Inada H, Wu LJ, Zhu YM, Choi YM, Liu P*, et al.* Oxygen Reduction on Well-Defined Core-Shell Nanocatalysts: Particle Size, Facet, and Pt Shell Thickness Effects. *Journal of the American Chemical Society* 2009, **131**(47)**:** 17298-17302.

113. Zhang H, Jin M, Xia Y. Enhancing the catalytic and electrocatalytic properties of Pt-based catalysts by forming bimetallic nanocrystals with Pd. *Chemical Society Reviews* 2012, **41**(24)**:** 8035-8049.

114. Xie S, Choi S-I, Lu N, Roling LT, Herron JA, Zhang L*, et al.* Atomic Layer-by-Layer Deposition of Pt on Pd Nanocubes for Catalysts with Enhanced Activity and Durability toward Oxygen Reduction. *Nano letters* 2014, **14**(6)**:** 3570-3576.

115. Park J, Zhang L, Choi S-I, Roling LT, Lu N, Herron JA*, et al.* Atomic Layer-by-Layer Deposition of Platinum on Palladium Octahedra for Enhanced Catalysts toward the Oxygen Reduction Reaction. *ACS nano* 2015, **9**(3)**:** 2635-2647.

116. He DS, He D, Wang J, Lin Y, Yin P, Hong X*, et al.* Ultrathin icosahedral Pt-enriched nanocage with excellent oxygen reduction reaction activity. *Journal of the American Chemical Society* 2016, **138**(5)**:** 1494-1497.

117. Zhang L, Roling LT, Wang X, Vara M, Chi M, Liu J*, et al.* Platinum-based nanocages with subnanometer-thick walls and well-defined, controllable facets. *Science* 2015, **349**(6246)**:** 412-416.

118. Wang X, Figueroa-Cosme L, Yang X, Luo M, Liu J, Xie Z-x*, et al.* Pt-Based Icosahedral Nanocages: Using a Combination of {111} Facets, Twin Defects, and Ultrathin Walls to Greatly Enhance Their Activity toward Oxygen Reduction. *Nano letters* 2016.

119. Lim B, Jiang M, Camargo PH, Cho EC, Tao J, Lu X*, et al.* Pd-Pt bimetallic nanodendrites with high activity for oxygen reduction. *Science* 2009, **324**(5932)**:** 1302-1305.

120. Peng Z, Yang H. Synthesis and oxygen reduction electrocatalytic property of Pt-on-Pd bimetallic heteronanostructures. *Journal of the American Chemical Society* 2009, **131**(22)**:** 7542-7543.

121. Koh S, Strasser P. Electrocatalysis on bimetallic surfaces: modifying catalytic reactivity for oxygen reduction by voltammetric surface dealloying. *Journal of the American Chemical Society* 2007, **129**(42)**:** 12624-12625.

122. Srivastava R, Mani P, Hahn N, Strasser P. Efficient oxygen reduction fuel cell electrocatalysis on voltammetrically dealloyed Pt–Cu–Co nanoparticles. *Angewandte Chemie International Edition* 2007, **46**(47)**:** 8988-8991.

123. Mani P, Srivastava R, Strasser P. Dealloyed Pt− Cu core− shell nanoparticle electrocatalysts for use in PEM fuel cell cathodes. *The Journal of Physical Chemistry C* 2008, **112**(7)**:** 2770-2778.

124. Strasser P, Koh S, Anniyev T, Greeley J, More K, Yu CF*, et al.* Lattice-strain control of the activity in dealloyed core-shell fuel cell catalysts. *Nature Chemistry* 2010, **2**(6)**:** 454-460.

125. Wang DL, Xin HLL, Hovden R, Wang HS, Yu YC, Muller DA*, et al.* Structurally ordered intermetallic platinum-cobalt core-shell nanoparticles with enhanced activity and stability as oxygen reduction electrocatalysts. *Nature Materials* 2013, **12**(1)**:** 81-87.

126. Yan Y, Du JS, Gilroy KD, Yang D, Xia Y, Zhang H. Intermetallic Nanocrystals: Syntheses and Catalytic Applications. *Advanced Materials* 2017.

127. Chung DY, Jun SW, Yoon G, Kwon SG, Shin DY, Seo P*, et al.* Highly Durable and Active PtFe Nanocatalyst for Electrochemical Oxygen Reduction Reaction. *Journal of the American Chemical Society* 2015.

128. Wang C, van der Vliet D, More KL, Zaluzec NJ, Peng S, Sun S*, et al.* Multimetallic Au/FePt3 nanoparticles as highly durable electrocatalyst. *Nano Lett* 2011, **11**(3)**:** 919-926.

129. Kang Y, Snyder J, Chi M, Li D, More KL, Markovic NM*, et al.* Multimetallic Core/Interlayer/Shell Nanostructures as Advanced Electrocatalysts. *Nano letters* 2014, **14**(11)**:** 6361-6367.

130. Wang D, Li Y. Bimetallic nanocrystals: liquid-phase synthesis and catalytic applications. *Advanced Materials* 2011, **23**(9)**:** 1044-1060.

131. Wu J, Yang H. Platinum-based oxygen reduction electrocatalysts. *Accounts of chemical research* 2013, **46**(8)**:** 1848-1857.

132. Liu H-l, Nosheen F, Wang X. Noble metal alloy complex nanostructures: controllable synthesis and their electrochemical property. *Chemical Society Reviews* 2015, **44**(10)**:** 3056-3078.

133. Shao M, Chang Q, Dodelet JP, Chenitz R. Recent Advances in Electrocatalysts for Oxygen Reduction Reaction. *Chem Rev* 2016, **116**(6)**:** 3594-3657.

134. Lee H, Habas SE, Kweskin S, Butcher D, Somorjai GA, Yang P. Morphological control of catalytically active platinum nanocrystals. *Angewandte Chemie-International Edition* 2006, **45**(46)**:** 7824-7828.

135. Bratlie KM, Lee H, Komvopoulos K, Yang P, Somorjai GA. Platinum nanoparticle shape effects on benzene hydrogenation selectivity. *Nano Letters* 2007, **7**(10)**:** 3097-3101.

136. Habas SE, Lee H, Radmilovic V, Somorjai GA, Yang P. Shaping binary metal nanocrystals through epitaxial seeded growth. *Nature materials* 2007, **6**(9)**:** 692-697.

137. Tao AR, Habas S, Yang P. Shape control of colloidal metal nanocrystals. *small* 2008, **4**(3)**:** 310-325.

138. Zhou K, Li Y. Catalysis Based on Nanocrystals with Well-Defined Facets. *Angewandte Chemie International Edition* 2012, **51**(3)**:** 602-613.

139. Xia Y, Xia X, Peng H-C. Shape-controlled synthesis of colloidal metal nanocrystals: Thermodynamic versus kinetic products. *Journal of the American Chemical Society* 2015, **137**(25)**:** 7947-7966.

140. Chen J, Lim B, Lee EP, Xia Y. Shape-controlled synthesis of platinum nanocrystals for catalytic and electrocatalytic applications. *Nano Today* 2009, **4**(1)**:** 81-95.

141. Yu T, Kim DY, Zhang H, Xia Y. Platinum concave nanocubes with high-index facets and their enhanced activity for oxygen reduction reaction. *Angewandte Chemie* 2011, **123**(12)**:** 2825-2829.

142. Guo S, Zhang S, Sun S. Tuning nanoparticle catalysis for the oxygen reduction reaction. *Angewandte Chemie International Edition* 2013, **52**(33)**:** 8526-8544.

143. Li D, Wang C, Strmcnik DS, Tripkovic DV, Sun X, Kang Y*, et al.* Functional links between Pt single crystal morphology and nanoparticles with different size and shape: the oxygen reduction reaction case. *Energy & Environmental Science* 2014, **7**(12)**:** 4061-4069.

144. Bing Y, Liu H, Zhang L, Ghosh D, Zhang J. Nanostructured Pt-alloy electrocatalysts for PEM fuel cell oxygen reduction reaction. *Chemical Society Reviews* 2010, **39**(6)**:** 2184-2202.

145. Chen A, Holt-Hindle P. Platinum-based nanostructured materials: synthesis, properties, and applications. *Chem Rev* 2010, **110**(6)**:** 3767-3804.

146. Wang D, Zhao P, Li Y. General preparation for Pt-based alloy nanoporous nanoparticles as potential nanocatalysts. *Scientific reports* 2011, **1:** 37.

147. van der Vliet D, Wang C, Debe M, Atanasoski R, Markovic NM, Stamenkovic VR. Platinum-alloy nanostructured thin film catalysts for the oxygen reduction reaction. *Electrochimica Acta* 2011, **56**(24)**:** 8695-8699.

148. van der Vliet DF, Wang C, Tripkovic D, Strmcnik D, Zhang XF, Debe MK*, et al.* Mesostructured thin films as electrocatalysts with tunable composition and surface morphology. *Nature Materials* 2012, **11**(12)**:** 1051-1058.

149. Wu JB, Zhang JL, Peng ZM, Yang SC, Wagner FT, Yang H. Truncated Octahedral Pt3Ni Oxygen Reduction Reaction Electrocatalysts. *Journal of the American Chemical Society* 2010, **132**(14)**:** 4984-+.

150. Zhang J, Yang HZ, Fang JY, Zou SZ. Synthesis and Oxygen Reduction Activity of Shape-Controlled Pt3Ni Nanopolyhedra. *Nano Letters* 2010, **10**(2)**:** 638-644.

151. Wu JB, Gross A, Yang H. Shape and Composition-Controlled Platinum Alloy Nanocrystals Using Carbon Monoxide as Reducing Agent. *Nano Letters* 2011, **11**(2)**:** 798-802.

152. Choi SI, Xie SF, Shao MH, Odell JH, Lu N, Peng HC*, et al.* Synthesis and Characterization of 9 nm Pt-Ni Octahedra with a Record High Activity of 3.3 A/mg(Pt) for the Oxygen Reduction Reaction. *Nano Letters* 2013, **13**(7)**:** 3420-3425.

153. Cui CH, Gan L, Li HH, Yu SH, Heggen M, Strasser P. Octahedral PtNi Nanoparticle Catalysts: Exceptional Oxygen Reduction Activity by Tuning the Alloy Particle Surface Composition. *Nano Letters* 2012, **12**(11)**:** 5885-5889.

154. Cui CH, Gan L, Heggen M, Rudi S, Strasser P. Compositional segregation in shaped Pt alloy nanoparticles and their structural behaviour during electrocatalysis. *Nature Materials* 2013, **12**(8)**:** 765-771.

155. Gan L, Cui C, Heggen M, Dionigi F, Rudi S, Strasser P. Element-specific anisotropic growth of shaped platinum alloy nanocrystals. *Science* 2014, **346**(6216)**:** 1502-1506.

156. Wu Y, Wang D, Chen X, Zhou G, Yu R, Li Y. Defect-dominated shape recovery of nanocrystals: A new strategy for trimetallic catalysts. *Journal of the American Chemical Society* 2013, **135**(33)**:** 12220-12223.

157. Wu Y, Wang D, Niu Z, Chen P, Zhou G, Li Y. A strategy for designing a concave Pt–Ni alloy through controllable chemical etching. *Angewandte Chemie International Edition* 2012, **51**(50)**:** 12524-12528.

158. Strasser P. Catalysts by Platonic design. *Science* 2015, **349**(6246)**:** 379-380.

159. Wang C, Markovic NM, Stamenkovic VR. Advanced Platinum Alloy Electrocatalysts for the Oxygen Reduction Reaction. *Acs Catalysis* 2012, **2**(5)**:** 891-898.

160. Wang C, Wang GF, van der Vliet D, Chang KC, Markovic NM, Stamenkovic VR. Monodisperse Pt3Co nanoparticles as electrocatalyst: the effects of particle size and pretreatment on electrocatalytic reduction of oxygen. *Physical Chemistry Chemical Physics* 2010, **12**(26)**:** 6933-6939.

161. Wang C, Chi MF, Li DG, van der Vliet D, Wang GF, Lin QY*, et al.* Synthesis of Homogeneous Pt-Bimetallic Nanoparticles as Highly Efficient Electrocatalysts. *Acs Catalysis* 2011, **1**(10)**:** 1355-1359.

162. Wang C, Chi MF, Wang GF, van der Vliet D, Li DG, More K*, et al.* Correlation Between Surface Chemistry and Electrocatalytic Properties of Monodisperse PtxNi1-x Nanoparticles. *Advanced Functional Materials* 2011, **21**(1)**:** 147-152.

163. Wang C, Chi MF, Li DG, Strmcnik D, van der Vliett D, Wang GF*, et al.* Design and Synthesis of Bimetallic Electrocatalyst with Multilayered Pt-Skin Surfaces. *Journal of the American Chemical Society* 2011, **133**(36)**:** 14396-14403.

164. Chi M, Wang C, Lei Y, Wang G, Li D, More KL*, et al.* Surface faceting and elemental diffusion behaviour at atomic scale for alloy nanoparticles during in situ annealing. *Nature communications* 2015, **6**.

165. van der Vliet DF, Wang C, Li D, Paulikas AP, Greeley J, Rankin RB*, et al.* Unique electrochemical adsorption properties of Pt-skin surfaces. *Angew Chem Int Ed Engl* 2012, **51**(13)**:** 3139-3142.

166. Niu MT, Wang YS, Cheng Y, Chen GX, Cui LF. Fabrication of Co3O4 cubic nanoframes: Facet-preferential chemical etching of Fe3+ ions to Co3O4 nanocubes. *Materials Letters* 2009, **63**(11)**:** 837-839.

167. Lu XM, Au L, McLellan J, Li ZY, Marquez M, Xia YN. Fabrication of cubic nanocages and nanoframes by dealloying Au/Ag alloy nanoboxes with an aqueous etchant based on Fe(NO3)(3) or NH4OH. *Nano Letters* 2007, **7**(6)**:** 1764-1769.

168. Jang HJ, Hong S, Park S. Shape-controlled synthesis of Pt nanoframes. *Journal of Materials Chemistry* 2012, **22**(37)**:** 19792-19797.

169. Xie SF, Lu N, Xie ZX, Wang JG, Kim MJ, Xia YN. Synthesis of Pd-Rh Core-Frame Concave Nanocubes and Their Conversion to Rh Cubic Nanoframes by Selective Etching of the Pd Cores. *Angewandte Chemie-International Edition* 2012, **51**(41)**:** 10266-10270.

170. Metraux GS, Cao YC, Jin RC, Mirkin CA. Triangular nanofrarnes made of gold and silver. *Nano Letters* 2003, **3**(4)**:** 519-522.

171. Au L, Chen YC, Zhou F, Camargo PHC, Lim B, Li ZY*, et al.* Synthesis and Optical Properties of Cubic Gold Nanoframes. *Nano Research* 2008, **1**(6)**:** 441-449.

172. Mahmoud MA, El-Sayed MA. Gold Nanoframes: Very High Surface Plasmon Fields and Excellent Near-Infrared Sensors. *Journal of the American Chemical Society* 2010, **132**(36)**:** 12704-12710.

173. Si GL, Ma ZF, Li K, Shi WT. Triangular Au-Ag Nanoframes with Tunable Surface Plasmon Resonance Signal from Visible to Near-Infrared Region. *Plasmonics* 2011, **6**(2)**:** 241-244.

174. Hong X, Wang DS, Cai SF, Rong HP, Li YD. Single-Crystalline Octahedral Au-Ag Nanoframes. *Journal of the American Chemical Society* 2012, **134**(44)**:** 18165-18168.

175. Xia BY, Wu HB, Wang X, Lou XW. One-Pot Synthesis of Cubic PtCu3 Nanocages with Enhanced Electrocatalytic Activity for the Methanol Oxidation Reaction. *Journal of the American Chemical Society* 2012, **134**(34)**:** 13934-13937.

176. Liu XW, Wang WY, Li H, Li LS, Zhou GB, Yu R*, et al.* One-Pot Protocol for Bimetallic Pt/Cu Hexapod Concave Nanocrystals with Enhanced Electrocatalytic Activity. *Scientific Reports* 2013, **3:** 5.

177. Nosheen F, Zhang ZC, Zhuang J, Wang X. One-pot fabrication of single-crystalline octahedral Pt-Cu nanoframes and their enhanced electrocatalytic activity. *Nanoscale* 2013, **5**(9)**:** 3660-3663.

178. Han L, Liu H, Cui P, Peng Z, Zhang S, Yang J. Alloy Cu3Pt nanoframes through the structure evolution in Cu-Pt nanoparticles with a core-shell construction. *Scientific reports* 2014, **4**.

179. Jia YY, Jiang YQ, Zhang JW, Zhang L, Chen QL, Xie ZX*, et al.* Unique Excavated Rhombic Dodecahedral PtCu3 Alloy Nanocrystals Constructed with Ultrathin Nanosheets of High-Energy {110} Facets. *Journal of the American Chemical Society* 2014, **136**(10)**:** 3748-3751.

180. Yoon D, Park S, Park J, Kim J, Baik H, Yang H*, et al.* One pot synthesis of hollow Cu-doped Ru octahedral nanocages via an in situ generated metastable Cu nanoparticle template. *Nanoscale* 2014, **6**(21)**:** 12397-12402.

181. Dhavale VM, Kurungot S. Cu-Pt Nanocage with 3-D Electrocatalytic Surface as an Efficient Oxygen Reduction Electrocatalyst for Primary Zn-Air Battery. *ACS Catalysis* 2015.

182. Ding J, Zhu X, Bu L, Yao J, Guo J, Guo S*, et al.* Highly open rhombic dodecahedral PtCu nanoframes. *Chemical Communications* 2015, **51**(47)**:** 9722-9725.

183. Luo S, Shen PK. Concave Platinum-Copper Octopod Nanoframes Bounded With Multiple High-Index Facets for Efficient Electrooxidation Catalysis. *ACS nano* 2016.

184. Luo S, Tang M, Shen PK, Ye S. Atomic-Scale Preparation of Octopod Nanoframes with High-Index Facets as Highly Active and Stable Catalysts. *Advanced Materials* 2016.

185. Zhang Z, Luo Z, Chen B, Wei C, Zhao J, Chen J*, et al.* One-Pot Synthesis of Highly Anisotropic Five-Fold-Twinned PtCu Nanoframes Used as a Bifunctional Electrocatalyst for Oxygen Reduction and Methanol Oxidation. *Advanced Materials* 2016, **28**(39)**:** 8712-8717.

186. Hung LI, Tsung CK, Huang W, Yang P. Room-Temperature Formation of Hollow Cu2O Nanoparticles. *Advanced Materials* 2010, **22**(17)**:** 1910-1914.

187. Chen C, Kang Y, Huo Z, Zhu Z, Huang W, Xin HL*, et al.* Highly crystalline multimetallic nanoframes with three-dimensional electrocatalytic surfaces. *Science* 2014, **343**(6177)**:** 1339-1343.

188. Wu Y, Wang D, Zhou G, Yu R, Chen C, Li Y. Sophisticated Construction of Au Islands on Pt–Ni: An Ideal Trimetallic Nanoframe Catalyst. *Journal of the American Chemical Society* 2014, **136**(33)**:** 11594-11597.

189. Oh A, Baik H, Choi DS, Cheon JY, Kim B, Kim H*, et al.* Skeletal Octahedral Nanoframe with Cartesian Coordinates via Geometrically Precise Nanoscale Phase Segregation in a Pt@ Ni Core–Shell Nanocrystal. *ACS nano* 2015, **9**(3)**:** 2856-2867.

190. Wang Y, Chen Y, Nan C, Li L, Wang D, Peng Q*, et al.* Phase-transfer interface promoted corrosion from PtNi10 nanoctahedra to Pt4Ni nanoframes. *Nano Research* 2015**:** 1-16.

191. Wang C, Zhang L, Yang H, Pan J, Liu J, Dotse C*, et al.* High-Indexed Pt3Ni Alloy Tetrahexahedral Nanoframes Evolved through Preferential CO Etching. *Nano Letters* 2017.

192. Somorjai GA, Park JY. Colloid science of metal nanoparticle catalysts in 2D and 3D structures. Challenges of nucleation, growth, composition, particle shape, size control and their influence on activity and selectivity. *Topics in Catalysis* 2008, **49**(3-4)**:** 126-135.

193. Bell AT. The impact of nanoscience on heterogeneous catalysis. *Science* 2003, **299**(5613)**:** 1688-1691.

194. Yin Y, Alivisatos AP. Colloidal nanocrystal synthesis and the organic–inorganic interface. *Nature* 2005, **437**(7059)**:** 664-670.

195. Talapin DV, Lee J-S, Kovalenko MV, Shevchenko EV. Prospects of colloidal nanocrystals for electronic and optoelectronic applications. *Chemical reviews* 2009, **110**(1)**:** 389-458.

196. Tao A, Sinsermsuksakul P, Yang P. Tunable plasmonic lattices of silver nanocrystals. *Nature Nanotechnology* 2007, **2**(7)**:** 435-440.

197. Sun SH, Murray CB, Weller D, Folks L, Moser A. Monodisperse FePt nanoparticles and ferromagnetic FePt nanocrystal superlattices. *Science* 2000, **287**(5460)**:** 1989-1992.

198. Murray CB, Sun SH, Doyle H, Betley T. Monodisperse 3d transition-metal (Co, Ni, Fe) nanoparticles and their assembly into nanoparticle superlattices. *Mrs Bulletin* 2001, **26**(12)**:** 985-991.

199. Song H, Kim F, Connor S, Somorjai GA, Yang P. Pt nanocrystals: Shape control and Langmuir-Blodgett monolayer formation. *The Journal of Physical Chemistry B* 2005, **109**(1)**:** 188-193.

200. Yin Y, Rioux RM, Erdonmez CK, Hughes S, Somorjai GA, Alivisatos AP. Formation of hollow nanocrystals through the nanoscale Kirkendall effect. *Science* 2004, **304**(5671)**:** 711-714.

201. Toshima N, Yonezawa T. Bimetallic nanoparticles—novel materials for chemical and physical applications. *New Journal of Chemistry* 1998, **22**(11)**:** 1179-1201.

202. Kim D, Resasco J, Yu Y, Asiri AM, Yang P. Synergistic geometric and electronic effects for electrochemical reduction of carbon dioxide using gold–copper bimetallic nanoparticles. *Nature communications* 2014, **5**.

203. Shevchenko EV, Talapin DV, Rogach AL, Kornowski A, Haase M, Weller H. Colloidal synthesis and self-assembly of CoPt3 nanocrystals. *Journal of the American Chemical Society* 2002, **124**(38)**:** 11480-11485.

204. Shevchenko EV, Talapin DV, Schnablegger H, Kornowski A, Festin Ö, Svedlindh P*, et al.* Study of nucleation and growth in the organometallic synthesis of magnetic alloy nanocrystals: the role of nucleation rate in size control of CoPt3 nanocrystals. *Journal of the American Chemical Society* 2003, **125**(30)**:** 9090-9101.

205. Schulenburg H, Muller E, Khelashvili G, Roser T, Bonnemann H, Wokaun A*, et al.* Heat-Treated PtCo3 Nanoparticles as Oxygen Reduction Catalysts. *Journal of Physical Chemistry C* 2009, **113**(10)**:** 4069-4077.

206. Tzitzios V, Niarchos D, Margariti G, Fidler J, Petridis D. Synthesis of CoPt nanoparticles by a modified polyol method: characterization and magnetic properties. *Nanotechnology* 2005, **16**(2)**:** 287.

207. Ely TO, Pan C, Amiens C, Chaudret B, Dassenoy F, Lecante P*, et al.* Nanoscale Bimetallic Co x Pt1-x Particles Dispersed in Poly (vinylpyrrolidone): Synthesis from Organometallic Precursors and Characterization. *The Journal of Physical Chemistry B* 2000, **104**(4)**:** 695-702.

208. Sanchez J, Moran-Lopez J, Leroux C, Cadeville M. Magnetic properties and chemical ordering in Co-Pt. *Journal of Physics: Condensed Matter* 1989, **1**(2)**:** 491.

209. Okamoto H. Co-Pt (cobalt-platinum). *Journal of phase equilibria* 2001, **22**(5)**:** 591-591.

210. Lee B, Alsenz R, Ignatiev A, Van Hove M. Surface structures of the two allotropic phases of cobalt. *Physical Review B* 1978, **17**(4)**:** 1510.

211. Pennycook S. Z-contrast STEM for materials science. *Ultramicroscopy* 1989, **30**(1)**:** 58-69.

212. Vanysek P. Electrochemical series. *Handbook of Chemistry and Physics* 1998, **88**.

213. Mourdikoudis S, Liz-Marzan LM. Oleylamine in Nanoparticle Synthesis. *Chemistry of Materials* 2013, **25**(9)**:** 1465-1476.

214. Yu Y, Yang W, Sun X, Zhu W, Li X-Z, Sellmyer D*, et al.* Monodisperse MPt (M= Fe, Co, Ni, Cu, Zn) Nanoparticles Prepared from a Facile Oleylamine Reduction of Metal Salts. *Nano letters* 2014, **14**(5)**:** 2778-2782.

215. Sun S, Murray C. Synthesis of monodisperse cobalt nanocrystals and their assembly into magnetic superlattices. *Journal of Applied Physics* 1999, **85**(8)**:** 4325-4330.

216. Puntes VF, Krishnan KM, Alivisatos AP. Colloidal nanocrystal shape and size control: The case of cobalt. *Science* 2001, **291**(5511)**:** 2115-2117.

217. Zhang J, Fang JY. A General Strategy for Preparation of Pt 3d-Transition Metal (Co, Fe, Ni) Nanocubes. *Journal of the American Chemical Society* 2009, **131**(51)**:** 18543-18547.

218. Zhao JL, Spasova M, Li ZA, Zharnikov M. Ferromagnetic Cobalt Nanoparticles and Their Immobilization on Monomolecular Films and Chemical Templates. *Advanced Functional Materials* 2011, **21**(24)**:** 4724-4735.

219. Porter NS, Wu H, Quan ZW, Fang JY. Shape-Control and Electrocatalytic Activity-Enhancement of Pt-Based Bimetallic Nanocrystals. *Accounts of Chemical Research* 2013, **46**(8)**:** 1867-1877.

220. Oezaslan M, Hasché F, Strasser P. Oxygen electroreduction on PtCo3, PtCo and Pt3Co alloy nanoparticles for alkaline and acidic PEM fuel cells. *Journal of The Electrochemical Society* 2012, **159**(4)**:** B394-B405.

221. Hasché F, Oezaslan M, Strasser P. Activity, stability, and degradation mechanisms of dealloyed PtCu3 and PtCo3 nanoparticle fuel cell catalysts. *ChemCatChem* 2011, **3**(11)**:** 1805-1813.

222. Oezaslan M, Strasser P. Activity of dealloyed PtCo 3 and PtCu 3 nanoparticle electrocatalyst for oxygen reduction reaction in polymer electrolyte membrane fuel cell. *Journal of Power Sources* 2011, **196**(12)**:** 5240-5249.

223. Powell C, Jablonski A. NIST Electron Inelastic-Mean-Free-Path Database, Version 1.2, SRD 71; National Institute of Standards and Technology: Gaithersburg, MD, 2010. *There is no corresponding record for this reference.*

224. Carpenter MK, Moylan TE, Kukreja RS, Atwan MH, Tessema MM. Solvothermal Synthesis of Platinum Alloy Nanoparticles for Oxygen Reduction Electrocatalysis. *Journal of the American Chemical Society* 2012, **134**(20)**:** 8535-8542.

225. Huang X, Zhao Z, Cao L, Chen Y, Zhu E, Lin Z*, et al.* High-performance transition metal–doped Pt3Ni octahedra for oxygen reduction reaction. *Science* 2015, **348**(6240)**:** 1230-1234.

226. Cremer PS, Su X, Shen YR, Somorjai GA. Ethylene hydrogenation on Pt (111) monitored in situ at high pressures using sum frequency generation. *Journal of the American Chemical Society* 1996, **118**(12)**:** 2942-2949.

227. Tao F, Grass ME, Zhang Y, Butcher DR, Renzas JR, Liu Z*, et al.* Reaction-driven restructuring of Rh-Pd and Pt-Pd core-shell nanoparticles. *Science* 2008, **322**(5903)**:** 932-934.

228. Zheng F, Alayoglu S, Guo JH, Pushkarev V, Li YM, Glans PA*, et al.* In-situ X-ray Absorption Study of Evolution of Oxidation States and Structure of Cobalt in Co and CoPt Bimetallic Nanoparticles (4 nm) under Reducing (H-2) and Oxidizing (O-2) Environments. *Nano Letters* 2011, **11**(2)**:** 847-853.

229. Jia Q, Caldwell K, Ramaker DE, Ziegelbauer JM, Liu Z, Yu Z*, et al.* In Situ Spectroscopic Evidence for Ordered Core–Ultrathin Shell Pt1Co1 Nanoparticles with Enhanced Activity and Stability as Oxygen Reduction Electrocatalysts. *The Journal of Physical Chemistry C* 2014, **118**(35)**:** 20496-20503.

230. Caldwell KM, Ramaker DE, Jia Q, Mukerjee S, Ziegelbauer JM, Kukreja RS*, et al.* Spectroscopic in situ Measurements of the Relative Pt Skin Thicknesses and Porosities of Dealloyed PtMn (Ni, Co) Electrocatalysts. *The Journal of Physical Chemistry C* 2015, **119**(1)**:** 757-765.

231. Jia Q, Liang W, Bates MK, Mani P, Lee W, Mukerjee S. Activity Descriptor Identification for Oxygen Reduction on Pt-based Bimetallic Nanoparticles: In situ Observation of the Linear Composition-Strain-Activity Relationship. *ACS nano* 2015, **9**(1)**:** 387-400.

232. Friebel D, Miller DJ, O'Grady CP, Anniyev T, Bargar J, Bergmann U*, et al.* In situ X-ray probing reveals fingerprints of surface platinum oxide. *Physical Chemistry Chemical Physics* 2011, **13**(1)**:** 262-266.

233. Li DG, Wang C, Tripkovic D, Sun SH, Markovic NM, Stamenkovic VR. Surfactant Removal for Colloidal Nanoparticles from Solution Synthesis: The Effect on Catalytic Performance. *Acs Catalysis* 2012, **2**(7)**:** 1358-1362.

234. Trasatti S, Petrii O. Real surface area measurements in electrochemistry. *Pure and applied chemistry* 1991, **63**(5)**:** 711-734.

235. Fernández-García M. XANES analysis of catalytic systems under reaction conditions. *Catalysis Reviews* 2002, **44**(1)**:** 59-121.

236. Pandya K, Hoffman R, McBreen J, O'Grady W. In Situ X-Ray Absorption Spectroscopic Studies of Nickel Oxide Electrodes. *Journal of The Electrochemical Society* 1990, **137**(2)**:** 383-388.

237. De Groot F. High-resolution X-ray emission and X-ray absorption spectroscopy. *Chemical Reviews* 2001, **101**(6)**:** 1779-1808.

238. Brown M, Peierls R, Stern E. White lines in x-ray absorption. *Physical Review B* 1977, **15**(2)**:** 738.

239. Mansour AN, Cook JW, Sayers DE. Quantitative technique for the determination of the number of unoccupied d-electron states in a platinum catalyst using the l2,3 x-ray absorption-edge spectra. *Journal of Physical Chemistry* 1984, **88**(11)**:** 2330-2334.

240. Ahmadi M, Behafarid F, Cui C, Strasser P, Cuenya BR. Long-range segregation phenomena in shape-selected bimetallic nanoparticles: Chemical state effects. *Acs Nano* 2013, **7**(10)**:** 9195-9204.

241. Frenkel AI. Applications of extended X-ray absorption fine-structure spectroscopy to studies of bimetallic nanoparticle catalysts. *Chemical Society Reviews* 2012, **41**(24)**:** 8163-8178.

242. Frenkel AI. Solving the structure of nanoparticles by multiple-scattering EXAFS analysis. *Journal of synchrotron radiation* 1999, **6**(3)**:** 293-295.

243. Alayoglu S, Zavalij P, Eichhorn B, Wang Q, Frenkel AI, Chupas P. Structural and architectural evaluation of bimetallic nanoparticles: a case study of Pt− Ru core− shell and alloy nanoparticles. *Acs Nano* 2009, **3**(10)**:** 3127-3137.

244. Hwang B-J, Sarma LS, Chen J-M, Chen C-H, Shih S-C, Wang G-R*, et al.* Structural models and atomic distribution of bimetallic nanoparticles as investigated by X-ray absorption spectroscopy. *Journal of the American Chemical Society* 2005, **127**(31)**:** 11140-11145.

245. Nashner MS, Frenkel AI, Somerville D, Hills CW, Shapley JR, Nuzzo RG. Core shell inversion during nucleation and growth of bimetallic Pt/Ru nanoparticles. *Journal of the American Chemical Society* 1998, **120**(32)**:** 8093-8101.

246. Ferrando R, Jellinek J, Johnston RL. Nanoalloys: From theory to applications of alloy clusters and nanoparticles. *Chemical Reviews* 2008, **108**(3)**:** 845-910.

247. Narayanan R, El-Sayed MA. Shape-dependent catalytic activity of platinum nanoparticles in colloidal solution. *Nano letters* 2004, **4**(7)**:** 1343-1348.

248. Xia Y, Xiong Y, Lim B, Skrabalak SE. Shape-Controlled Synthesis of Metal Nanocrystals: Simple Chemistry Meets Complex Physics? *Angewandte Chemie International Edition* 2009, **48**(1)**:** 60-103.

249. Becknell N, Kang Y, Chen C, Resasco J, Kornienko N, Guo J*, et al.* Atomic Structure of Pt3Ni Nanoframe Electrocatalysts by in Situ X-ray Absorption Spectroscopy. *Journal of the American Chemical Society* 2015, **137**(50)**:** 15817-15824.

250. Becknell N, Zheng C, Chen C, Yu Y, Yang P. Synthesis of PtCo 3 polyhedral nanoparticles and evolution to Pt 3 Co nanoframes. *Surface Science* 2016, **648:** 328-332.

251. Zeng J, Zhu C, Tao J, Jin M, Zhang H, Li ZY*, et al.* Controlling the nucleation and growth of silver on palladium nanocubes by manipulating the reaction kinetics. *Angewandte Chemie International Edition* 2012, **51**(10)**:** 2354-2358.

252. Watt J, Young N, Haigh S, Kirkland A, Tilley RD. Synthesis and structural characterization of branched palladium nanostructures. *Advanced Materials* 2009, **21**(22)**:** 2288-2293.

253. Williams DB, Carter CB. The transmission electron microscope. *Transmission electron microscopy*. Springer, 1996, pp 3-17.

254. Ravel B, Newville M. ATHENA, ARTEMIS, HEPHAESTUS: data analysis for X-ray absorption spectroscopy using IFEFFIT. *Journal of synchrotron radiation* 2005, **12**(4)**:** 537-541.

255. Zabinsky S, Rehr J, Ankudinov A, Albers R, Eller M. Multiple-scattering calculations of X-ray-absorption spectra. *Physical Review B* 1995, **52**(4)**:** 2995.

256. Wang G, Van Hove MA, Ross PN, Baskes MI. Quantitative prediction of surface segregation in bimetallic Pt–M alloy nanoparticles (M= Ni, Re, Mo). *Progress in Surface Science* 2005, **79**(1)**:** 28-45.

257. Dahmani C, Cadeville M, Sanchez J, Moran-Lopez J. Ni-Pt phase diagram: experiment and theory. *Physical review letters* 1985, **55**(11)**:** 1208.

258. Nash P, Singleton M. The Ni-Pt (Nickel-Platinum) System. *Journal of Phase Equilibria* 1989, **10**(3)**:** 258-262.

259. Seo O, Lee JY, Kim JM, Kim J-W, Kang HC, Chung J. Chemical ordering in PtNi nanocrystals. *Journal of Alloys and Compounds* 2016, **666:** 232-236.

260. Cui C, Ahmadi M, Behafarid F, Gan L, Neumann M, Heggen M*, et al.* Shape-selected bimetallic nanoparticle electrocatalysts: evolution of their atomic-scale structure, chemical composition, and electrochemical reactivity under various chemical environments. *Faraday discussions* 2013, **162:** 91-112.

261. Zeng J, Zheng Y, Rycenga M, Tao J, Li Z-Y, Zhang Q*, et al.* Controlling the shapes of silver nanocrystals with different capping agents. *Journal of the American Chemical Society* 2010, **132**(25)**:** 8552-8553.

262. Niu Z, Li Y. Removal and utilization of capping agents in nanocatalysis. *Chemistry of Materials* 2013, **26**(1)**:** 72-83.

263. Turner JA. Sustainable hydrogen production. *Science* 2004, **305**(5686)**:** 972-974.

264. Han B, Carlton CE, Kongkanand A, Kukreja RS, Theobald BR, Gan L*, et al.* Record activity and stability of dealloyed bimetallic catalysts for proton exchange membrane fuel cells. *Energy & Environmental Science* 2015, **8**(1)**:** 258-266.

265. Niu Z, Becknell N, Yu Y, Kim D, Chen C, Kornienko N*, et al.* Anisotropic phase segregation and migration of Pt in nanocrystals en route to nanoframe catalysts. *Nature Materials* 2016, **15:** 1188–1194.

266. Patterson A. The Scherrer formula for X-ray particle size determination. *Physical review* 1939, **56**(10)**:** 978.

267. Cumpson PJ. Angle-resolved XPS and AES: depth-resolution limits and a general comparison of properties of depth-profile reconstruction methods. *Journal of Electron Spectroscopy and Related Phenomena* 1995, **73**(1)**:** 25-52.

268. Koningsberger DC, Mojet BL, van Dorssen GE, Ramaker DE. XAFS spectroscopy; fundamental principles and data analysis. *Topics in Catalysis* 2000, **10**(3-4)**:** 143-155.

A1. Methods of Chapter 2

Portions of the content of this chapter are reprinted or adapted with permission from N. Becknell, C. Zheng, C. Chen, Y. Yu, P. Yang, "Synthesis of $PtCo_3$ polyhedral nanoparticles and evolution to Pt_3Co nanoframes", Surf. Sci., 2016, 648, 328. DOI: 10.1016/j.susc.2015.09.024. Copyright 2016 Elsevier B.V.

A1.1 $PtCo_3$ Nanoparticle Synthesis

Chloroplatinic acid hexahydrate ($H_2PtCl_6 \cdot 6H_2O$), cobalt acetate tetrahydrate ($(CH_3COO)_2Co \cdot 4H_2O$), oleylamine (technical grade, 70%) and oleic acid (technical grade, 90%) were purchased from Sigma Aldrich. Chloroplatinic acid (28.5 mg) and cobalt acetate tetrahydrate (60 mg) were dissolved into 285 μL ultrapure water and then mixed with 3 mL oleylamine. This mixture was homogenized by stirring at 60 °C under nitrogen for 30 minutes. Oleylamine (5 mL) and oleic acid (2 mL) were added to a 25 mL three-neck flask and heated at 180 °C under argon for 45 minutes. Next, the precursor mixture was injected into the three-neck flask and heated under argon flow for 3 minutes. Then, the temperature of the reaction solution was increased to 240 °C. The solution went from dark purple to black. The NP solution was held at 240 °C for 2 minutes for growth of the particles before being rapidly cooled in a water bath. The particles were washed once with ethanol and a second time with hexanes and ethanol by centrifuging at 12,000 rpm for 10 minutes. After washing, the particles could be dispersed in solvents such as hexanes or chloroform.

A1.2 Evolution to Pt_3Co Nanoframes

The as-synthesized NPs (~ 2 mg) were dispersed into 2.5 mL chloroform with 300 μL oleylamine added. This solution was then diluted with 10 mL hexadecane and sonicated for 1 hour. The suspension of NPs was then heated at 130 °C with occasional sonication required to re-disperse the highly magnetic NPs. After heating for 6 hours, the NPs had fully evolved to hollow NFs.

A1.3 Characterization of Pt-Co Nanoparticles and Nanoframes

Nanoparticle and nanoframe samples were imaged by TEM using a Hitachi H-7650 TEM and SEM using a Zeiss Gemini Ultra-55 Field Emission SEM to determine size and morphology. EDS was also performed with TEM to determine composition of the bimetallic NPs and NFs. HRTEM was performed with an F20 UT Tecnai to confirm crystallinity and structure of the Pt-Co samples. HAADF-STEM and EDS mapping were performed with an FEI TitanX to characterize the elemental distribution in the NPs and NFs.

The crystalline phase of the samples was determined through XRD with a Bruker D-8 General Area Detector Diffraction System (GADDS) with HI-STAR area charge-coupled device (CCD) detector. The instrument was equipped with a Co-Kα source (λ = 1.789 Å). The composition of the samples was determined through XRD, EDS, and ICP-OES using a PerkinElmer Optima 7000 DV.

The behavior of the surface of the NPs was analyzed with APXPS on the Scienta R4000 HiPP endstation at the Lawrence Berkeley National Laboratory ALS Beamline 9.3.2. Samples were prepared on silicon substrates and mounted on a ceramic button heater sample holder in order to heat the sample up to 120 °C during experiments. The atmosphere was controlled at ultra-high vacuum (UHV, ~10^{-9} torr) or 100 mTorr of H_2 or O_2 by introducing the gases into the chamber through different molecular leak valves. XPS spectra were collected using an incident x-ray energy of 490 eV. The binding energy for XPS spectra was calibrated to the Au 4f core level of a Au foil. The XPS spectra were quantitatively analyzed by subtracting a Shirley background.

A2. Methods of Chapter 3

Portions of the content and figures of this chapter are reprinted or adapted with permission from N. Becknell, Y. Kang, C. Chen, J. Resasco, N. Kornienko, J. Guo, N. M. Markovic, G. A. Somorjai, V. R. Stamenkovic, P. Yang, "Atomic Structure of Pt3Ni Nanoframe Electrocatalysts by in situ X-ray Absorption Spectroscopy", J. Am. Chem. Soc., 2015, 137, 15817. DOI: 10.1021/jacs.5b09639. Copyright 2015 American Chemical Society.

A2.1 Synthesis of $PtNi_3$ Nanopolyhedra

Twenty milligrams of $H_2PtCl_6 \cdot 6H_2O$ and 17.5 mg of $Ni(NO_3)_2 \cdot 6H_2O$ were dissolved in 0.4 mL of deionized water, forming a transparent yellow solution. Ten milliliters of oleylamine was preheated in a three-necked flask at 160 °C for 1 h with argon purging, after which the aqueous precursor solution was injected. The reaction was held at 160 °C for 3 min under vacuum to remove water. The reaction system was further heated to 265 °C under argon atmosphere. After reaching 265 °C, the solution turned from transparent to black. After it had turned black, the reaction solution was then held for a further 3 min for growth of the particles. The reaction was stopped by rapidly cooling the solution down to room temperature. The synthesized $PtNi_3$ nanopolyhedra were washed once by ethanol and a second time by hexane and ethanol and were collected by centrifugation (8,000 rpm) after each wash. The washed product was re-dispersed in either hexanes or chloroform.

A2.2 Evolution from $PtNi_3$ Nanopolyhedra to Pt_3Ni Nanoframes

The $PtNi_3$ nanopolyhedra were re-dispersed in chloroform to a concentration of approximately 1 mg/mL. Three milliliters of this $PtNi_3$ nanopolyhedra solution was sonicated with 0.2 mL of oleylamine and diluted with 10 mL of hexadecane. This colloidal solution was sonicated for 30 min, followed by heating at 130 °C for 8 h in air to carry out the spontaneous oxidation and corrosion of $PtNi_3$ nanopolyhedra to Pt_3Ni nanoframes. Alternate combinations of temperature and timing can also be used during evolution, as reported previously.[187] After evolution, the Pt_3Ni nanoframes were washed two times with hexane and ethanol and collected by centrifugation (8,000 rpm). The washed nanoframes were re-dispersed in chloroform.

A2.3 Preparation of Pt_3Ni/C Nanocatalyst and Testing

Pt_3Ni nanoframes dispersed in chloroform were added to carbon (Cabot, Vulcan XC-72) in a ratio which produced the desired loading of platinum on carbon. The actual loadings were determined by ICP-MS. The mixture was sonicated in chloroform for 30-45 min to complete the loading process. The catalyst was collected by centrifugation (10,000 rpm), washed once with hexanes, and recollected by centrifugation. The resulting catalyst powder was heated at 200 °C in air for at least 12 h in order to conduct simultaneous removal of organic surfactants and Pt-skin segregation. The catalyst was kept

dry until preparation for electrochemical testing. Typically, the Pt_3Ni/C catalyst was dispersed in water with a concentration between 0.5 and 1 mg/mL. The catalyst ink was drop-cast onto a 6 mm glassy carbon disk in a volume of 10–20 μL and allowed to air-dry. The electrochemical measurements were conducted in a three-compartment electrochemical cell with a Pine RDE setup and an Autolab 302 potentiostat. A saturated Ag/AgCl electrode and a Pt wire were used as reference and counter electrodes, respectively, and 0.1 M $HClO_4$ was used as the electrolyte. All of the potentials are presented versus RHE. The nanoframe catalyst was typically held at 0.05 V vs RHE between measurements, and the limits of the cyclic voltammetry were 0.05–1.0 V. Measurements with H_{upd} were performed by saturating the electrolyte with argon gas before collecting the CV at a sweep rate of 50 mV/s. Electrooxidation of adsorbed CO, or CO-stripping measurements, were performed by purging CO through the electrolyte while holding the potential at 0.05 V. Argon was then purged to remove CO from the electrolyte and the CV was collected at a sweep rate of 50 mV/s. The ORR measurements were collected under O_2 purging conditions and at 20 mV/s with an RDE rotation rate of 1,600 rpm. The current densities for ORR were corrected for ohmic iR drop.

A2.4 X-ray Diffraction

Micro-XRD experiments were carried out at the Lawrence Berkeley Laboratory ALS Beamline 10.3.2 with an energy of 17 keV corresponding to a wavelength of 0.729 Å. The detector used was a Bruker APEX II CCD detector and the sample-to-detector distance was calibrated with an α-Al_2O_3 standard. Data reduction was performed with FIT2D to obtain diffraction patterns in Q-space.

A2.5 X-ray Absorption Measurements and Data Analysis

The Pt_3Ni/C catalyst ink was prepared at a concentration of 1 mg/mL in a solution of equal parts water and isopropanol and a concentration of 0.5% Nafion. A typical electrode for XAS was prepared with 20 μL of catalyst ink dropcast on a carbon paper substrate. A custom-made electrochemical cell was fabricated for *in situ* ORR measurements, in which the carbon paper acted as both the working electrode and X-ray transparent window (Fig. A2.1). The electrochemical measurements were carried out in 0.1 M $HClO_4$ using a Ag/AgCl reference electrode and a platinum wire counter electrode. The electrolyte was continuously purged with high purity oxygen for ORR.

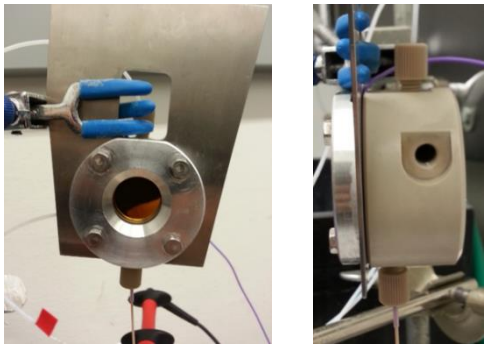


Figure A2.1. *In situ* electrochemical XAS cell. Front and side views show the bottom port for a Ag/AgCl reference electrode, the top port for a Pt wire counter electrode, and side ports for gas or liquid flow.

XANES and EXAFS data were collected at the ALS Beamline 10.3.2. The X-ray wavelength was monochromatized by a Si(111) double-crystal, fixed exit monochromator. The intensity of the incident X-ray radiation, I_0, was monitored with a nitrogen filled ionization chamber. All data were collected in fluorescence mode with a 7-element Ge detector (Canberra). The data at the Ni *K*-edge and Pt L_3-edge were calibrated to a Ni foil and Pt foil, respectively. All spectra at a given edge were aligned according to a glitch in I_0 near each absorption edge.

XANES and EXAFS data reduction and EXAFS fitting were performed using the IFEFFIT based programs Athena and Artemis.[254] Edge step normalization for each spectra was performed by subtracting the pre-edge and post-edge backgrounds in Athena. For EXAFS background removal, a cubic spline was fit to the data and the *k*-space data were Fourier transformed resulting in an *R*-space spectrum which was fit in Artemis using multiple *k*-weight fitting (k^1, k^2, k^3). EXAFS data were fit to the EXAFS function shown in Eq. A2.1:

$$\chi(k) = S_0^2 \sum_{i=1}^{shells} \frac{N_i}{kR_i^2} F_i(k) e^{-2k^2\sigma_i^2} e^{-2R_i/\lambda(k)} \sin[2kR_i - \varphi_i(k)] \quad \text{(A2.1)}$$

The amplitude of the contribution from each coordination shell in the EXAFS function is summed to generate a fit to the data. S_0^2 represents an amplitude reduction factor which is typically assumed to be chemically transferable and is affected by shake-up effects at the absorbing atom.[268] It was estimated by performing a fit to EXAFS transmission measurements on Ni and Pt metal foils. Values for S_0^2 were determined to be 0.80 for Pt and 0.78 for Ni. N_i and R_i are the coordination number and half-path length between the central absorbing atom and a scattering atom, respectively. The mean-square disorder in the distance from the central absorbing atom to a given shell due to thermal fluctuation and structural disorder is represented by σ_i^2. These parameters are calculated by fitting the experimental data. The photoelectron mean free path is represented by λ. Lastly, $F_i(k)$ is the backscattering amplitude and $\varphi_i(k)$ is the the phase factor for a given coordination shell. These parameters are calculated through *ab initio* methods using FEFF6 as embedded in Artemis and Atoms.

A3. Methods of Chapter 4

Portions of the content and figures of this chapter are reprinted or adapted with permission from Z. Niu†, N. Becknell†, Y. Yu, D. Kim, C. Chen, N. Kornienko, G. A. Somorjai, P. Yang, "Anisotropic phase segregation and migration of Pt in nanocrystals en route to nanoframe catalysts", Nat. Mater., 2016, 15, 1188. DOI: 10.1038/nmat4724. Copyright 2016 Macmillan Publishers Ltd: Nature Materials.

A3.1 Chemicals

Chloroplatinic acid hexahydrate ($H_2PtCl_6 \cdot 6H_2O$, ≥37.5% Pt basis), nickel(II) nitrate hexahydrate ($Ni(NO_3)_2 \cdot 6H_2O$, ≥98.5%), oleylamine (technical grade, 70%) and hexane (≥98.5%) were purchased from Sigma-Aldrich. Acetic acid (≥99.7%) was purchased from EMD. Toluene (≥99.9%) was purchased from Fisher Scientific. All chemicals were used as received without further purification.

A3.2 Synthesis of Pt–Ni Rhombic Dodecahedra

Aqueous solutions of $H_2PtCl_6 \cdot 6H_2O$ (0.1 g ml^{-1}, 0.4 ml) and $Ni(NO_3)_2 \cdot 6H_2O$ (0.1 g ml^{-1}, 0.35 ml) were mixed with one milliliter of oleylamine in a small vial. The mixture was heated at 120 °C under stirring for one hour, forming a transparent green solution after removal of water. Ten milliliters of oleylamine that had been preheated in a three-necked flask at 160 °C for one hour under nitrogen purging was raised to 230 °C just before the injection. The precursor solution was injected into the three-necked flask immediately after reaching 230 °C. The green reaction solution gradually turned yellow, brown and then black when kept at 230 °C for about one hour. After the growth solution turned black, aliquots were taken out by syringe after 3 min, 10 min and 30 min, and respectively termed as RD-3, RD-10 and RD-30. Before the solution turned black, intermediate products generally termed as pre-RD were collected by stopping the whole batch of reaction to get enough sample for further analysis. All the samples were washed two times by hexane/ethanol mixture, collected by centrifugation (12,000 rpm) after each wash, and then re-dispersed in toluene or hexane.

A3.3 Chemical Corrosion of Pt–Ni Rhombic Dodecahedra to $Pt_{75}Ni_{25}$ 3-D Structures

Ten microliters of oleylamine was added into a toluene dispersion of Pt–Ni rhombic dodecahedra (~0.5–1 mg ml^{-1}, 2 ml). The colloidal dispersion was briefly sonicated and mixed with two milliliters of acetic acid. The mixture was heated at 90 °C under vigorous stirring for two hours in air to allow chemical corrosion of Pt–Ni rhombic dodecahedra to corresponding $Pt_{75}Ni_{25}$ tetradecapod or frame structures. After corrosion, the products were washed with hexane/ethanol mixture and collected by centrifugation (12,000 rpm). The washed products were re-dispersed in hexane or chloroform.

A3.4 Characterization

TEM and quantitative EDS were performed with a Hitachi H-7650 equipped with EDAX microanalysis. HRTEM was taken using an FEI Tecnai F20 at an accelerating voltage of 200 kV. HAADF-STEM and EDS mapping were carried out with an FEI TitanX 60-300. XRD was acquired using a Bruker D-8 GADDS with HI-STAR area CCD detector, equipped with a Co-Kα source (λ = 1.789 Å). ICP-OES was measured using a PerkinElmer Optima 7000 DV. XPS was performed using a PHI 5600 X-ray photoelectron spectrometer.

A3.5 Electrochemical Characterization

After chemical corrosion, $Pt_{75}Ni_{25}$ tetradecapods or nanoframes were dispersed in chloroform and added to carbon (Cabot, Vulcan XC-72) in a ratio which produced a loading of 17–20 wt% Pt. The mixture was sonicated in chloroform for 30 to 45 min to complete the loading process. The catalyst was collected by centrifugation (10,000 rpm), washed once with hexanes, and recollected by centrifugation. The resulting catalyst powder was heated at 200 °C in air for 14 h to remove organic surfactants. The $Pt_{75}Ni_{25}$/C catalyst was then dispersed in water with a concentration of 0.5 $mg_{catalyst}$ ml^{-1}. The actual concentration of Pt in the ink was determined by ICP-OES. The catalyst ink was dropcast onto a 5 mm glassy carbon disk (Pine Instruments) in the appropriate volume to achieve 6.9 μg_{Pt} cm^{-2} loading density and allowed to air dry. The commercial Pt/C catalyst (Alfa, ~20 wt% Pt) had a loading density of 7.8 μg_{Pt} cm^{-2}. The electrochemical measurements were conducted in a three-compartment glass electrochemical cell with a Pine RDE set-up and a Biologic VSP potentiostat. A saturated Ag/AgCl electrode and a Pt wire were used as reference and counter electrodes, respectively, and 0.1 M $HClO_4$ prepared from 67% $HClO_4$ (Sigma-Aldrich) was used as the electrolyte. All potentials are presented versus RHE. The catalyst was typically held at 0.05 V versus RHE between measurements, and the limits of the cyclic voltammetry were 0.05–1.02 V. H_{upd} measurements were performed by saturating the electrolyte with argon gas before collecting the CV at a sweep rate of 50 mV s^{-1}. Electrooxidation of adsorbed CO, or CO-stripping measurements, were performed by purging CO through the electrolyte while holding the potential at 0.05 V. Argon was then purged to remove CO from the electrolyte and the CV was collected at a sweep rate of 50 mV s^{-1}. The ORR measurements were collected under O_2 purging conditions and at 20 mV s^{-1} with an RDE rotation rate of 1,600 rpm. The current densities for ORR were corrected for ohmic iR drop.

A3.6 EXAFS Data Collection and Analysis

EXAFS data were collected at the ALS Beamline 10.3.2. The data at the Ni *K*-edge and Pt L_3-edge were calibrated to a Ni foil and Pt foil, respectively. All spectra at a given edge were aligned according to a glitch in I_0 near each absorption edge. EXAFS data reduction and EXAFS fitting was performed using the IFEFFIT based programs Athena and Artemis.[254] For additional details on the data collection and reduction, please see Appendix A2.5.

The Ni *K*-edge and Pt L_3-edge were fit together for RD-3 and RD-10, using first shell paths generated from a FEFF6 model of a disordered $Pt_{10}Ni_{90}$ fcc solid solution. The $Pt_{10}Ni_{90}$ disordered fcc model was generated by creating a Ni fcc lattice and randomly substituting Pt atoms at 10% of the lattice positions. The Pt atoms were distributed evenly throughout the various coordination shells and the lattice constant was the same as determined from XRD. No multiple shell fitting was performed, so all paths mentioned in the following discussion are first shell, single scattering paths. The Pt-Pt path was omitted due to the dilution of Pt in the $Pt_{10}Ni_{90}$ phase which lowered the frequency of Pt-Pt bonding. If the Pt-Pt path was included, the fit could not converge on physically reasonable values for the variables. However, it is obvious from the ~2% misfit to both RD-3 and RD-10 EXAFS data (Table 4.2) and the slight asymmetry of the first shell peak towards larger *R* in Fig. 4.10b,d that the model could be improved by using a linear combination of the $Pt_{10}Ni_{90}$ phase and a Pt-rich phase. This is not possible because the number of independent data points limits the number of variables which can be used to model the EXAFS data. The following restraints were also applied for the co-fit of RD-3 and RD-10[241]:

$$R_{NiPt} = R_{PtNi} \qquad \sigma^2_{NiPt} = \sigma^2_{PtNi} \qquad N_{PtNi} = (x_{Ni}/x_{Pt}) \times N_{NiPt}$$

RD-30 was co-fit using paths generated from a $Pt_{25}Ni_{75}$ FEFF file created in a similar manner to the $Pt_{10}Ni_{90}$ model. RD-30 was fit with similar constraints as listed above for RD-3 and RD-10. However, the Pt-Pt scattering path was able to be included in a successful fit to RD-30, unlike in the fits to RD-3 and RD-10, due to the increased frequency of Pt-Pt bonding in RD-30. The method of Hwang et al was then used to calculate extent of alloying parameters, J_{Ni} and J_{Pt}.[244] See Table 4.2 for the results of the co-fits to the Ni *K*-edges and Pt L_3-edges of RD-3, RD-10, and RD-30 and the extent of alloying parameters.

A4. Methods of Chapter 5

Portions of the content of this chapter are reprinted or adapted with permission from N. Becknell[†], Y. Son[†], D. Kim, Y. Yu, Z. Niu, T. Lei, B. T. Sneed, K. L. More, N. M. Markovic, V. R. Stamenkovic, P. Yang, "Tunable Architecture of Rhombic Dodecahedral Pt-Ni Nanoframe Electrocatalysts", Manuscript in preparation.

A4.1 Chemicals

Nickel (II) nitrate hexahydrate ($Ni(NO_3)_2 \cdot 6H_2O$, ≥98.5%), chloroplatinic acid hexahydrate ($H_2PtCl_6 \cdot 6H_2O$, ≥37.5% Pt basis), oleylamine (technical grade, 70%), and hexane (≥98.5%) were purchased from Sigma-Aldrich. Toluene (≥99.9%) was purchased from Fisher Scientific and acetic acid (≥99.7%) was purchased from EMD.

A4.2 Synthesis of Pt-Ni Rhombic Dodecahedra

For H-SD, 20 mg $H_2PtCl_6 \cdot 6H_2O$ and 21.5 mg $Ni(NO_3)_2 \cdot 6H_2O$ were dissolved in 0.8 mL oleylamine. The solution was injected into 9.2 mL oleylamine which had been kept at 160 °C under Ar for one hour. The reaction was then kept under vacuum for 2.5 minutes. Then, the reaction was heated to 265 °C with a ramping rate of 15 °C/min under Ar atmosphere. The color of the reaction solution changed to black after reaching 265 °C. The reaction was stopped 5 min after the color turned to black. The reaction flask was carefully transferred into a water bath in order to quench the growth process. The produced H-SD was washed twice with ethanol and hexane. For E-SD, the procedures were kept the same except that 20 mg $H_2PtCl_6 \bullet 6H_2O$ and 11.5 mg $Ni(NO_3)_2 \cdot 6H_2O$ were dissolved in 0.6 mL oleylamine and injected into 9.4 mL oleylamine.

A4.3 Chemical corrosion to Nanoframes

For H-NF, H-SD was dispersed in 4 mL toluene and mixed with 4 mL acetic acid and 0.2 mL oleylamine, followed by heating at 90 °C in an oil bath for 2 hours with reflux system. The collected sample was washed twice with ethanol and hexane. E-NF could be evolved from E-SD with the same procedure.

A4.4 Characterization

The prepared samples were analyzed by SEM (Zeiss Gemini Ultra-55 analytical field emission SEM), TEM (Hitachi H-7650), HRTEM (FEI Tecnai F20) and STEM-HAADF and EDS mapping (FEI TitanX 60-300). XRD was performed using a Bruker AXS D8 Advance diffractometer with Cu Kα source. ICP-OES was utilized for total composition analysis with PerkinElmer Optima 7000 DV. XPS was carried out with PHI 5600 X-ray photoelectron spectrometer and analyzed using CasaXPS.

A4.5 EXAFS Data Collection and Analysis

EXAFS data were collected at the ALS Beamline 10.3.2. The data at the Ni *K*-edge and Pt L_3-edge were calibrated to a Ni foil and Pt foil, respectively. All spectra at a given edge were aligned according to a glitch in I_0 near each absorption edge. EXAFS data reduction and EXAFS fitting was performed using the IFEFFIT based programs Athena and Artemis.[254] For additional details on the data collection and reduction, please see Appendix A2.5.

The Ni *K*-edge and Pt L_3-edge were fit together for H-NF and E-NF using first shell paths generated from a FEFF model of a disordered face-centered cubic Pt-Ni alloy with seven Pt and five Ni atoms randomly placed around the central absorbing atom. Outer shell sites were also randomly assigned to hold either a Pt or Ni atom, maintaining the composition to be approximately that identified by ICP for H-NF and E-NF. The following restraints were also applied in co-fitting the two edges:

$$R_{NiPt} = R_{PtNi}$$
$$\sigma^2_{NiPt} = \sigma^2_{PtNi}$$

The extent of alloying parameters, J_{Ni} and J_{Pt} were calculated using the method of Hwang et al.[244] See Table 5.2 for the results to the fits.

A4.6 Electrochemical Characterization

After chemical corrosion, H-NF or E-NF were dispersed in chloroform and added to carbon (Cabot, Vulcan XC-72) in a ratio which produced a loading of 15-18 wt% Pt. The mixture was sonicated in chloroform for 30 to 45 minutes to complete the loading process. The catalyst was collected by centrifugation (10,000 rpm), washed once with hexanes, and recollected by centrifugation. The resulting catalyst powder was heated at 200 °C in air for 14 hours in order to remove organic surfactants. The catalyst was then dispersed in water with a concentration of 0.5 $mg_{catalyst}$/mL. The actual concentration of Pt in the ink was determined by ICP-OES. The catalyst ink was dropcast onto a 5 mm glassy carbon disk (Pine Instruments) in the appropriate volume to achieve 4.6 $\mu g_{Pt}/cm^2$ loading density and allowed to air dry. The commercial Pt/C catalyst (Alfa, ~20wt% Pt) had a loading density of 7.8 ug_{Pt}/cm^2. The electrochemical measurements were conducted in a three-compartment glass electrochemical cell with a Pine RDE setup and a Biologic VSP potentiostat. A saturated Ag/AgCl electrode and a Pt wire were used as reference and counter electrodes, respectively, and 0.1 M $HClO_4$ prepared from 67% $HClO_4$ (Sigma-Aldrich) was used as the electrolyte. All potentials are presented versus RHE. H_{upd} measurements were performed by saturating the electrolyte with argon gas before collecting the CV at a sweep rate of 50 mV/s. Electrooxidation of CO_{ad}, or CO-stripping measurements, were performed by purging CO through the electrolyte while holding the potential at 0.05 V. Argon was then purged to remove CO from the electrolyte and the CV was collected at a sweep rate of 50 mV/s. The ORR measurements were collected under O_2 purging conditions and at 20 mV/s with an RDE rotation rate of 1600 rpm. The current densities for ORR were corrected for ohmic iR drop.

A5. Full Publication List

* Indicates publication central to dissertation. † Indicates equal contribution.

1. **Tunable Architecture of Rhombic Dodecahedral Pt-Ni Nanoframe Electrocatalysts.** N. Becknell†, Y. Son†, D. Kim, Y. Yu, Z. Niu, T. Lei, D. Li, B. T. Sneed, K. L. More, N. M. Markovic, V. R. Stamenkovic, P. Yang. **2017**, in preparation. *

2. **Sulfur-Promoted Tin Sites Enable Efficient Electrochemical Reduction of CO_2 to Formate.** X. Zheng, P. De Luna, F. Pelayo Garcia de Arquer, B. Zhang, N. Becknell, M. Ross, Y. Li, M. Norouzi Banis, Y. Li, M. Liu, O. Voznyy, C. Thang Dinh, T. Zhuang, Y. Cui, X. Du, P. Yang, E. H. Sargent. **2017**, submitted.

3. **Electrochemical Activation of CO_2 through Atomic Ordering Transformations of AuCu Nanoparticles.** D. Kim, C. Xie, N. Becknell, Y. Yu, M. Karamad, K. Chan, E. J. Crumlin, J. K. Norskov, P. Yang. **2017**, submitted.

4. **Ultrathin Epitaxial Cu@Au Core-Shell Nanowires for Stable Transparent Conductors.** Z. Niu, F. Cui, Y. Yu, N. Becknell, Y. Sun, G. Khanarian, D. Kim, L. Dou, A. Dehestani, K. Schierle-Arndt, P. Yang. **2017**, submitted.

5. **Room Temperature Dynamics of Vanishing Copper Nanoparticles Supported on Silica.** D. Kim, N. Becknell, Y. Yu, P. Yang. *Nano Letters* **2017**, *17*, 2732. DOI: 10.1021/acs.nanolett.7b00942

6. **Revealing the Size-Dependent d–d Excitations of Cobalt Nanoparticles Using Soft X-ray Spectroscopy.** Z. Cui, C. Xie, X. Feng, N. Becknell, P. Yang, Y. Lu, X. Zhai, X. Liu, W. Yang, Y.-D. Chuang, J. Guo. *Journal of Physical Chemistry Letters* **2017**, *8*, 319. DOI: 10.1021/acs.jpclett.6b02600

7. **Anisotropic Phase Segregation and Migration of Pt in Nanocrystals en route to Nanoframe Catalysts.** Z. Niu†, N. Becknell†, Y. Yu, D. Kim, C. Chen, N. Kornienko, G. A. Somorjai, P. Yang. *Nature Materials* **2016**, *15*, 1188. DOI: 10.1038/nmat4724 *

8. **Nanoporous Transparent MOF Glasses with Accessible Internal Surface.** Y. Zhao, S.-Y. Lee, N. Becknell, O. M. Yaghi, C. A. Angell. *Journal of the American Chemical Society* **2016**, *138*, 10818. DOI: 10.1021/jacs.6b07078

9. **TiO_2/$BiVO_4$ Nanowire Heterostructure Photoanodes Based on Type II Band Alignment.** J. Resasco, H. Zhang, N. Kornienko, N. Becknell, H. Lee, J. Guo, A. Briseno, P. Yang. *ACS Central Science* **2016**, *2*, 80. DOI: 10.1021/acscentsci.5b00402

10. **Synthesis of $PtCo_3$ Polyhedral Nanoparticles and Evolution to Pt_3Co Nanoframes.** N. Becknell, C. Zheng, C. Chen, Y. Yu, P. Yang. *Surface Science* **2016**, *648*, 328. DOI: 10.1016/j.susc.2015.09.024 *

11. **Atomic Structure of Pt_3Ni Nanoframe Electrocatalysts by *in Situ* X-ray Absorption Spectroscopy**. N. Becknell, Y. Kang, C. Chen, J. Resasco, N. Kornienko, J. Guo, N. M. Markovic, G. A. Somorjai, V. R. Stamenkovic, P. Yang. *Journal of the American Chemical Society* **2015**, *137*, 15817. DOI: 10.1021/jacs.5b09639 *

12. **Operando Spectroscopic Analysis of an Amorphous Cobalt Sulfide Hydrogen Evolution Electrocatalyst.** N. Kornienko, J. Resasco, N. Becknell, C.-M. Jiang, Y.-S. Liu, K. Nie, X. Sun, J. Guo, S. R. Leone, P. Yang. *Journal of the American Chemical Society* **2015**, *137*, 7448. DOI: 10.1021/jacs.5b03545